

EFFICIENT MULTISCALE IMAGE FUSION AND FEATURE REDUCTION FOR
ELEVATION DATA IN COASTAL URBAN AREAS

By

SWEUNG WON CHEUNG

A DISSERTATION PRESENTED TO THE GRADUATE SCHOOL
OF THE UNIVERSITY OF FLORIDA IN PARTIAL FULFILLMENT
OF THE REQUIREMENTS FOR THE DEGREE OF
DOCTOR OF PHILOSOPHY

UNIVERSITY OF FLORIDA

2009

© 2009 Sweung Won Cheung

To my family and friends

ACKNOWLEDGMENTS

First of all I would like to thank my parents who have kept encouraging and inspiring me to pursue my dreams in many ways with unconditional love. I also have to thank my beautiful wife, Sookjung Yun, who willingly dedicated her dream and life to me for my dream. And she brought two precious lives, our son and daughter (Brian and Mitchell), and has cared for them many long nights while I was working. For all of this I will always be grateful and in awe of her. And my father-in-law who unexpectedly passed away, always prayed for me. He continues to live on and be with me in spirit

I wish to thank my advisor, Prof. Kenneth C. Slatton. Without his patience, insightful guidance and encouragement this dissertation would never have been realized. His ambition and hard work gave me a good model to follow.

I would also like to thank the members of my PhD. committee, (Prof. Fred J. Taylor, Prof. John G. Harris, and Prof. Ramesh L. Shrestha). I am grateful for their willingness to serve on my committee

I especially thank Dr. Andrew Kennedy and Dr. Robert G. Dean. They willingly shared their time with me and helped me better understand the hydrologic aspects of my application.

I also thank my colleagues at Adaptive Signal Processing Laboratory (ASPL) in the Electrical and Computer Engineering Department and at Geosensing Engineering and Mapping (GEM) Center in Civil and Coastal Engineering Department. The discussions with my colleagues always gave me pleasant and new realizations I will never forget.

TABLE OF CONTENTS

| | <u>page</u> |
|---|-------------|
| ACKNOWLEDGMENTS | 4 |
| LIST OF TABLES | 7 |
| LIST OF FIGURES | 8 |
| LIST OF ABBREVIATIONS..... | 10 |
| ABSTRACT..... | 12 |
| CHAPTER | |
| 1 INTRODUCTION | 14 |
| 2 REMOTE SENSING DATA AND DATA FUSION..... | 18 |
| 2.1 Study Site..... | 18 |
| 2.2 Remote Sensing Data Sets..... | 19 |
| 2.2.1 NOAA NGDC | 19 |
| 2.2.3 Topographic LiDAR..... | 20 |
| 2.2.4 Bathymetric LiDAR | 21 |
| 2.2.5 SRTM | 22 |
| 2.3 Data Fusion..... | 25 |
| 2.3.1 Kalman Filter and Smoother | 26 |
| 2.3.2 Multiscale Kalman Filter and Smoother..... | 29 |
| 3 MULTISCALE ELEVATION IMAGE FUSION OVER COASTAL AREAS | 34 |
| 3.1 Introduction..... | 34 |
| 3.2 Reduced-Complexity MKS | 36 |
| 3.2.1 Simplified Equation for Calculating Process Noise Variance..... | 36 |
| 3.2.2 Pruning Quadtree Structure | 38 |
| 3.2.3 Results | 41 |
| 3.3 Landscape-dependent Evaluation of SRTM Accuracy..... | 44 |
| 3.3.1 Approximating the Hydrologic Surface by Region Properties..... | 45 |
| 3.3.2 Assessing the Measurement Error Variance of SRTM | 48 |
| 3.3.3 Big Measurement Error of SRM over the Coastline | 52 |
| 3.3.4 Results | 54 |
| 4 MULTISCALE FEATURE REDUCTION FOR HYDROLOGIC MODELING OF URBAN AREAS | 58 |
| 4.1 Introduction..... | 58 |
| 4.2 Decomposition..... | 62 |

| | | |
|---------|--|-----|
| 4.3 | Reduction and Scale Selection..... | 66 |
| 4.3.1 | Ground..... | 67 |
| 4.3.2 | Building..... | 69 |
| 4.4 | Evaluation..... | 74 |
| 4.4.1 | Mean Square Error and Correlation Coefficient | 75 |
| 4.4.2 | Flow Accumulation Number | 76 |
| 4.4.3 | Water Discharge Rate..... | 81 |
| 4.4.3.1 | Simple 2D Hydraulic Model | 81 |
| 4.4.3.2 | Sub-grid Parameterization..... | 88 |
| 4.4.3.3 | Evaluation..... | 91 |
| 5 | CONCLUSIONS AND FUTURE WORK..... | 98 |
| | APPENDIX DETAILED DERIVATION OF PROCESS NOISE VARIANCE | 104 |
| | LIST OF REFERENCES..... | 108 |
| | BIOGRAPHICAL SKETCH | 114 |

LIST OF TABLES

| <u>Table</u> | | <u>page</u> |
|--------------|--|-------------|
| 2-1 | Original data spacing and published RMS error for data sets | 19 |
| 3-1 | Comparison of memory storage using RC-MKS and standard MKS..... | 41 |
| 3-2 | Real values of error variance with respect to the color mapped on elevation surface..... | 43 |
| 3-3 | Estimated measurement error standard deviations for SRTM..... | 51 |
| 4-1 | Memory requirements for buildings as a function of scale..... | 72 |
| 5-1 | The similarity between Gain Q_x and MSE, CC, LOSD | 103 |

LIST OF FIGURES

| <u>Figure</u> | <u>page</u> |
|---------------|---|
| 2-1 | A 1° latitude × 1° longitude tile of the NOAA elevation data over the Florida coast18 |
| 2-2 | The solution to recursive minimum mean square estimation27 |
| 2-3 | Quadtree data structure with two measurements30 |
| 2-4 | Procedure for multiscale Kalman filter (upward sweeping).....32 |
| 2-5 | Procedure for multiscale Kalman smoother (downward sweeping).....33 |
| 3-1 | Data processing structures and procedure RC-MKS39 |
| 3-2 | Fused and estimated DEM by RC- MKS.....42 |
| 3-3 | Example of generating a DEM from LBS+ LiDAR data over urban test site.46 |
| 3-4 | Three studied sites extracted from Dade County, Florida48 |
| 3-5 | DEMs obtained from LIDAR and SRTM DTED-2.....49 |
| 3-6 | Kalman filter residuals (innovations) for the three terrain types.50 |
| 3-7 | Error variance mapping depending on the density of urban development.52 |
| 3-8 | A 1.5km × 1.5km coastal site shown at the SRTM scale53 |
| 3-9 | Component data sets to be fused together over a 20km × 20 km area.....54 |
| 3-10 | MKS fusion results for the 20km × 20km area.....55 |
| 3-11 | Two-meter simulated flood images over the 1.5km × 1.5km coastal site56 |
| 4-1 | Ground and non ground DEM of LiDAR.....63 |
| 4-2 | Procedure for making hydrologic surface.....64 |
| 4-3 | Spectral characteristic of ground and buildings.....65 |
| 4-4 | Optimal scale selection for ground data.....68 |
| 4-5 | Encoding building and scale-division procedure.....71 |
| 4-6 | Optimal scale selection for buildings.....73 |
| 4-7 | Two kinds of DEMs in different scales.74 |

| | | |
|------|--|-----|
| 4-8 | Evaluation of the hydrologic DEMs. | 76 |
| 4-9 | Procedure of calculating FAN. | 77 |
| 4-10 | Input and resultant images for the FAN metric. | 78 |
| 4-11 | FAN and DHRA at different scales. | 79 |
| 4-12 | Comparison to high risk area detection (DHRA) by FAN | 80 |
| 4-13 | Spatial domain discretization scheme..... | 83 |
| 4-14 | Pictorial illustration of the criterion..... | 84 |
| 4-15 | Convergence of our simple model with changing bottom friction value..... | 86 |
| 4-16 | Testing of the ratio of the numerical solution to an analytical solution..... | 87 |
| 4-17 | Example of the physical behavior of water by building. | 88 |
| 4-18 | Procedure for calculating WDR..... | 90 |
| 4-19 | Simple simulated DEM and its estimated WDR..... | 91 |
| 4-20 | Estimated WDR of hydrologic DEM made by downsampling | 92 |
| 4-21 | Estimated WDR of hydrologic DEM and sub-grid parameterization..... | 93 |
| 4-22 | Comparison of total discharge rate and running-time..... | 93 |
| 4-23 | Comparison of total discharge rate over real DEM data..... | 94 |
| 4-24 | Estimate of total discharge rate on different sites in Dade County, Miami, FL | 95 |
| 4-25 | Estimate of total discharge rate on simulated DEMs having different building distribution. | 96 |
| 5-1 | LOSD and its error for the quantization of buildings. | 101 |
| 5-2 | Comparison measurements (MSE, CC, LOSD) with Water discharge rate, (Q_x)..... | 102 |

LIST OF ABBREVIATIONS

| | |
|--------|---|
| ACF | Auto-Correlation Function |
| ALSM | Airborne Laser Swath Mapping |
| BB | Building-Block |
| BH | Building-Hole |
| CC | Correlation Coefficient |
| DEM | Digital Elevation Models |
| DTED-2 | Digital Terrain Elevation Data – Level 2 |
| EGM96 | Earth Gravity Model 1996 |
| fBm | fractional Brownian motion |
| FAN | Flow Accumulation Number |
| FDE | Finite Difference Equations |
| FEMA | Federal Emergency Management Agency |
| FIU | Florida International University |
| HMM | Hidden Markov Model |
| IHRC | International Hurricane Research Center |
| LBS | LiDAR Bottom Surface |
| LiDAR | Light Detection And Ranging |
| LMMSE | Linear Minimum Mean Square Error |
| LTS | LiDAR Top Surface |
| LULC | Land Use Land Cover |
| MHHW | Mean Higher High Water |
| MKS | Multiscale Kalman filter and Smoother |
| MSE | Mean Square Error |
| NASA | National Aeronautics and Space Administration |

| | |
|--------|--|
| NED | National Elevation Dataset |
| NGA | National Geospatial-Intelligence Agency |
| NGDC | National Geophysical Data Center |
| NOAA | National Oceanic and Atmospheric Association |
| RC-MKS | Reduced Complexity MKS |
| RMS | Root Mean Square |
| RTS | Rauch-Tung-Striebel |
| SAR | Synthetic Aperture Radar |
| SFWMD | South Florida Water Management District |
| SRTM | Shuttle Radar Topography Mission |
| SWE | Shallow Water Equation |
| UF | University of Florida |
| USGS | United States Geological Survey |
| UTM | Universal Transverse Mercator |
| WDR | Water Discharge Rate |

Abstract of Dissertation Presented to the Graduate School
of the University of Florida in Partial Fulfillment of the
Requirements for the Degree of Doctor of Philosophy

EFFICIENT MULTISCALE IMAGE FUSION AND FEATURE REDUCTION FOR
ELEVATION DATA IN COASTAL URBAN AREAS

By

Sweung Won Cheung

May 2009

Chair: K. Clint Slatton

Major: Electrical and Computer Engineering

Technological advances in the remote sensing of elevations have made it possible to improve topographic resolutions to the 1-10 meter scale and bathymetric (underwater elevations) to the 5-90 m scale. To a large extent, however, data collected at different resolutions and from different types of sensors remain largely separate and their joint information content under-exploited. For many applications, such as flood modeling, there is a vital need to combine information from these seemingly disparate data sets and extract characteristics about the surface that can aid Earth scientists and emergency planners. The research discussed in this dissertation consists of two parts that address this need.

In the first component of the work, a simplified formulation for calculating the variance of the process noise in a multiscale Kalman smoother is derived and implemented via a pruning method on the quadtree data structure. This method exploits the distribution of measurements in the finest scale to efficiently fuse multi-resolution data with different areas of spatial coverage to produce seamless single surface digital elevation models (DEMs). To further improve the accuracy of the Kalman-based fusion, a landscape-dependent measurement error is calculated for the Shuttle Radar Topography Mission (SRTM) data set, providing information on a scale intermediate to the meter-scale DEMs from airborne laser altimetry (LiDAR) and 90-m coastal

DEMs created by the National Oceanic and Atmospheric Association (NOAA). Analysis of the Multiscale Kalman filter and Smoother (MKS) residuals was employed because only a single (spatially uniform) value for the SRTM measurement error is specified by the US Geological Survey (USGS). This was done by defining a LiDAR-derived hydrologic ground surface that excludes vegetation and bridges, under which flood waters can pass.

In the second component of this work, an alternative method to traditional downsampling and mesh generation (used to reduce DEM resolutions to scales at which flood and storm surge modelers can run their fluid-dynamics algorithms) is described. By recognizing that the two main DEM components in urban areas that control flood water flow (i.e. ground and buildings) exhibit different spatial frequencies, vegetation points can be filtered out, resulting in a DEM that can be further decomposed into ground and building classes. The resolution of each class can then be reduced independently, using downsampling for the ground elevations and rectangular parameterization for the building regions (so as to preserve the “channels” for water flowing between buildings even when the overall resolution is dramatically decreased). To examine the performance improvements of the new method compared to the traditional method of downsampling DEMs used by the hydrologic modeling community, two DEM-based hydrologic calculations, flow accumulation number and hydraulic water discharge rate, were calculated. The results obtained from these two calculations confirm that the new method better preserves flood model accuracy with reduced computation time as a function of DEM resolution.

CHAPTER1 INTRODUCTION

As population levels and investment in civil infrastructure in coastal areas continue to increase, the need to accurately predict natural hazard risks such as hurricanes, tsunamis, and sea-level rise becomes increasingly important (Small *et al.*, 2000). Inland flooding and extreme wave action caused by storm surge are influenced by nearshore topography and bathymetry (underwater elevations), which are the surface expressions of underlying geologic and sedimentary processes (Dean *et al.*, 2002). There is also a need to characterize the coastal zone environment for improved understanding of nearshore physical and biological processes. Airborne Laser Swath Mapping (ALSM) is a term for laser-based light detection and ranging (LiDAR) technology used to map terrain elevations at high resolutions. ALSM enables measurement of topography at the scales needed to accurately monitor, predict and mitigate coastal flooding and erosion (Shrestha *et al.*, 2005). Modern topographic LiDAR data are generally acquired at a wavelength of 1064 nm (the near infrared portion of the spectrum), which does not penetrate water. These systems are capable of very fast pulse rates, however, to achieve 1 to 5 m spatial resolution in the resulting elevation images, which are referred to as Digital Elevation Models (DEMs). Bathymetric LiDAR systems typically use the frequency-doubled wavelength of 532 nm (green light), which penetrates water up to 60 meters deep (depending on water clarity). Spatial DEM resolution is generally no better than 10 m because the higher pulse energies require slower pulse rates.

A mathematical framework for estimating surface elevations by fusing major elevation data types is therefore needed so that regional coastal flooding and erosion can be accurately predicted and mitigated. Precise mapping of the nearshore ocean bottom is particularly important for characterizing acoustic propagation and benthic environments (Komar, 1998), (Kuperman,

2004). A robust and scalable framework for combining surface elevation data from above (topography) and below (bathymetry) the waterline is presented. In addition, the framework has the potential to support other applications, such as the modeling of geologic and biologic processes, tactical expeditionary (military) operations, and aid to emergency responders.

The Multiscale Kalman Smoother (MKS) algorithm is a globally optimal estimator for fusing remotely sensed data of different spatial resolutions (Chou *et al.*, 1994), (Fieguth *et al.*, 1995), (Slatton *et al.*, 2005). The MKS algorithm can be readily parallelized because it operates on a Markov tree data structure. However, such an implementation requires a large amount of memory to store the parameters and estimates at each scale in the tree. This becomes particularly inefficient in applications where the observations have very different resolutions and the finest scale data are sparse or locally aggregated. Such cases commonly arise when fusing data to capture both regional structures (generally acquired by lower resolution sensors) and local structures (generally acquired by higher resolution sensors). We develop a reduced-complexity MKS algorithm through the reduction of the number of floating point operations per node by deriving a simplified equation for calculating the process noise variance and also reducing the number of nodes in the quadtree that must be processed. This leads to a dramatic reduction in floating point operations required for estimating a DEM from the fusion of topographic and bathymetric elevations.

Data from the Shuttle Radar Topography Mission (SRTM) is shown to provide important intermediate-scale information between large national elevation data sets and small high-resolution LiDAR data sets. We evaluate the accuracy of SRTM elevations over the Florida coast using filter residuals in an adaptive multiscale fusion algorithm. We obtain fused DEMs at multiple scales and demonstrate improved DEM quality for coastal flood prediction.

Modern ranging sensor technology, in particular airborne LiDAR, enables the formation of DEM images with pixel resolutions of 1m x 1m or smaller. Such data sets should, in principle, improve our ability to accurately monitor, predict and mitigate coastal flooding and erosion (Shrestha *et al.*, 2005). But in general, the flood and storm surge modeling community struggles with incorporating high resolution data into their flood predictions (Bates, 2004). The fundamental equation for fluid dynamics is the well known Navier-Stokes Equation (Acheson, 1990), from which many specialized equations are derived to predict water level, velocity, and momentum. For all but the simplest geometries and momentum conservation assumptions, these equations offer no closed form solution, thus requiring computationally intensive numerical solutions. Solving the equations iteratively for every pixel and every possible direction of water flow on a very large DEM often leads to unacceptable computational times (Alemseged *et al.*, 2005).

We present a method for decomposing the hydrologic surface into two distinct components, ground and building, and then reduce their resolutions independently in the spatial domain for the purpose of reducing the computational time needed by flood models. To give a guideline for the modeler to decide a proper scale, we propose an optimal scale selection by balancing memory usage with the user's accuracy requirements. While still a relatively new topic, some approaches to encoding the impact of buildings in flood or surge routing have been explored (Alemseged *et al.*, 2005), (Neelz *et al.*, 2007). We suggest a new method to encode the impact. It is derived by combining the drag force of buildings with shear stress of the ground, including its dependence on the water depth.

Chapter 2 describes the study site and different remote sensing data sets used (e.g. 90 m resolution NOAA NGDC, 30 m resolution SRTM) to make a seamless combined topographic-bathymetric DEM. Background information is given about the multiscale Kalman filter and how it is applied to fuse multiple images of different resolutions. Chapter 3 then presents an example of the traditional application of MKS, and the difficulties, primarily high computational complexity that arise. Motivation is given for the proposed method, known as the reduced-complexity multiscale Kalman Smoother (RC-MKS). In Section 3.2, we evaluate the accuracy of the SRTM data over the Miami Beach area through statistical characterization of the Kalman innovation terms, creating a terrain-dependent measurement uncertainty. Accurate delineation of the coastline is then achieved by using the fine-scale LiDAR data to boost the uncertainty values at the coarse SRTM scale. In Chapter 4, we compare the performance of RC-MKS in an urban environment to the traditional method of downsampling using a number of error metrics (e.g. root mean square error and correlation coefficient). A novel method for estimating the impact of buildings for hydraulic models while maintaining low memory usage is described. Conclusions and topics for future research are discussed in Chapter 5.

CHAPTER 2 REMOTE SENSING DATA AND DATA FUSION

2.1 Study Site

The investigated site is located in Dade County, FL and consists mainly of sandy beaches, barrier islands, and underwater shoals. The site encompasses the Miami Beach barrier island and the lip of the continental shelf. Beyond the shelf break, the surface drops down into the Straits of Florida (Figure 2-1). The data also includes a part of the densely populated urban center of the city of Miami. This region of North American coast is prone to hurricanes and tropical storms. It also experiences seasonal beach erosion and rip currents (Komar *et al.*, 1998). We focused on this one site because there are relatively few locations with as wide an array of topographic and bathymetric data sets available as this one. The data types that are the most limited in their coverages around the world are the topographic and bathymetric LiDAR data sets. Such data are, however, being collected more and more, and will thus play increasingly important roles in future flood modeling.

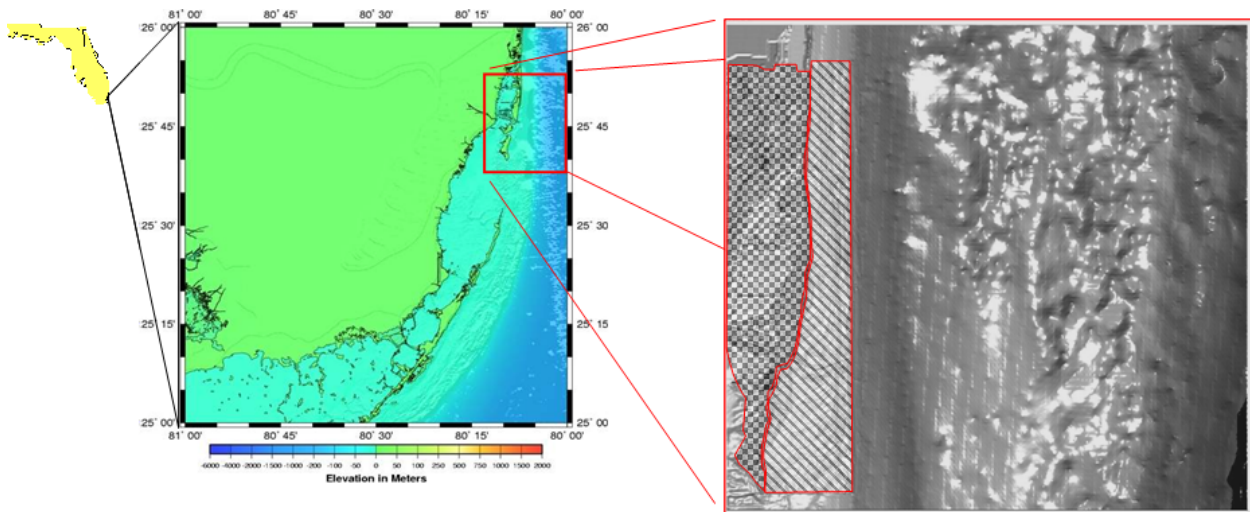


Figure 2-1. A 1° latitude \times 1° longitude tile of the NOAA elevation data over the Florida coast [NGDC, 2005]. The outlined box indicates the region of interest over Miami Beach, Coverage of the multiscale observations: (shaded relief) $40\text{km} \times 40\text{km}$ NGDC data, (diagonal hatch) bathymetric LiDAR coverage, and (checker hatch) topographic LiDAR coverage

Table 2-1. Original data spacing and published RMS error for data sets (NGDC, 2005; USGS, 2000; Gesch *et al.*, 2001; LADS, 2003; IHRC, 2004).

| Data source | Data type | RMS error |
|-------------|-----------------|--|
| NOAA NGDC | 90 m topography | 7 m |
| NOAA NGDC | 90 m bathymetry | 0.3 m ; $0 m \leq d < 20 m$ 1.0 m ; $20 m \leq d < 100 m$ ($0.01 \times d$) m ; $d \geq 100 m$ (<i>d</i> : depth of bathymetry (meters)) |
| SRTM | 30 m topography | 6 ~ 10 m |
| Tenix LADS | 10 m bathymetry | 0.50 m |
| UF/FIU ALSM | 5 m topography | 0.12 m |

2.2 Remote Sensing Data Sets

2.2.1 NOAA NGDC

The National Oceanic and Atmospheric Administration (NOAA) created the National Geophysical Data Center (NGDC), the purpose of which is to create and maintain an official elevation data set consisting of integrated topographic and bathymetric elevations along the U.S. coastline (NGDC, 2005). The primary acquisition modality for the bathymetric data is acoustic sonar deployed from boats. The standard grid spacing of the NGDC DEM is 3 arc-seconds (approximately 90m × 90m). The coverage of the sonar soundings used to derive the bathymetric grid data varies with location, but is often dense near populated shores and grows sparser with distance from the shore. For this work, a 40km × 40km area was extracted from the 1° × 1° NGDC tile shown in Figure 2-1. Since the MKS quadtree requires integer scale changes, the NGCD data were up-sampled to 80 m.

The expected measurement uncertainty in the bathymetric elevations is a function of water depth (NGDC, 2005) and is given in Table 2-1. The soundings were acquired over many years, and are therefore not necessarily representative of the current state of the shallow-water

bathymetry, which motivated the acquisition of higher resolution bathymetry in the shallow water via LiDAR (discussed below).

The topographic component of the NGDC DEM is taken from the National Elevation Dataset (NED) developed by USGS (U.S. Geological Survey) from stereo aerial photography acquired over many years (NGDC, 2005). The standard NED DEMs are available from USGS at 1 arc-second postings (approximately 30m × 30m), but for consistency with the bathymetry, NOAA formats the topographic component of the NGDC data set at a 3 arc-second spacing. Thus, the topographic component of the NGDC can be significantly out of date in areas undergoing urbanization or development and is too coarse to capture much of the important topography that can influence floodwater routing. Furthermore, the USGS NED data are derived by interpreting elevation contours from the aerial photography. Thus, buildings and many small landforms, such as stream channels, are completely lost. The primary advantage to the NGDC data set is its uniform coverage of the entire US coastline, consisting of a mosaic of 1° × 1° tiles that are publicly available (NGDC, 2005). Thus, it is ideal for “filling in gaps” between higher resolution images.

2.2.3 Topographic LiDAR

LiDAR-derived elevations over the barrier islands and coastal uplands were acquired by an ALSM system that was jointly owned by the University of Florida (UF) and Florida International University (FIU). The sensor consists of an Optech 1233 laser altimeter that pulses at 33 kHz and operates at a 1064 nm (near-infrared) wavelength, which does not penetrate water (Carter *et al.*, 2001). First and last laser returns are recorded for each outgoing pulse. The data used in this work were acquired as part of a Federal Emergency Management Agency (FEMA) grant in 2002 and 2003. Acquisition and processing details can be found in the project final report in International Hurricane Research Center (IHRC, 2004). This acquisition was conducted by FIU

personnel and processed to FEMA specifications. Thus, only the DEMs were available, not the raw LiDAR point data.

With a maximum scan angle of only +/- 20 degrees from nadir, such ALSM systems can only image a swath width of roughly 400 m when flying at an altitude of 600 m above ground. In order to decrease the number of flight lines necessary for complete coverage of the Miami area, the aircraft was flown at relatively high altitudes (between 900 m and 1200 m above ground level), increasing the effective swath width, footprint spacing, and footprint diameter. The average root mean squared error of the ALSM DEM elevations was still very good at 12cm (IHRC, 2004), but data voids and dropouts were common, particularly over low-reflectance surfaces (e.g. canals) and shadowed areas, due to higher path length losses and increased footprint spacing. For this study, the LiDAR points representing the geo-referenced laser reflections in the IHRC data set were interpolated to form DEMs with 5m pixel spacing.

2.2.4 Bathymetric LiDAR

The 3 arc-second NGDC DEMs do not have sufficient resolution to capture small-scale bathymetric features in the nearshore region, such as breaks in underwater sand bars that can lead to rip currents. In the fall of 2002, a bathymetric LiDAR system operated by the Tenix LADS Corporation contracted with the state of Florida to acquire nearshore bathymetry off the coast of Dade County. The bathymetric elevations were acquired by the LADS MkII system using a 532 nm wavelength laser (a frequency-doubled output from a 1064 nm laser). The laser pulses at 900 Hz while scanning over a 240 m wide swath (Stumpf *et al.*, 2003), resulting in a nominal horizontal spot spacing of 4 m. The laser footprint diameter on the water surface is approximately 2.5 m with 300~400m flight altitude. The Dade County acquisition covered an area of roughly 7km × 30km with a grid spacing of 10 m in the resulting DEM (Figure 2-1). We obtained the LADS data from the Florida Department of Environmental Protection. Only the

DEM was available, not that raw LiDAR point data. Prior to the MKS data fusion, the bathymetric LiDAR data were upsampled to 5m and combined with the 5m topographic LiDAR data since the coverage areas were small and mutually exclusive. While not strictly necessary, this was done early in the analysis so that each level in the quadtree data structure that would eventually be populated with data could be associated with a given sensor type or data product (e.g. LiDAR, space-based SRTM radar, and the NOAA NGDC data). Although the maximum measurable depth for the Tenix LADS Mk II is specified as 70 m, data for the Dade County acquisition were limited to a maximum depth of about 60 m due to limited water clarity.

2.2.5 SRTM

SRTM was a cooperative project between the National Geospatial-Intelligence Agency (NGA), the National Aeronautics and Space Administration (NASA) and the German and Italian space agencies. The entire SRTM data set was acquired during a single Space Shuttle mission in February 2000, yielding a temporally consistent “snapshot” of the Earth’s surface that is more recent than the NGDC data from NOAA. The primary instrument was a dual-antenna C-band (wavelength of 5.6cm) radar carried onboard the Space Shuttle Endeavour. Limited X-band (wavelength of 3cm) data were also acquired. Data were collected over 80% of the Earth’s surface (between 60° N and 56° S latitude) (USGS, 2004). Unlike most other large scale elevation data sets, SRTM elevations were generated from one consistent source (single sensor on a single flight), resulting in smaller and more consistent elevation errors (Gesch *et al.*, 2001).

Only the C-band system on SRTM was operated in a Scan Synthetic Aperture Radar (SAR) mode, which allowed it to obtain contiguous coverage of the terrain. Thus, only the C-band data were used to generate the Digital Terrain Elevation Data – Level 2 (DTED-2) data products for NGA, where level 2 refers to 1 arc second spacing. Due to the Scan-SAR acquisition method and the orbital trajectory, the coverage density of individual SAR images

varies with location. Coverage is dense at high latitudes and relatively low near the equator. The wavelength and variable coverage have implications for phase unwrapping and vegetation penetration. Radar energy at C-band wavelengths typically exhibits limited penetration of vegetation canopies. Thus SRTM DTED-2 elevations represent an intermediate height between the bare-surface and canopy tops. The precise height bias due to land-cover is unknown because it is highly dependent on the vegetation type and density, number of component SRTM images in the particular DTED-2 tile, and their incidence angles.

At present, data at 1 arc-second (~30m) horizontal resolution for the United States and 3 arc-second (~90m) for the rest of the world are distributed by USGS. Since the MKS quadtree requires integer scale changes, the SRTM data were up-sampled to 20 m for this work. The mission specifications for absolute horizontal and vertical accuracies are 20 meters (circular error at 90% confidence) and 16 meters (linear error at 90% confidence), respectively. The vertical accuracy is often significantly better than the 16 meters specification, and is actually closer to 10 meters (Farr, T.G, *et al*, 2007).

NGA provides “finished” topographic data from SRTM after performing quality control checks on the “unfinished” data. “Unfinished” SRTM contains occasional voids or gaps, where the terrain is in the radar beam's shadow or in areas of low radar backscatter, such as calm seas and lakes. The “finished” SRTM DEMs have the elevation of areas corresponding to water bodies set to a constant value (zero for oceans, the mean of the surrounding elevations for inland lakes, and monotonically decreasing values along their length for large rivers). Small voids are filled in via interpolation. The finished NGA product is a uniform grid of elevation values indexed to specific points on the ground in a standardized DTED-2 format. One important application that utilizes SRTM digital elevation data is delineating hydrologic surface features,

such as watersheds and large river networks. Since the SRTM dataset covers most of the Earth's land surface, it offers opportunities to extend hydrologic modeling research to nearly the entire world where accurate modeling has not been previously feasible due to the low resolution of existing data sets (Curkendall *et al.*, 2003).

The topographic LiDAR data are provided in orthometric heights referenced to the NAD83 datum using the geoid model Geoid03 (IHRC, 2004), but SRTM data are referenced to the WGS84 ellipsoid using the older geoid model EGM96, (NGA, 2005), as shown in Table 2-1. Before the LiDAR and SRTM data can be compared, they must be brought into a consistent geo-referenced coordinate system. In an effort to provide seamless coverage, NGA had the SRTM data mosaicked into continental-scale data sets, which then underwent continental-scale least-squared ("bundle") adjustments. While the SRTM accuracy on continental scales is excellent, over smaller areas on the order of tens of square kilometers, the geo-referencing of the LiDAR data is more accurate.

Unfortunately, there is a limitation as to how precisely the SRTM heights can be corrected to reflect more recent geoid models, such as Geoid03. The process used by the Jet Propulsion Laboratory to generate SRTM "orthometric" heights was as follows (Slater, 2005).

1. Convert elevations from SRTM sensor coordinates to ellipsoidal heights for the 1 arc-second posting of terrain elevations.
2. Evaluate spherical harmonic expansion of the EGM96 gravity model (geoid) at 0.1° (6 minute) intervals in each 1° × 1° cell to generate geoid undulation values at this interval.
3. Use bilinear interpolation to compute geoid undulations at the SRTM 1 arc-second postings.
4. Subtract the geoid undulation from the ellipsoid height at each 1 arc-second post to generate a floating point orthometric height.
5. Round the floating point value to the nearest integer (meter). These integer height values are the values found in the SRTM DTED-2 data file.

As mentioned above, the EGM96 geoid was embedded in the SRTM data at 0.1° intervals for each $1^\circ \times 1^\circ$ tile before the elevations were quantized to 1 meter integer values. This results in a $\pm 0.5\text{m}$ quantization effect that cannot be removed. While SRTM was “bundle adjusted” for each continent using GPS ground truth, over smaller areas there can be differences between SRTM and accurate LiDAR orthometric heights on the order of a few meters due to the older geoid model embedded in the SRTM data product. If an area with complete LiDAR coverage is to be fused with SRTM data, the average quantization error can be subtracted out of the SRTM data prior to fusion. When fusing data over areas with partial or no LiDAR coverage, however, we must convert the SRTM to data orthometric heights using the following steps (NGA, 2005) and accept the residual $\pm 0.5\text{m}$ quantization errors. The two-step process is as follows:

1. Convert the orthometric heights of the SRTM data to ellipsoid heights by subtracting the geoid, which is calculated by the EGM geoid height calculator version 1.0 (NGA, 2005).
2. Convert the ellipsoid heights back into orthometric heights in NAVD88 using Corpscon version 6 (USACE, 2004). The WGS84 ellipsoid is approximately the same as the GRS80 ellipsoid (geocentric) with slight differences documented in the WGS84 Technical Report (NGA, 2005).

2.3 Data Fusion

Data fusion techniques combine data from multiple sensors or related information from associated databases to achieve improved accuracies and more specific inference than could be achieved by the use of a single sensor alone (Hall *et al.*, 1997). Observational data may be fused at the measurement level, feature level, or decision level. Measurement data can be combined directly if the sensors make a measurement of the same physical phenomena using methods like weighted least squares (Sorenson, 1970). In feature level fusion, features extracted from multiple sensors are combined into a single feature vector. The feature vector can then be used in pattern recognition algorithms, such as clustering (Gunatilaka *et al.*, 2001),(Gao *et al.*, 2005) or in a state-variable estimator, such as a Kalman filter (Gan *et al.*, 2001), (Willisky, A.S., 2002). In

decision level fusion, final decisions are made by fusing the preliminary decisions that are made for each sensor.

Depending on the particular state-to-observation mapping used, state-variable methods can perform either measurement level fusion or feature level fusion. One of the more common approaches is the application of a sequential estimation technique, such as the Kalman filter. Chou *et al.*, (1994) and Fieguth *et al.*, (1995) introduced a recursive estimator consisting of a multiscale variant on the well known Kalman smoother, constructed on a Markov tree data structure. We refer to that basic method as the multiscale Kalman smoother (MKS). It is a methodology for the efficient, statistically optimal fusion of measurements of a Gaussian random process. The approach can solve problems in which the measurement data may convey information about random processes at very different scales (Daniel *et al.*, 1997).

The standard Kalman filter and smoother are first briefly presented below, followed by the theoretical framework for the basic MKS algorithm. In Chapter 3, we discuss the extensions on the standard MKS we developed for making the single surface DEMs by fusing the component elevation data sets.

2.3.1 Kalman Filter and Smoother

The Kalman filter is a recursive stochastic estimator that attempts to minimize the mean squared error between the estimates and the random variables being estimated (i.e. the state variables) (Haykin, 2002), (Hwang *et al.*, 1997), (Kay, 1993). It is often used to “smooth” noisy observations, but unlike Fourier methods, it operates in the time/space-domain. Because it incorporates a stochastic model of the underlying state process, it can continue to produce estimates in the event of data gaps. Since the solution is computed recursively using only the previous estimate and the present observation, the standard Kalman filter has relatively low memory requirements.(Haykin, 2002) It can also be formulated in a matrix form because only

second order statistics are used, thus giving it multiple-input/multiple-output capability. If the model input parameters are known to be correct, the Kalman filter is the optimal linear minimum mean-square error (LMMSE) estimator, and it becomes the optimal MMSE estimator when the signal and noise distributions are Gaussian (Kay, 1993). The state model is given as

$$x(t+1) = \Phi(t)x(t) + w(t) \tag{2-1}$$

where $x(t)$ is the process state vector at time t . $\Phi(t)$ is the state transition matrix. $w(t)$ is the process noise (also sometimes called the detail process), which is assumed to be a white Gaussian processes with zero mean and variance $Q(t)$.

The corresponding observation model is given as

$$y(t) = H(t)x(t) + v(t) \tag{2-2}$$

where $y(t)$ is the observation vector at time t . $H(t)$ is the observation-state relation matrix, and $v(t)$ is the measurement noise process, which is assumed to be a white Gaussian process with zero mean and variance $R(t)$.

In the recursion of the Kalman filter (Figure 2-2), the future state variable at time $t+1$ is first predicted (the *a priori* estimate), along with the error covariance, from the present state and covariance at time t using the stochastic information encoded in the state transition operator and process noise variance.

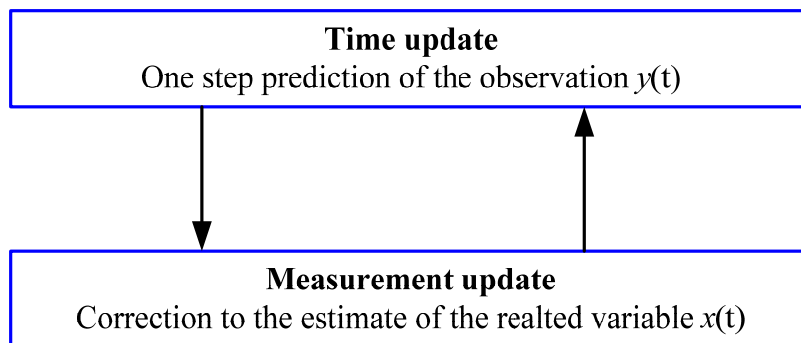


Figure 2-2. The solution to recursive minimum mean square estimation portrayed as a predictor–corrector (Haykin, 2002)

$$\hat{x}(t+1|t) = \Phi(t)\hat{x}(t|t) \quad (2-3)$$

$$P(t+1|t) = \Phi(t)P(t|t)\Phi^T(t) + Q(t) \quad (2-4)$$

The *a posteriori* estimates of the state and covariance at time $t+1$ are then calculated using the present observations at time $t+1$ and the priors,

$$\hat{x}(t+1|t+1) = \hat{x}(t+1|t) + K(t+1)(y(t+1) - H(t+1)\hat{x}(t+1|t)) \quad (2-5)$$

$$P(t+1|t+1) = (I - K(t+1)H^T(t+1))P(t+1|t) \quad (2-6)$$

where $K(t+1)$ is the Kalman gain and is defined as

$$K(t+1) = P(t+1|t)H^T(t+1)(H(t+1)P(t+1|t)H^T(t+1) + R(t+1))^{-1} \quad (2-7)$$

Because the measurement noise variance R appears in the Kalman gain as an inverse factor (or the denominator in the scalar case), the Kalman filter balances uncertainty in the observations with uncertainty in the process. Considering the scalar $H=1$ case for simplicity, one can observe that when R is very small, K is close to unity and the filter “trusts” the observations and tracks them closely. When R is very large, K is close to zero and the filter relies more on the stochastic model because the posterior estimate is dominated by the prior estimate.

The standard Kalman filter makes one pass through the data in one direction, and is thus ideal for processing streaming data. An extension of the Kalman filter, known as the Kalman smoother, can be employed to make both a forward and backward sweep through the data. While it requires processing the data in a “batch mode”, the Kalman smoother has the advantage of achieving optimal estimates conditioned on all of the observations rather than just on the past observations (Hwang *et al.*, 1997). The Kalman filter and Kalman smoother therefore constitute a causal filter and a non-causal filter, respectively (Anderson, 1999).

There are three main types of Kalman smoothing methods: 1) fixed-interval smoothing, 2) fixed-point smoothing, and 3) fixed-lag smoothing (Anderson, 1999). The fixed interval smoothing, also called the Rauch-Tung-Striebel (RTS) algorithm, is the form implemented in our multiscale Kalman smoother. It is of interest to note that the smoothing error variance matrix is not needed for the computation of the estimate in the backward sweep. This is in contrast to the situation in the filter (forward) sweep, where error covariance matrix is needed for the gain and associated estimated computations (Hwang *et al.*, 1997).

The Kalman filter can also be viewed as an analogue to the Hidden Markov Model (HMM). The primary difference is that the underlying state process is assumed continuous and Gaussian in the Kalman filter, whereas the state is often considered discrete and of arbitrary distribution in the HMM. Both approaches can be derived from the Bayesian estimator (Roweis *et al.*, 1999).

2.3.2 Multiscale Kalman Filter and Smoother

Due to the difficulty in establishing suitable 2-D causal models and the high dimensionality of the resulting state vectors, the application of the standard Kalman filter to image processing has been limited (Woods, 1984). But in the 1990s, Chou *et al.* (1994) and Fieguth *et al.* (1995) developed a method that replaced the 2-D recursion in space (pixel rows and columns) with a recursion in scale. This allowed them to develop a causal Kalman filter sweep for images. One of the main motivations for trying to employ causality is to develop computationally efficient algorithms, especially for the large images often encountered in remote sensing.

Figure 2-3 shows a multiscale pyramid, or quadtree data structure, which is used in the multiscale Kalman filter and smoother (Fieguth *et al.*, 1995). The structure is similar to wavelet decompositions applied to multi-resolution analysis, but the Kalman-based approach is able to

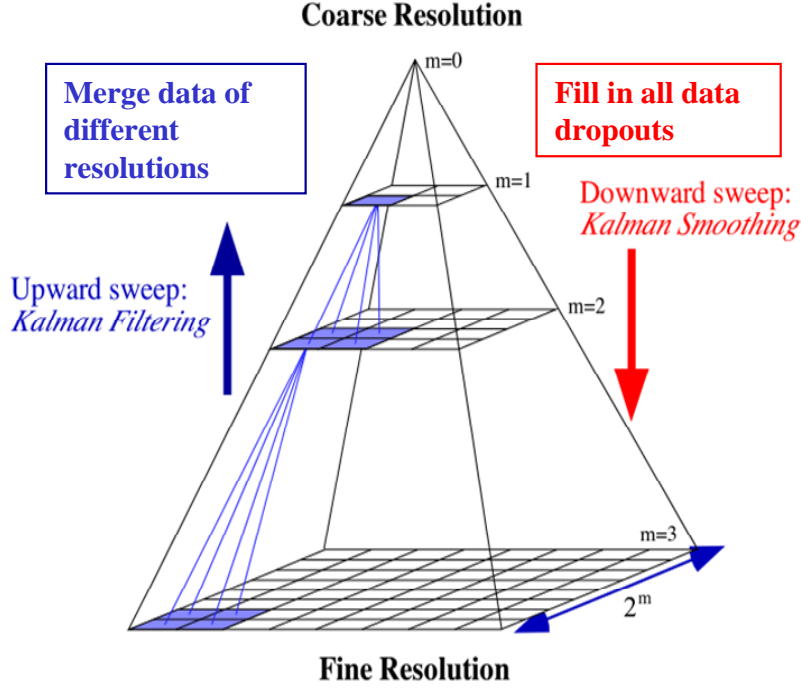


Figure 2-3. Quadtree data structure with two measurements, where m denotes scale. The support of the tree at the finest scale is $2^M \times 2^M$, where $m \in (1, \dots, M)$

accommodate irregularly spaced data and indirect measurements via the observation-state relation, as well as provide error statistics via the covariance matrix (Slatton *et al.*, 2001).

$$x(s) = \Phi(s)x(Bs) + \Gamma(s)w(s) \quad \forall s \in S, s \neq s_o \quad (2-8)$$

$$y(s) = H(s)x(s) + v(s) \quad \forall s \in T \subseteq S \quad (2-9)$$

where $x(s)$ is the state variable at node s . s is the node index on the tree, where $s=1$ denotes the root node. Each node can also be referenced by a three-tuple (i, j, m) , where (i, j) is the pixel row and column of the node at scale (level) m in the tree. $y(s)$ represents the observation (if any) at node s . The stochastic forcing function $w(s)$ is a Gaussian white noise process with unity variance, and the measurement error $v(s)$ is a Gaussian white noise process with scale-dependent variance $R(s)$. S represents the set of all nodes on the quadtree, and T denotes the collection of nodes at which an observation is available. B is a backshift operator in scale, such that Bs is one scale coarser (higher up in the tree) than s . $\Phi(s)$ is the coarse-to-fine state transition operator,

$\Gamma(s)$ is the coarse-to- fine stochastic detail scaling function, $H(s)$ is the measurement-state model, and $R(s)$ represents the measurement variance of the observations. A complete description of the MKS algorithm can be found in Chou *et al.* (1994) and Fieguth *et al.* (1995). The algorithm is non-iterative and has deterministic computational complexity per pixel with $O(S_M)$ operations, where S_M is the number of nodes at the finest scale $m = M$. A residual, known as the innovation, $y(s) - H(s)\hat{x}(s | s+)$ is computed during the Kalman filter recursion, where $\hat{x}(s | s+)$ is the *a priori* state estimate at node s . Total complexity of the scalar MKS is proportional to S_M since the total number of nodes in the tree is $\lfloor \frac{4}{3}S_M \rfloor$ and each node has constant complexity (four children and one parent) (Fieguth *et al.* 1995).

With the generative coarse-to-fine model in place, the MKS algorithm starts with a fine-to-coarse sweep up through the quadtree using a Kalman filter recursion with an added merge step. The fine-to-coarse sweep is followed by a coarse-to-fine downward sweep that corresponds to Kalman smoothing (i.e. the RTS algorithm mentioned earlier). The whole procedure of multiscale Kalman filtering and smoothing is shown in Figures 2-4 and 2-5, respectively. The standard Kalman filter with Gaussian assumption provides optimal estimates in the mean squared sense if perfect *a priori* information regarding the model parameters is known. Since a wide range of natural stochastic processes, such as topography, exhibit power law behavior in their power spectra, they can be effectively modeled as fractional Brownian motion (fBm) processes (Fieguth *et al.*, 1995). We therefore assume that our state process (surface elevation) follows a $1/f^\mu$ model in scale (Fieguth *et al.*, 1995), (Slatton *et al.*, 2001). Using this model, the power spectrum of the state variable $x(s)$ is represented by the multiscale model in (Eq. 2-8) by specifying the coarse-to-fine state transition operator $\Phi(s) = 1$ and process noise standard

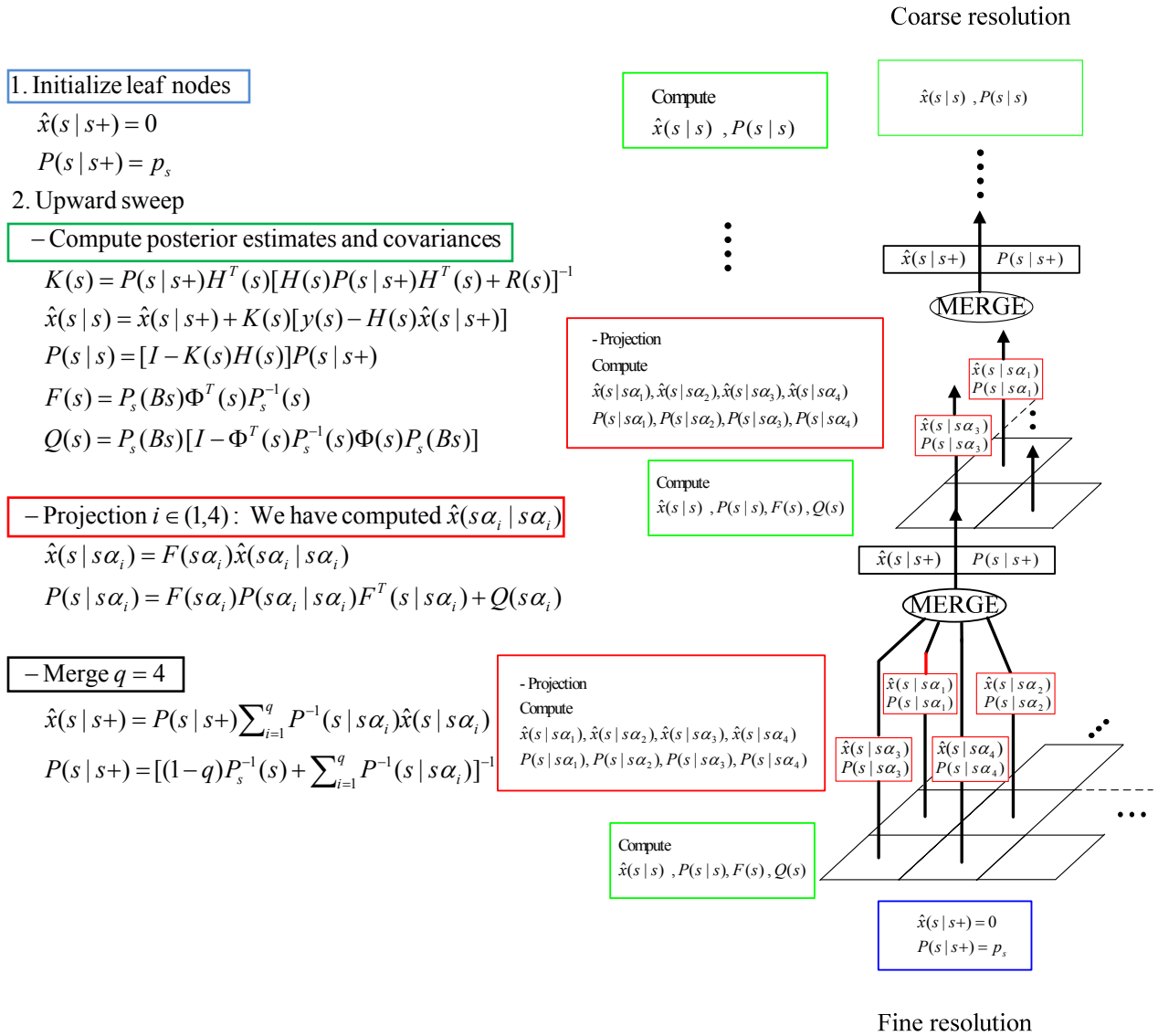


Figure 2-4. Procedure for multiscale Kalman filter (upward sweeping)

deviation $\Gamma(s) = \Gamma_0 2^{\frac{(1-\mu)m}{2}}$. The values of Γ_0 and μ are determined by first order regression of the power spectra of the observations and a realization of the fBm model in log-log space. Since our data sets consist of direct measurements of surface elevation, $H(s_i)$ is simply 1 where $s_i \in T$ and 0 otherwise.

Downward sweep

– Compute smoothed estimates and covariances

$$\hat{x}^s(s) = \hat{x}(s | s) + J(s)[\hat{x}^s(Bs) - \hat{x}(Bs | s)]$$

$$P^s(s) = P(s | s) + J(s)[P^s(Bs) - P(Bs | s)]J^T(s)$$

$$J(s) = P(s | s)F^T(s)P^{-1}(Bs | s)$$

Compute
 $\hat{x}^s(s), P^s(s), J(s)$ using
 $J(s) = 0, \hat{x}(s | s), P(s | s), P(Bs)$
 $\hat{x}(s | s\alpha_1), \hat{x}(s | s\alpha_2), \hat{x}(s | s\alpha_3), \hat{x}(s | s\alpha_4)$
 $P(s | s\alpha_1), P(s | s\alpha_2), P(s | s\alpha_3), P(s | s\alpha_4)$

⋮

Compute
 $\hat{x}^s(s), P^s(s), J(s)$ using
 $J(s), \hat{x}(s | s), P(s | s), P(Bs)$
 $\hat{x}(s | s\alpha_1), \hat{x}(s | s\alpha_2), \hat{x}(s | s\alpha_3), \hat{x}(s | s\alpha_4)$
 $P(s | s\alpha_1), P(s | s\alpha_2), P(s | s\alpha_3), P(s | s\alpha_4)$

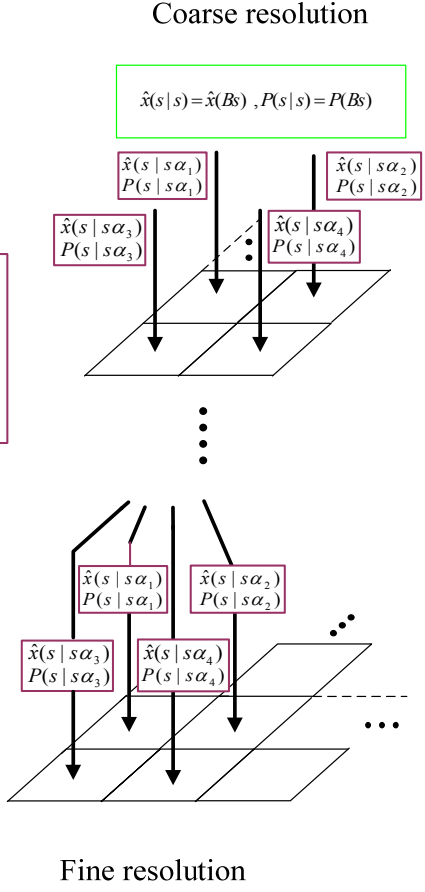


Figure 2-5. Procedure for multiscale Kalman smoother (downward sweeping)

CHAPTER 3 MULTISCALE ELEVATION IMAGE FUSION OVER COASTAL AREAS

3.1 Introduction

Oceanic phenomena, such as hurricanes, tsunamis, and sea-level rise, as well as terrestrial processes, such as fluvial erosion and subsidence, continually modify the world's coastlines. Inland flooding caused by storm surge and extreme wave action is influenced by nearshore topography and bathymetry. As population levels and property development in coastal areas continue to increase, there is a critical need to characterize the coastal zone environment for improved nearshore physical and biological process monitoring. Precise mapping of the ocean bottom is also important for characterizing acoustic propagation for sonar (Komar *et al.*, 1998), (Kuperman *et al.*, 2004).

A mathematical framework for fusing data and estimating coastal zone surface elevations is therefore needed so that coastal flooding and erosion mechanisms can be more accurately predicted and mitigated. A robust and scalable framework for combining surficial elevation data from above (topography) and below (bathymetry) the waterline is presented. The framework could subsequently be used to support geo- and biophysical modeling as well as military functions, such as tactical deployments and post-strike damage assessment in the coastal zone (Hicks *et al.*, 2000). In one study, Starek *et al.*, (2005) generated the DEM of a coastal area (St. Augustine, FL) using airborne LiDAR data. They selected the mean higher high water (MHHW) tidal datum, referenced to a nearby tidal gauge, and used the corresponding elevation contour as an approximation for the shoreline (the MHHW is the average of the high water of each tidal day observed over a 19-year period). The resulting elevation contour was then projected onto the DEM and compared to results derived from conventional methods for determining shoreline position (Starek *et al.*, 2005) (Robertson *et al.*, 2004). When used in conjunction with high

resolution LiDAR DEMs, this approach to deriving the shoreline contour is very accurate spatially. But the LiDAR data usually only cover a thin strip along the beach, and are thus of limited use when establishing the regional elevation surface for flood modeling. Furthermore, no matter how precise a DEM is, it can only reflect the surface conditions (e.g. urban infrastructure) that were present when the data were collected. So ideally, one would want a method to merge different elevation data sets to get continuous coverage of the region, high resolutions wherever possible, and the most recent acquisitions to better reflect recent urban development. This method should also have the ability to encode uncertainty in the data sets based on the data set age, resolution, and/or known sensor characteristics.

Chou *et al.* (1994) and Fieguth *et al.* (1995) introduced a recursive estimator consisting of an MKS constructed on a Markov tree data structure that accommodates multi-sensor observations of differing resolutions. At each node in the tree, the estimator optimally (in a least mean squared error sense) blends a stochastic multiscale model with the available observations according to a Kalman gain that accounts for the error characteristics of each sensor type. The estimator also accommodates sparse and irregularly spaced data and provides an estimate error variance (uncertainty measure) at each node in the tree. Slatton *et al.*, (2001) successfully used MKS to fuse topographic elevations derived from high-resolution interferometric SAR and airborne LiDAR data. However, in many remote sensing applications, it is desirable to extract both regional and local structure. In such cases, the resolutions of the component data sets may differ by an order of magnitude or more, and the highest resolution observations may be sparse relative to the coarse-scale observations. Such data characteristics are common in the case of coastal zone surficial mapping, and lead to numerical inefficiencies in the standard MKS.

3.2 Reduced-Complexity MKS

For a standard implementation of MKS in which two-dimensional surface elevation data are fused, the full set of recursive operations is performed at each node in the quadtree. This approach is highly inefficient if the finest scale (the set of leaf nodes in the quadtree) is populated sparsely with observations. This is often the case with small airborne LiDAR strips along the beaches. So in (Slatton, Cheung *et al.*, 2005), we develop a reduced-complexity version of the MKS algorithm (RC-MKS) to exploit this commonly encountered data configuration. First, we derived an alternative formulation for scale-wise process noise variance to that found in (Fieguth *et al.*, 1995). Then we developed an efficient implementation of the MKS algorithm that indexes the leaf nodes so that only fine-scale nodes containing data are considered in the full recursion.

3.2.1 Simplified Equation for Calculating Process Noise Variance

Because MKS is recursive, significant overall reduction in computational complexity is possible with modest per-node reductions. The nominal MKS algorithm has a per-node computational complexity of $O(L)$ where L is the number of leaf nodes in the quadtree, such that $L=2^{2M}$. where M is the finest scale.

From the downward model (Eq. 2-8) and (Eq. 2-9), which is Markov process and satisfies the forward orthogonal property, i.e. $E(x(0)w^T(s))=0$ for $s \geq 0$ in (Eq. 3-1), a corresponding state equation for the upward model can be written as

$$x(Bs) = \Phi^{-1}(s)x(s) - \Phi^{-1}(s)\Gamma(s)w(s) \quad (3-1)$$

This backward state process is still Markov, but the backward orthogonal condition between $x(s_i)$ and $w(s_j)$ for $s_j \leq s_i$ is not satisfied. Therefore estimate of $x(Bs)$ is not the same to the one step projected estimate of $x(s)$.

We can define $w(s)$ as a sum of MMSE and its error term as follows

$$w(s) = E[w(s) | x(s)] + \tilde{w}(s) \quad (3-2)$$

where $\tilde{w}(s)$ represents the non-orthogonal contributions to $w(s)$ in the upward model. By the MMSE property $\tilde{w}(s_i)$ is orthogonal to $x(s_j)$ for $s_j \geq s_i$. Since we assume that $w(s)$ and $x(s)$ are zero mean and Gaussian, we can write using fundamental formula of MMSE (Kay, 1993)

$$E[w(s) | x(s)] = E[w(s)x^T(s)]E[x(s)x^T(s)]^{-1}x(s) \quad (3-3)$$

Substituting (Eq. 3-1) into (Eq. 3-2) gives

$$E[w(s) | x(s)] = \Gamma^T(s)P_x^{-1}(s)x(s) \quad (3-4)$$

where $P_x(s) = E[x(s)x^T(s)]$. The upward Markov model can then be rewritten (Verghese 1979)

$$x(Bs) = \underbrace{(\Phi^{-1}(s) - \Phi^{-1}(s)\Gamma(s)\Gamma^T(s)P_x^{-1}(s))}_{F(s)}x(s) + \underbrace{\Phi^{-1}(s)\Gamma(s)\tilde{w}(s)}_{\bar{w}(s)} \quad (3-5)$$

We define $Q(s)$ to be

$$\begin{aligned} Q(s) &= E[\bar{w}(s)\bar{w}^T(s)] \\ &= \Phi^{-1}(s)\Gamma(s)E[\tilde{w}(s)\tilde{w}^T(s)]\Gamma^T(s)\Phi^{-T}(s) \\ &= \Phi^{-1}(s)\Gamma(s)[I - \Gamma^T(s)P_x^{-1}(s)\Gamma(s)]\Gamma^T(s)\Phi^{-T}(s) \\ &= \Phi^{-1}(s)\Gamma(s)\Gamma(s)\Phi^{-T}(s) - \Phi^{-1}(s)\Gamma(s)\Gamma^T(s)P_x^{-1}(s)\Gamma(s)\Gamma(s)\Phi^{-T}(s) \end{aligned} \quad (3-6)$$

But from the equation of $P_x(s)$, we can rewrite $Q(s)$ and $F(s)$ as follows.

$$Q(s) = P_x(Bs)\Phi^T(s)\Gamma(s)\Gamma^T(s)\Phi^{-T}(s) \quad (3-7)$$

$$F(s) = P_x(Bs)\Phi^T(s)P_x^{-1}(s) \quad (3-8)$$

Thus, upon substitution of $F(s)$ into $P_x(Bs)$

$$\begin{aligned} Q(s) &= F(s)P_x(s)\Phi^T(s) - F(s)\Phi(s)P_x(Bs) \\ &= P_x(Bs) - F(s)\Phi(s)P_x(Bs) \end{aligned} \quad (3-9)$$

We then write the final expression for $Q(s)$ as

$$Q(s) = (I - F(s)\Phi(s))P_x(Bs) \quad (3-10)$$

which is an alternative to the form presented in (Fieguth *et al.* 1995).

$$Q(s) = P_x(Bs) \left[I - \Phi^T(s)P_x^{-1}(s)\Phi(s)P_x(Bs) \right] \quad (3-11)$$

The alternative calculation for $Q(s)$ in equation (Eq. 3-10) requires two multiplications per node, compared with four multiplications in the standard expression in equation (Eq. 3-11). The reduction by two multiplications per iterative step is for the scalar MKS. If incorporated into a vector MKS, the corresponding reduction would be further increased proportionally to the vector size.

3.2.2 Pruning Quadtree Structure

Further reduction in the computational complexity can be realized if the sparseness of the fine-scale data is exploited. In data fusion applications where the observation scales differ by an order of magnitude or more, it is quite common that the finest-scale data will only be available over a small subset of the quadtree leaf nodes. New information is presented to a Kalman estimator through observations; in the absence of observations, the prior estimate is simply propagated. Thus, we need only consider those subtrees that contain at least one leaf node at which an observation is available (Figure 3-1. C).

Let $m=N$ be the level where dense coarse-scale observations are available, e.g. the NGDC elevations, and $m=M$ be the level where the finest-scale data are available, e.g. LiDAR elevations. We define an indicator (flag) matrix to store the location of populated subtrees. The flag matrix is $2^N \times 2^N$, i.e. the size of the NGDC data matrix. To find valid subtrees, we tile the leaf nodes with a $2^{M-N} \times 2^{M-N}$ window and set the corresponding entry in the flag matrix to 0 if no node in the corresponding tile contains an observation. Otherwise, the entry in flag matrix is

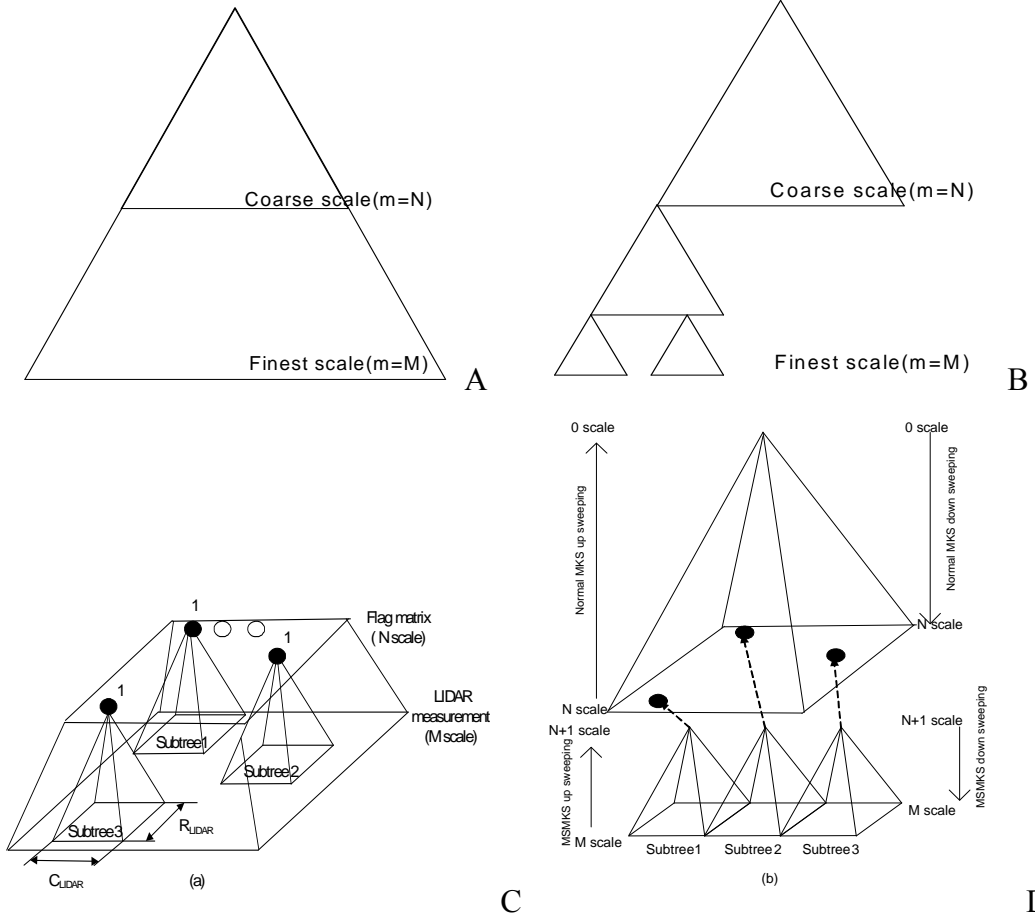


Figure 3-1. Data processing structures and procedure for utilizing the distribution of measurements in the finest scale. A) Full pyramid structure. B) Pruning pyramid structure. C) Set of subtrees for which finest scale data are available. D) Mapping the subtrees to the square matrices using the flag matrix.

set to 1. This can be accomplished at no extra computational cost during the specification of H (measurement-state model operator).

Using the flag matrix, we can obtain a range of row and column indices (R_M and C_M) at the finest scale for each valid subtree as

$$\begin{aligned} R_M &= \left[2^{M-N} \cdot R_N - (2^{M-N} - 1) \right] \sim \left[2^{M-N} \cdot R_N \right] \\ C_M &= \left[2^{M-N} \cdot C_N - (2^{M-N} - 1) \right] \sim \left[2^{M-N} \cdot C_N \right] \end{aligned} \quad (3-12)$$

where R_N and C_N are row and column indices of the flag matrix whose entries are set to 1. Due to the Markov property of MKS, each subtree can be processed independently. In practice,

however, it is convenient to concatenate the subtrees, such that their bases form a single rectangular matrix. That matrix has support $N_{st} \times 2^{M-N} \times 2^{M-N}$, where N_{st} is the number of subtrees. Other MKS parameters, such as H , Γ , and R are similarly permuted to correspond to the concatenated subtree structure. Subtrees that connect leaf nodes to scale N but do not contain observations are not explicitly processed since the priors are propagated directly to scale N .

The reduction in computational complexity afforded by this implicit pruning of the quadtree depends on (i) the size of the subtree blocks, which is determined by the difference in scales M and N and (ii) the aggregation of the fine-scale data, which determines the number of subtrees N_{st} . The percent reduction in floating point operations is determined by the reduction in the number of leaf nodes that must be processed in the recursion, which is given by

$$ME_{\%} = 100 - \left(\frac{N_{st} \cdot 2^{M-N} \cdot 2^{M-N}}{2^M 2^M} \times 100 \right) \quad (3-13)$$

The NOAA NGDC data contains comprehensive coverage (such that there are no data dropouts) at scale N so that we did not apply the memory saving procedure above scale N . With the quadtree now effectively pruned below scale N , the standard MKS algorithm was used to compute estimates for each subtree in parallel (Figure 3-1. D). As we process upwards in the quadtree, the number of data elements processed is reduced by one quarter from the previous scale. These subtrees are used from the finest scale to one scale below the NOAA NGDC scale, (scale $N+1$), for both the upward Kalman filtering sweep and the downward Kalman smoothing sweep. When the filtering process reaches scale $N+1$ the posterior estimates at scale $N+1$ are used as prior information for estimation at scale N in the usual Kalman recursion. To accomplish this, we use the flag matrix as an indicator function to permute the rectangular matrix of Kalman

estimates into a square matrix of prior state information. From scale N , the standard MKS upsweep proceeds with square matrices. Normal down sweeping (Kalman smoothing) is performed from the coarsest (root) scale to NOAA NGDC scale. When the estimator reaches scale $N+1$, it proceeds down through the subtrees according to the flag matrix.

As a final step, we must propagate the estimates at scale N , where the flag matrix value is 0, down to scale M . We initially used the nominal quadtree interpolation, i.e., nearest neighbor (zero order) interpolation, which retains the Markov property for the propagation. However, propagation on a Markov tree over several scales leads to a well known problem known as block artifacts (loss of spatial correlation). To retain spatial correlation, we instead employed an up-sampling of the NGDC data with linear interpolation. The propagated values were then available at scale M in tiles where no LiDAR data were present.

3.2.3 Results

This section presents the application of the proposed RC-MKS method for fusing data sets over the Florida coast. The topographic LiDAR observations and the bathymetric LiDAR were available at a 5m grid spacing (data size = $2^{13} \times 2^{13}$) and a 10m spacing (data size = $2^{12} \times 2^{12}$) respectively. The NGDC observations were resampled from their original 90m spacing to 80m (data size = $2^9 \times 2^9$) so that the data sets would differ in resolution by integer powers of 2.

Table 3-1. Comparison of memory storage using RC-MKS and standard MKS. (Mb :Mega bytes, Gb: Giga bytes)

| m | Memory saving method | | Standard method | |
|-------|----------------------|-----------|-----------------|-----------|
| | Up | Down | Up | Down |
| 10 | 25.22 Mb | 13.19 Mb | 136.31Mb | 71.30 Mb |
| 11 | 100.88 Mb | 52.77 Mb | 545.26 Mb | 285.21 Mb |
| 12 | 403.53 Mb | 211.08 Mb | 2.181 Gb | 1.141 Gb |
| 13 | 1.614 Gb | 844.31 Mb | 8.724 Gb | 4.563 Gb |
| Total | 3.27 Gb | | 17.58 Gb | |

In this example, the bathymetric LiDAR are one level up from the leaf nodes $m = M - 1$. Situations in which observations are present at intermediate scales between M and N do not preclude significant reductions in complexity if the intermediate-scale data have sparse or aggregated support and are close in scale to the finest scale. The locations of intermediate data can be projected down to the leaf nodes and indicated by 1 in the flag matrix along with the finest-scale data. The fused result is shown in Figure 3-2.

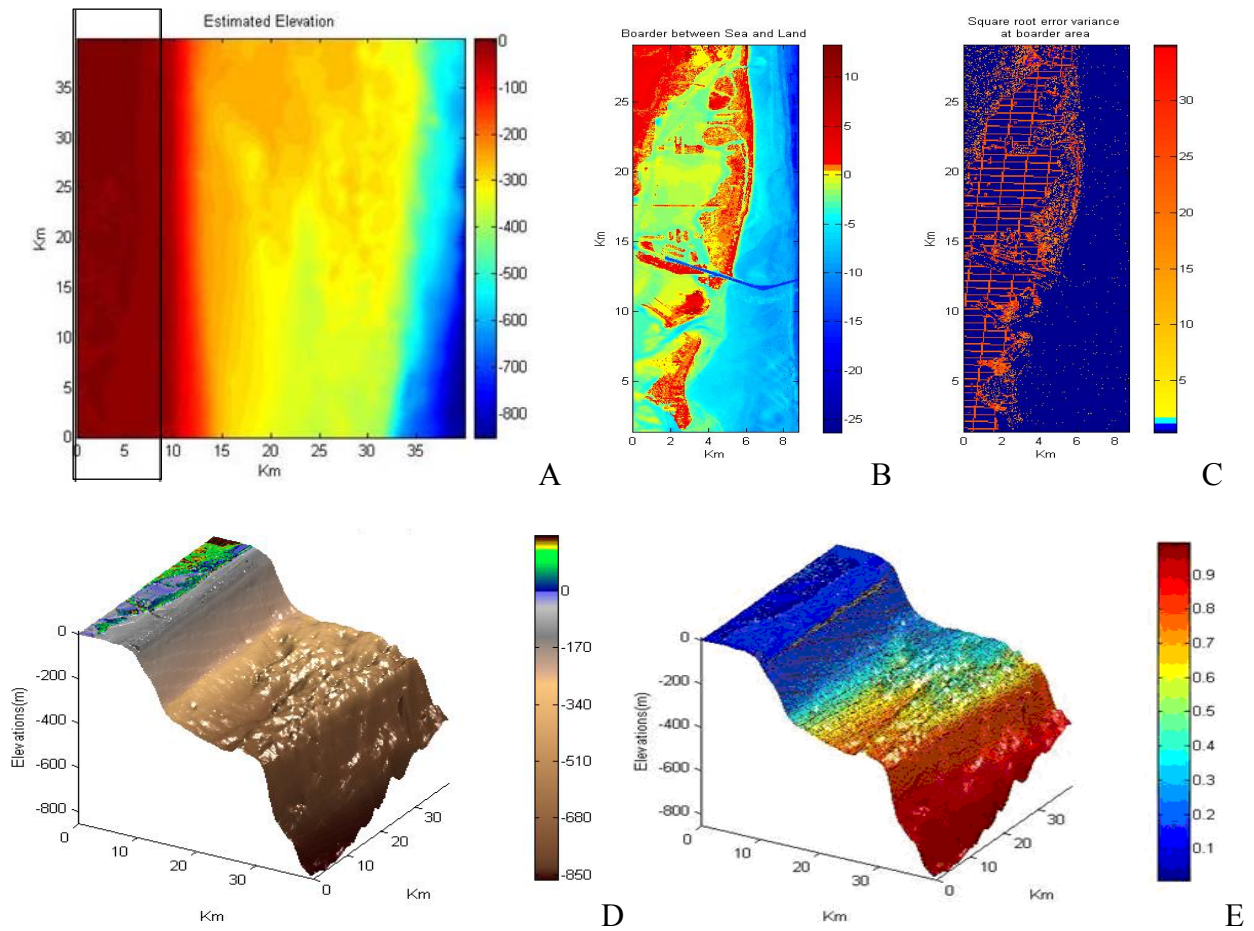


Figure 3-2. Fused and estimated DEM by RC- MKS A) Estimated elevation of 40km x 40km, B) Estimated elevation in outlined area of A, C) RMS error of the bounded area of A) where high resolution data are available. 3 dimensional view of estimated elevations and its error variance D) 3D view of topographic and bathymetric elevations fused and E) 3D view of normalized square root error variance. All elevations are in meters.

Table 3-2. Real values of error variance with respect to the color mapped on elevation surface.

| Colors on surface | Normalized values | Real values (m) |
|-------------------|-------------------|-----------------|
| Dark Red | 1.0 | 24.96 |
| Red | 0.9 | 2.286 |
| Orange | 0.75 | 2.043 |
| Yellow | 0.65 | 1.914 |
| Green | 0.5 | 1.864 |
| Cyan | 0.4 | 1.757 |
| Blue | 0.1 | 0.999 |

Given these data, $M - N = 4$ and N_{st} is 48501, so the support of the sub-trees at the finest scale consists of a 776016×16 array. From Eq. 3-13, we can calculate the expected computational savings. In the standard MKS implementation, the number of leaf nodes to be processed is 2^{2M} , i.e. 8192^2 for $M = 13$. For the investigated data sets in this work, the number of nodes in the reduced leaf node set is $N_{st} \cdot 2^{M-N} \times 2^{M-n}$, i.e. $48501 \cdot 16^2$. The reduction in the number of nodes that must be processed is therefore 81.5% at each scale below $m=N$.

It is also possible to measure the impact of pruning the quadtree in terms of memory required for a non-parallelized implementation of MKS. By reducing the number of subtrees between scale M and N that must be processed, we also significantly reduce the amount of memory required to store values of filter parameters and estimates at those levels in the quadtree. Without loss of generality, we let a 1×1 matrix represent a single byte and then compare the amount of memory used for the MKS algorithm to the amount of memory required for the proposed method below scale N . The columns in Table 3-1 list the required memory for the up and down sweeps for standard MKS and the proposed RC-MKS method. The realized memory savings between the standard MKS that uses the full quadtree and the RC-MKS is 81.4%, which corresponds well to the 81.5% savings predicted by Eq. 3-13. Using both the simpler expression for calculating $Q(s)$ at each node and the pruned quadtree, we obtained a total reduction in

floating point operations of 82.59% in the upsweep and 72.87% in the down sweep. The actual values of each normalized square root error variance in Figure 3-2 are summarized on Table 3-2.

A common problem that arises when fusing data that span a wide range in scales is that the detail of interest is difficult to see in a synoptic view. Important detail exists at both fine (less significant bits) and global (more significant bits) ranges. Simple monotonic transformations of the image histograms are not helpful because they necessarily eliminate valuable detail from one of these extremities. Instead, we partition the color map to reveal both small and large range characteristics that occupy different average values in the range (Figure 3-2).

3.3 Landscape-dependent Evaluation of SRTM Accuracy

NOAA acquires and maintains many datasets for the U.S. coastal zone. NOAA's NGDC has assembled a single topographic and bathymetric database to provide surface elevations of the U.S. coastline at 3 arc-second (roughly 90m) postings. We fuse the NGDC data with SRTM, which provides topographic elevations with 1 arc-second (roughly 30m) postings, along with high resolution topographic LiDAR and bathymetric LiDAR observations near the shoreline with 5m to 10m postings, respectively. In the topographic LiDAR DEMs, it is possible to estimate the actual solid surface on which the water flows (the hydrologic surface) by removing the vegetation but keeping the buildings in. This process is described below. Prior to fusing the data sets, we also estimate the accuracy (encoded in the MKS via the R parameter) of the SRTM elevation data over different landscapes near the coastline. This is accomplished through the statistical characterization of the Kalman filter innovations. Considering the vegetation-penetrating characteristics of the C-band wavelength mentioned previously, we used the LiDAR-derived hydrologic surface for proper evaluation of the SRTM measurement error.

3.3.1 Approximating the Hydrologic Surface by Region Properties

Various field observations and numerical analysis have shown that overland flooding dynamics are strongly influenced by surface morphology (gradient, curvature, and surface roughness), and the distribution of structures on the ground (Harris, 1963). For better prediction and mitigation of coastal flood hazards, we must be able to evaluate where floodwaters will flow. Floodwaters will generally flow around solid structures such as buildings but flow under elevated roads (overpasses) and vegetation canopies. Ideally then, we desire a treatment that classifies overpasses and vegetation separately from buildings when defining our LiDAR-derived hydrologic ground surface (which is then fused with the SRTM data). Several studies have investigated the penetration of vegetation canopies by C-band radar. Wegmuller *et al.*, (1997) investigated vegetation effects on ERS data, Treuhaft *et al.*, (2000) evaluated penetration of vegetation canopies using AIRSAR data, and Dobson *et al.*, (1995) did the same for SIR-C data.

Ideally, the original LiDAR point data should be segmented to filter out the vegetation and leave building structures in, yielding a DEM of the impervious surface on which floodwaters could flow. However, the LiDAR data provided by the International Hurricane Research Center (IHRC) at FIU had already been filtered and gridded into DEMs. The DEMs that were distributed consisted of a LiDAR Top Surface (LTS) product and a LiDAR Bottom Surface (LBS) product (IHRC, 2004). The LBS had been filtered in order to remove both vegetation and buildings from the LTS. Therefore it only contains elevations from the underlying topographic surface (Zhang *et al.*, 2003).

In order to fuse SRTM data with the other topographic data, we must specify values for R in the MKS state-space model. We cannot simply use the specified SRTM value in Table 2-1 if we desire optimal estimation of the elevations since that value is not landscape-dependent. A reasonable approach instead is to use the sample variance of the differences between SRTM and

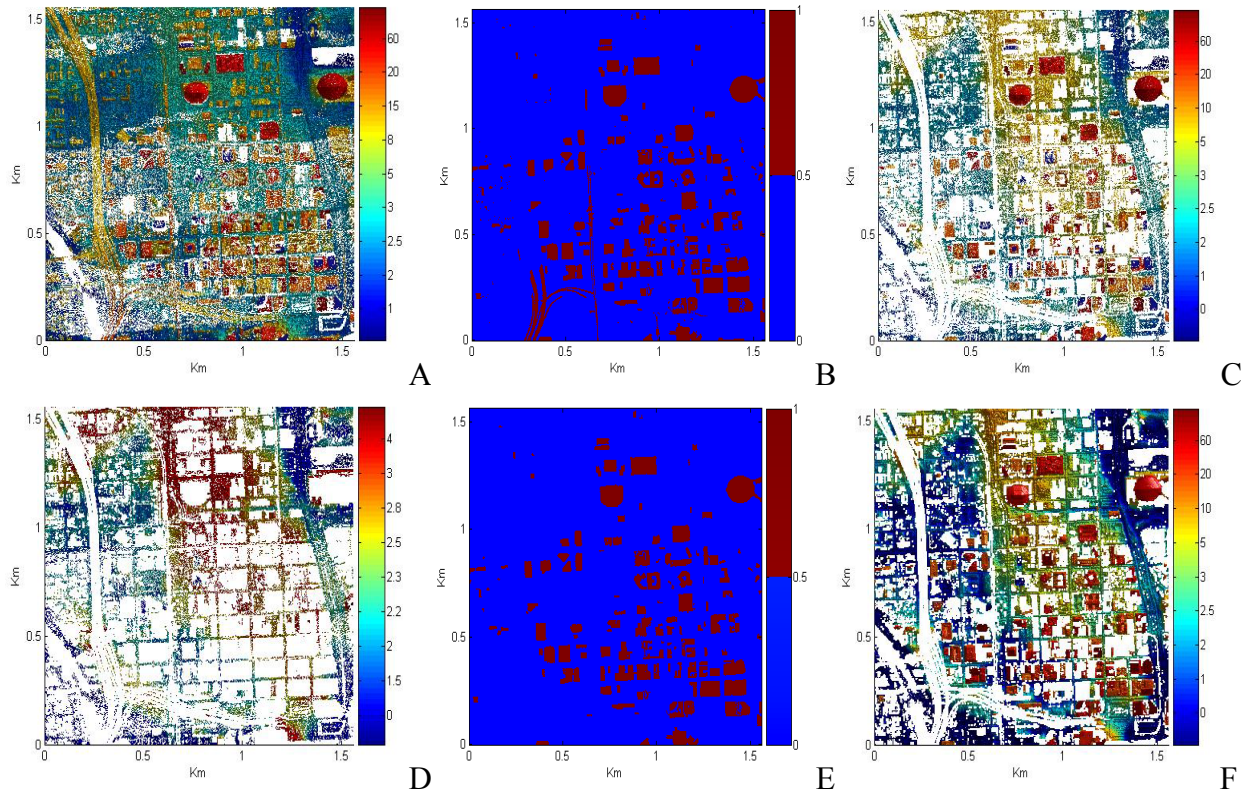


Figure 3-3. Example of generating a DEM from LBS+ LiDAR data over the $1.5\text{km} \times 1.5\text{km}$ urban test site. A) LTS point data. White spaces denote data voids and dropouts due to the high acquisition altitude and low-reflection surfaces. D) LBS point data, where white spaces denote voids and removed elevated surfaces. B) classification of LTS using a 15m height threshold followed by a 3×3 median filter, where unity values represent elevated structures. E) refined classification after applying region properties to remove bridges and elevated roads. C) LBS+ point data obtained by adding buildings to LBS that were extracted from LTS using the classification. F) LBS+ gridded to form a 5m DEM. White spaces in the final LiDAR DEMs denote vegetation and elevated structures under which flood waters can flow, very short buildings, or data voids due to low-return surfaces. The subsequent MKS data fusion fills in these voids using the other data types. All elevations are in meters.

the LiDAR data over different landscapes. However, we cannot derive a good measurement uncertainty (R) value for SRTM with either LTS or LBS individually. Since SRTM blurs the closely packed urban buildings, if we use $|LTS - SRTM|$ to derive R for SRTM, uncertainty will be relatively large where there are buildings due to the deviation of SRTM elevations from the building surfaces. Over vegetation, R would be largest where SRTM penetrates the

vegetation the most. This is undesirable because it would cause the SRTM values to be under-weighted in the MKS algorithm where it penetrates deep into vegetation (and almost reaches the ground), and it would be over-weighted where there was little penetration of the vegetation. The converse is also true; by using $|LBS - SRTM|$ to derive R for SRTM, the values would resemble the desired trends over vegetation and would be skewed over building areas.

To estimate our hydrologic surface for comparison with SRTM, a data set with combined information from the LTS and LBS data is therefore needed. We create a new LiDAR DEM, which we denote as LBS+ (Figure 3-3), consisting of the LBS data combined with the re-inserted building structures. In order to extract the building data and create the LBS+ DEM, we apply a simple segmentation procedure to the LTS data. A binary threshold of 15m is applied to the LTS elevations, followed by a 3×3 median filter to reduce spurious high points and refine building edges.

Elevated highways and bridges were observed in the resulting DEM. Since water can generally flow under these structures, we wish to omit them from our building mask. We therefore applied the morphological filter described in (Gader *et al.*, 2004, Gonzalez *et al.* 2002) in order to exclude elongated structures like bridges. The algorithm was run with the following parameters: eccentricity >0.99, solidity <0.2 and area <50. The mask was then applied to add the building structures to the LBS DEM and form the LBS+ DEM. Using the LBS+ surface, the Kalman innovations at the SRTM scale yield the expected trends, namely smaller R values for SRTM over vegetation the more SRTM penetrates the vegetation. They also yield larger R values for the SRTM measurements over tall buildings, as SRTM underestimates the true building heights due to the fact that a single SRTM pixel is so large (30 m × 30 m).

3.3.2 Assessing the Measurement Error Variance of SRTM

Before we can optimally combine the datasets in the MKS framework, we must account for the spatially-varying measurement error in the SRTM data. This is particularly important over the land surface since there are many anthropogenic structures that cause heights derived from side-looking radar to deviate markedly from the actual land surface elevations. In addition, each SRTM scene is actually a weighted average of many individual radar sub-images that only cover part of the radar swath (Hensley, 2005). Thus, we focus on estimating the measurement error variance of the SRTM as a function of landscape and land-use.

To assess SRTM measurement error, we employed a stochastic approach that uses the MKS innovations at the SRTM scale. Since the stochastic estimation in the MKS algorithm is statistically optimal, we choose to use it instead of deterministic differencing, which simply measures the height differences between LBS+ and SRTM. Three representative landscape



Figure 3-4. Three studied sites extracted from Dade County, Florida (Miami metro area) to evaluate SRTM accuracy. Coastal (Longitude W/Latitude N): $80.183^{\circ}\sim 80.198^{\circ} / 25.762^{\circ}\sim 25.776^{\circ}$. Urban: $80.200^{\circ}\sim 80.211^{\circ} / 25.762^{\circ}\sim 25.776^{\circ}$. Rural: $80.472^{\circ}\sim 80.487^{\circ} / 25.612^{\circ}\sim 25.626^{\circ}$.

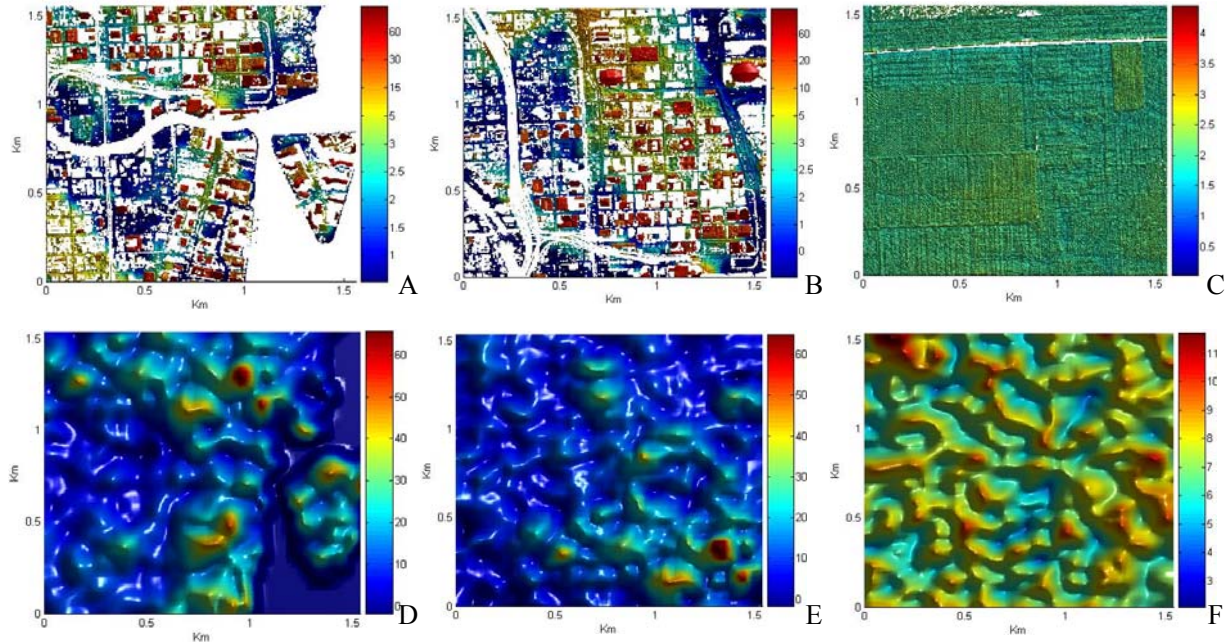


Figure 3-5 DEMs obtained from LIDAR (A, B, and C) and SRTM DTED-2 (D, E, and F) over three distinct terrain types. From left to right, the terrain types are coastal urban, urban, and rural. 1.5 m scale LIDAR DEMs are derived from LBS+ points. The SRTM DEMs are resampled from 1 arc second (roughly 30m) spacing to 24m to correspond to integral powers of 2 scale levels in the MKS quadtree data structure. Each area is $1.5\text{km} \times 1.5\text{km}$. All elevations are in meters.

archetypes are chosen for error analysis from the Dade County study area. They are urban, coastal, and rural (Figures 3-4, 3-5). The number of archetypes was limited to three to reduce the chance of over fitting to a particular study area and thus to keep the estimator generalizable.

The MKS innovations represent the difference between the SRTM data and the *a priori* estimates from the MKS estimator (Figure 3-6). We examined the first and second order statistics of these stochastic differences (innovations), including their 2-D autocorrelation function (ACF). We verified that over a single land-use/land-cover archetype, such as “rural”, the ACF plots indicate the innovations do not exhibit strong spatial correlation (see Figure 3-6). This suggests they can be well approximated as wide-sense stationary and that Kalman based data fusion should perform well since the noise term in the MKS measurement equation is assumed to be white. Another important characteristic is that the measurement error varies

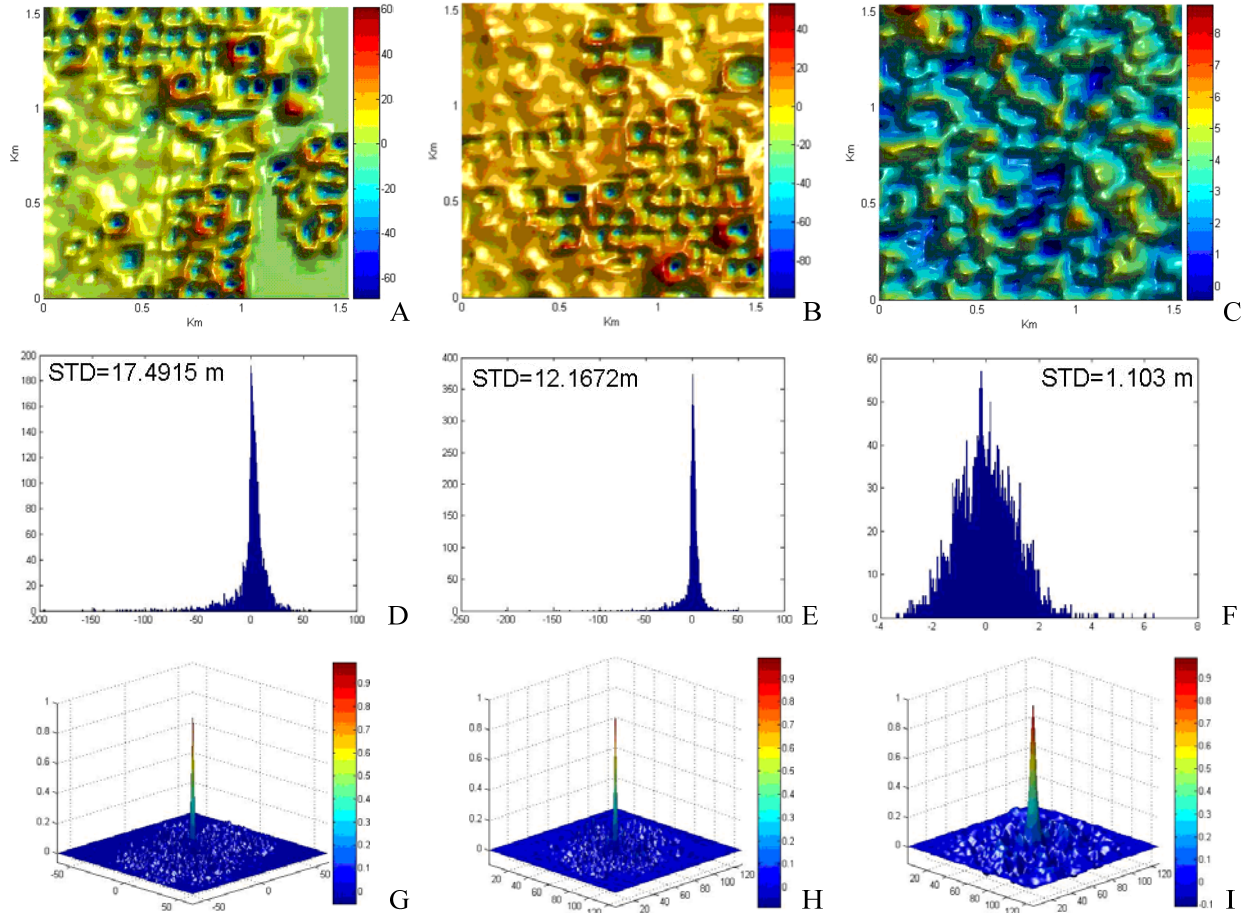


Figure 3-6. Kalman filter residuals (innovations) for the three terrain types in Figure 3-5 used to assess SRTM accuracy. The Kalman residual is the *a priori* estimate (predicted observation) subtracted from the actual observation. Thus, the residual is negative at the centers of tall buildings since the prediction based on LiDAR is higher than the SRTM elevation. Large positive values result just outside the perimeters of tall buildings where the blurred building signal is still present in the SRTM data. From left to right, the terrain types are coastal, urban, and rural. A, B, C) innovations. D, E, F) histograms of the normalized innovations (innovations minus their mean). G, H, I) autocorrelations of the normalized innovations. All innovations are in meters.

noticeably between the three terrain archetypes. Using the three simple terrain archetypes, we were thus able to establish the need for a spatially-dependent R for the SRTM data.

We then used the same concept with a slightly expanded list of classes to estimate R over the study site. Since land in southeast Florida is generally flat, variation in terrain type is largely dependent on the density of anthropogenic structures and proximity to the coastline. The effect

Table 3-3. Estimated measurement error standard deviations \sqrt{R} for SRTM for the aggregated terrain types in the study area.

| Class | Terrain type | SRTM rms measurement error |
|-------|--------------------------------|----------------------------|
| 5 | Urban (tall buildings) & coast | 17.5 meter |
| 4 | Urban (tall buildings) | 12 meter |
| 3 | Suburban & coast | 10 meter |
| 2 | Suburban | 5.5 meter |
| 1 | Rural (low relief) | 1.1 meter |
| other | unclassified | 8 meter |

of the coastline is to split a given subtree in the SRTM DTED-2 data into a terrain portion and a flat non-terrain portion (except the case for rural sites, where flat terrain predominates both in land and in water.) We therefore expanded our initial list of three terrain archetypes into six classes (shown in Table 3-3): urban, urban adjacent to the coast, suburban, suburban adjacent to the coast, rural, and unclassified, in which no specific information about terrain type could be derived. SRTM elevations were found to be very accurate when highly localized features associated with urban development were minimally present, such as in rural areas. Following the same procedure described for estimating R where LiDAR is present, we estimated R over the six major landscape classes (Table 3-3) based on expected building size and density and the presence of the coastline. This process was applied only in regions where LiDAR data were available.

We then took a landuse/landcover (LULC) shape file supported by South Florida Water Management District (SFWMD) that covered the entire area, including areas where no LiDAR data were acquired and aggregated the LULC units into these same six classes (Figure 3-7). The trained R values for the six classes were then assigned throughout the entire region in $1.5\text{km} \times 1.5\text{km}$ tiles. The choice of 1.5km for assigning R values was dictated by the smallest number of

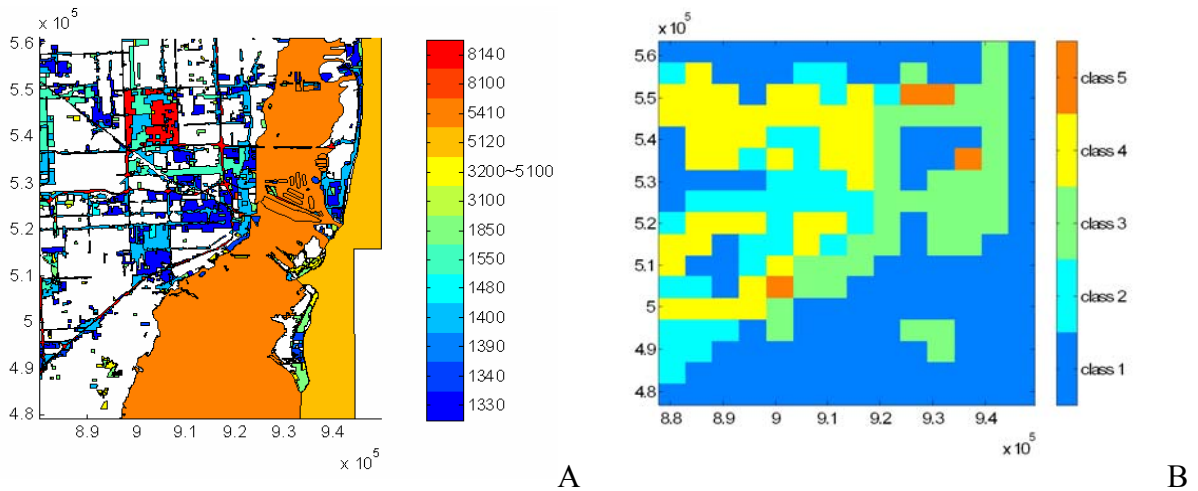


Figure 3-7. Error variance mapping depending on the density of urban development. A) LULU shape file of the Miami area produced by the South Florida Water Management District. Classes ranging from 1300 – 1600 represent high density urban development. Classes in the 1800s and 8000s represent intermediate density urban development. Classes in the 3000s represent lower density development. Classes in the 5000s represent water bodies. White space represents unclassified areas. Class numbering details can be found in (SFWMD, 1999). Original UTM coordinates of feet used here. The area is roughly 21km \times 21km. B) Corresponding area showing five aggregated terrain classes corresponding to Table 3-3. Classes were aggregated into 1.5km \times 1.5km tiles because the SRTM measurement noise is assumed stationary over such distances. Although, the noise may not actually be stationary over such distances, the tiles must be sufficiently large to allow for the robust calculation of the innovation statistics.

SRTM pixels in a given dimension (e.g., University Transverse Mercator (UTM) easting or northing) that could consistently provide a robust estimate of sample variance and autocorrelation. For water bodies in the SRTM data, the MKS mapping operator is set to zero ($H = 0$). Thus, the R value for SRTM has no effect on MKS estimates over water bodies.

3.3.3 Big Measurement Error of SRM over the Coastline

Accurate delineation of the coastline is critically important for coastal flood modeling. Furthermore, the coastline in this area exhibits many small-scale variations, particularly near developed areas such as marinas, canals, and modified shorelines. Discerning the coastline in SRTM is problematic due to its coarse resolution. Thus, SRTM heights near the coastline are

expected to have large uncertainties, and it is desired that the MKS fusion track the high-resolution LiDAR data very closely over the coastline.

In coastal pixels where LiDAR is present, we want to ensure that the estimated R values for the SRTM will have minimal effect because the MKS estimates should still be dominated by the small- R LiDAR pixels below. In coastal pixels where there are neither topographic nor bathymetric LiDAR pixels present, the estimated R value for the SRTM should have a stronger effect. Therefore we need a way to inform the algorithm when it is over coastal pixels so that the R for the SRTM can be increased to better reflect the poor elevation quality in the SRTM over coastal pixels, yet the adjustment should be small enough for the SRTM to influence the MKS estimates in the absence of LiDAR data. As a result (Figure 3-8 C) the coastline pixels in the SRTM are delineated, and we increase the R values of the SRTM to a value of 100 (a value that was determined experimentally to be sufficient) to affect these changes.

First, we classified the down-sampled LiDAR and SRTM by height, such that a logical “1”

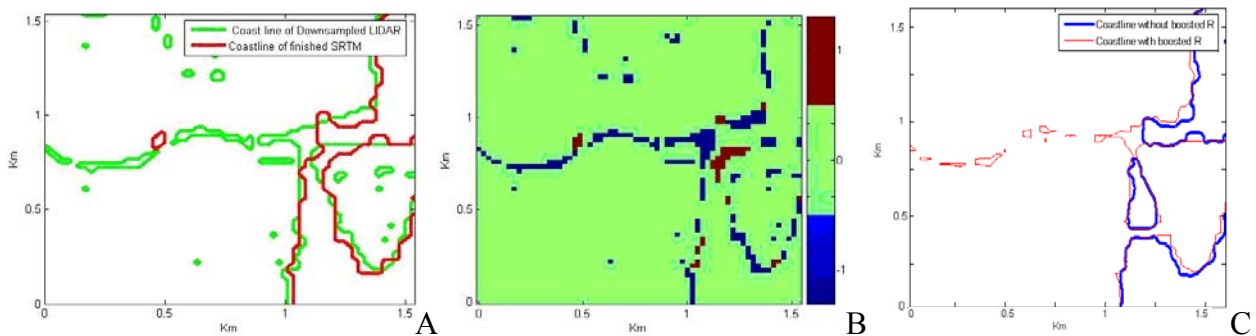


Figure 3-8. A $1.5\text{km} \times 1.5\text{km}$ coastal site shown at the SRTM scale (24m). A) coastlines derived from the downsampled LiDAR and SRTM. B) Differences between classified LiDAR and classified SRTM. Red represents pixels where the LiDAR indicates land and SRTM indicates water. Blue represents the converse. Green indicates the same class in both LiDAR and SRTM. C) Corresponding coast line in the MKS data fusion result at the SRTM scale using both the nominal (constant) measurement noise variance R for SRTM and the terrain-dependent boosted R . Compared to the SRTM coastline in the plot on the left, the coastline in the fused data at the SRTM scale is able to track the LiDAR coastline more closely.

corresponds to land (elevations above -0.05m), and a logical “-1” represents sea water (elevations below -0.05m). We then calculated the difference between classified LiDAR and classified SRTM (Figure 3-8 B). Results are shown with areas of coloration representing pixels (Red : Water in SRTM/Land in LiDAR, Blue : Land in SRTM/ Water in LiDAR, Green : Land in SRTM and LiDAR or Water in SRTM and LiDAR) R was increased only where the LiDAR indicates water and SRTM indicates land since only SRTM land pixels are used in the MKS fusion..

3.3.4 Results

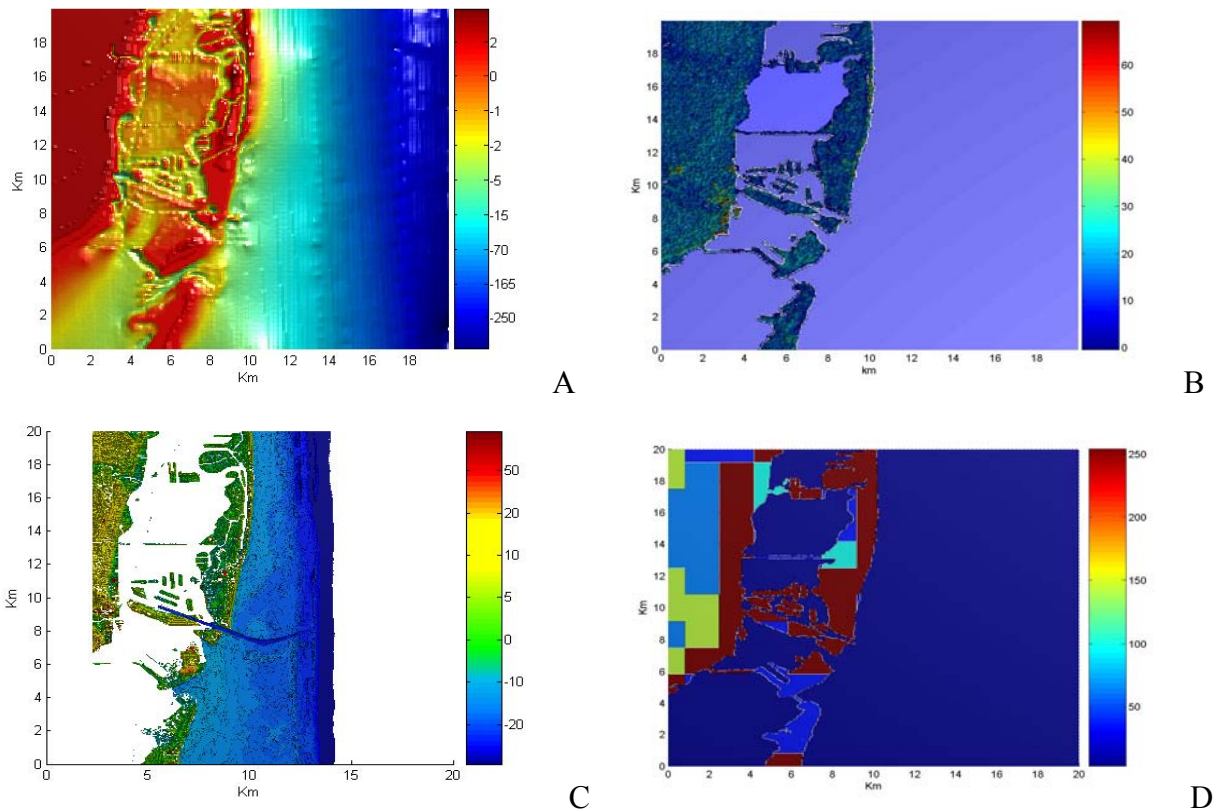


Figure 3-9. Component data sets to be fused together over a $20\text{km} \times 20\text{km}$ area: A) bare surface NGDC elevations (80 m spacing) showing deep water bathymetry and land surface topography on a non-linear color scale; B) SRTM elevations (20 m spacing); and C) LBS+ and bathymetric LiDAR elevations (5 m spacing). D) SRTM measurement error variance R estimated as a function of landuse class corresponding to Figure 3-7. R has units of meters squared. Over the ocean, R values for SRTM have no meaning since $H = 0$ there.

We fused the NGDC, SRTM, bathymetric LiDAR, and topographic LBS+ data sets with the MKS estimator (Figure 3-9). Since we wish to estimate solid surface elevations, the SRTM pixels containing ocean were treated as missing data by setting measurement-state model operator zero, $H=0$. Similarly, topographic LiDAR pixels over the water were excluded from the fusion.

Table 2-1 shows the nominal measurement error for each data set. The SRTM measurement error was modulated by terrain type. As described previously, the SRTM measurement error over areas containing topographic LiDAR data was determined from the

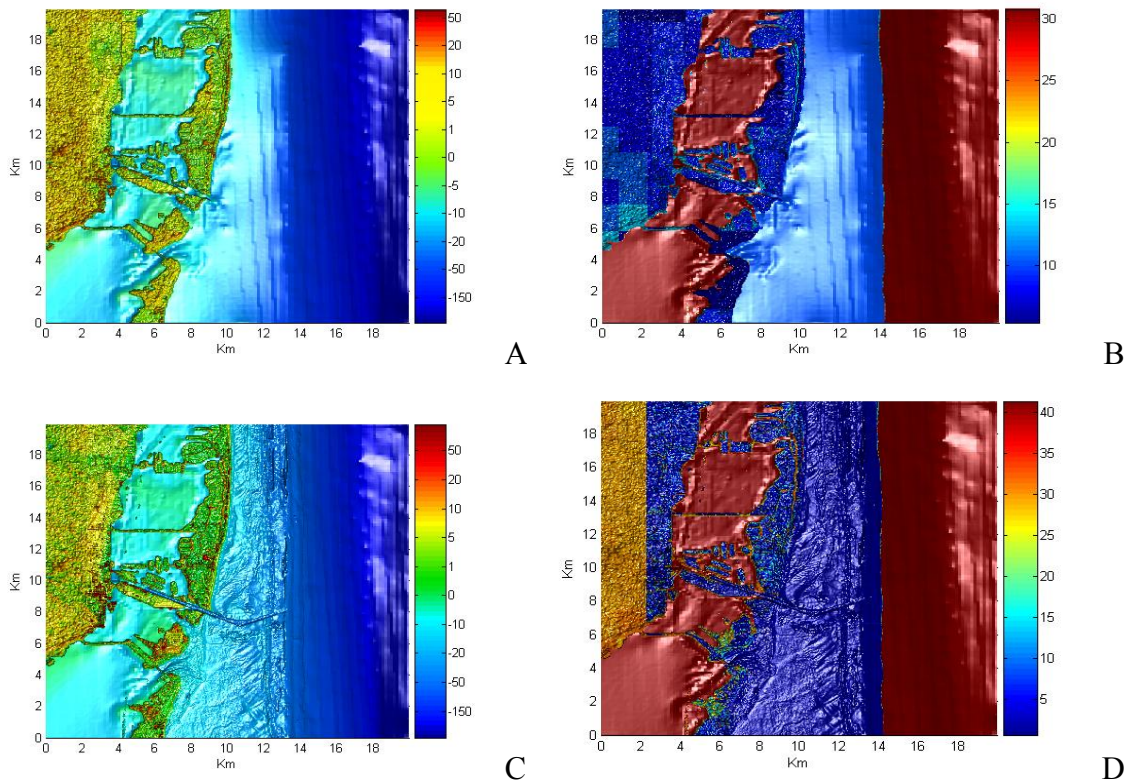


Figure 3-10. MKS fusion results for the $20\text{km} \times 20\text{km}$ area. (A) Fused estimates at SRTM scale (20m). (B) Standard deviation of the expected estimate error \sqrt{R} at SRTM scale (in meters). (C) Fused estimates at LIDAR scale (5m). (D) \sqrt{R} at LIDAR scale. Dark red indicates high uncertainty in areas where only NGDC data were available. Yellow indicates intermediate uncertainty where SRTM data were available. Dark blue indicates low uncertainty where LIDAR data. All elevations and \sqrt{R} are in meters

MKS innovations adaptively. For areas with no LiDAR data, aggregated LULC classes were used to propagate spatially-dependent R values (Table 3-3). The largest root mean square (RMS) values occur where tall buildings lift the SRTM phase scattering center above the ground. A value of 8m is used for unclassified terrain types because it is the median value between the nominal bounds of 6m and 10m listed in Table 2-1.

The original grid sizes of SRTM and NGCD were 30 m and 90 m, respectively. Since the MKS quadtree requires integer scale changes, the SRTM and NGCD were upsampled to 20 m and 80 m, respectively. Prior to the MKS fusion, the bathymetric LiDAR was upsampled to 5m and combined with the 5m topographic LiDAR data since the coverage areas were small and mutually exclusive. The fused elevation estimates and the square root of the Kalman estimate error variances are shown in Figure 3-10 at both the SRTM and LiDAR scales.

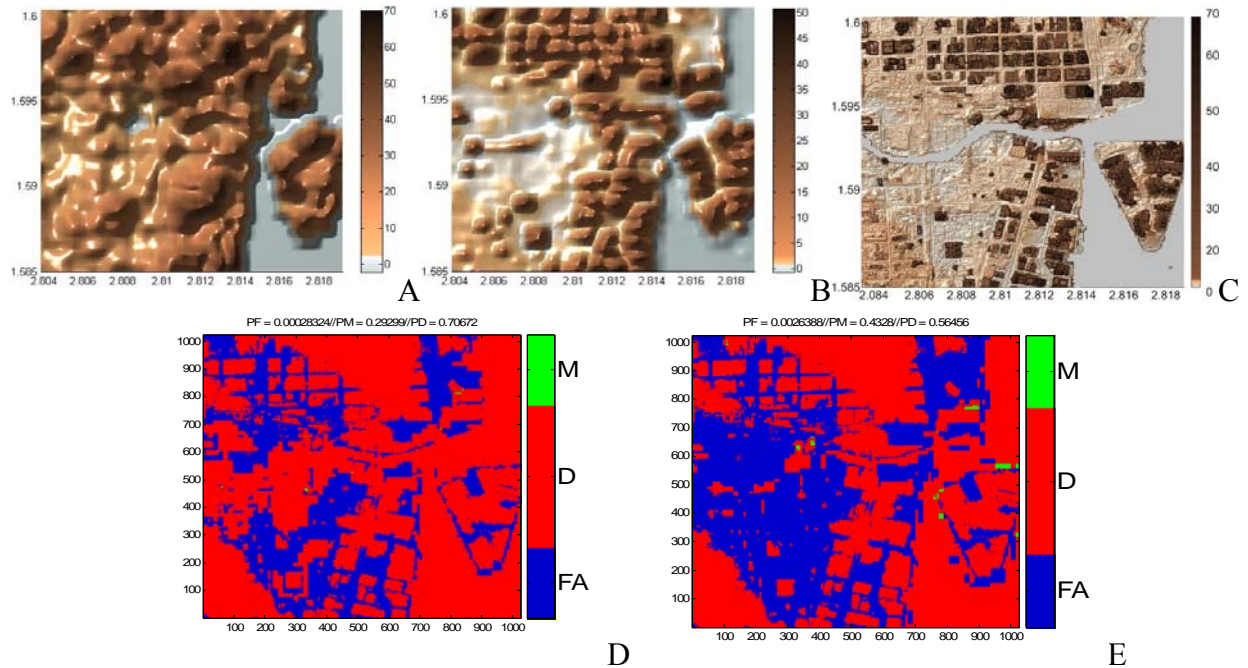


Figure 3-11. Two-meter simulated flood images over the 1.5km \times 1.5km coastal site. A) SRTM data (20m). B) MKS fused estimate at SRTM scale (20m). C) fused estimate at LiDAR scale (5m). Black color indicates simulated flooded area. Elevations are in meters. D) The flood estimate error with SRTM data, FA (False alarm) rate is 0.0026, M (Missing) rate is 0.4628. E) The flood estimate error with coarse scale fused DEM, FA rate is 0.00028, M rate is 0.2929.

To further elucidate the benefits of fusing LiDAR and SRTM data, a simulated 2m flood level is depicted in Figure 3-11. The flood routing prediction using the fused DEM at the LiDAR scale is much more precise than that obtained from non-fused SRTM observations alone. It is interesting to observe that even at the SRTM scale, the prediction is dramatically improved through the data fusion. To quantify the improvement, we calculated the false alarm (no flood in LiDAR scale flood model / flood in coarse scale flood model) and miss (flood in LiDAR scale flood model / no flood in coarse scale flood model) rates by considering the 2 m simulation result over the finest scale data as truth (Figure 3-11 D and E). In addition, the MKS estimate error images in Figure 3-11 provide an uncertainty measure for every pixel at every scale in the quadtree that reflects the quality of data available at that pixel. Such uncertainty measures are needed for sound decision making in response to and mitigation of flooding hazards

CHAPTER 4 MULTISCALE FEATURE REDUCTION FOR HYDROLOGIC MODELING OF URBAN AREAS

4.1 Introduction

Due to population growth and development in coastal areas, eight of the ten largest cities in the world are located on the coast and 44% of the world's population lives within 150 km of the ocean (Resio, *et al.*, 2008), resulting in increased natural hazard risks that must be accurately estimated. Modern ranging sensor technology, in particular airborne LiDAR, enables the formation of DEM images with pixel resolutions of 1m x 1m or smaller. Such data sets should, in principal, improve our ability to accurately monitor, predict and mitigate coastal flooding and erosion (Shrestha *et al.*, 2005). Yet, the flood and storm surge modeling communities struggle with how to incorporate high resolution data into their flood predictions (Bates *et al.*, 2004). In general, the physical phenomenon of fluid dynamics in such models is expressed by non-linear, coupled, time-varying differential equations, and the terrain and land cover (buildings and vegetation) comprise a set of complex boundary conditions. The fundamental equation for fluid dynamics is the well known Navier-Stokes Equation (Acheson *et al.*, 1990), but from it many specialized equations are derived to predict water level, velocity, and momentum. For all but the simplest geometries and momentum conservation assumptions, these equations offer no closed form solution, thus requiring computationally intensive numerical solutions. Solving the equations iteratively for many possible water flow directions at every pixel in a very large DEM often leads to unacceptable computation times, particularly because multiple realizations are often desired for each storm scenario. A 1 km \times 1 km area with 1 m resolution would require up to one million nodes at this resolution if a regular grid is used. In order to reduce the computation time, modelers are often forced to use DEMs with large (coarse) resolution, and accept the errors in flow routing and discharge predictions that result from the degraded boundary condition

information. Alemseged *et al.* (2005) concluded that relatively low resolution DEMs can yield useful 2D models in areas of relatively simple topography, such as rural settings. They found that the calculation times for estimating inundation levels with the SOBEK flood model over a few tens of square kilometers ranged from a few hours to 13 days for gridding (pixel) resolutions of 15 m and 2.5 m, respectively, on a 1.5 GHz Pentium IV PC. Herritt and Bates (2007) studied the impact of varying spatial resolution from 10 m to 1000 m over larger areas to evaluate their raster-based model of flood flow and concluded that resolutions as coarse as 500 m were adequate for predicting water levels in some rural areas. 500 m is far too coarse for urban areas however, and the flood modeling community still lacks a general method to balance the need for accuracy against computation time.

In modern storm surge models, such as ADCIRC (Luettich *et al.*, 2006), irregular mesh grids are generated to represent the terrain since they can reduce information loss and storage requirements by adjusting the density of the mesh depending on the amount of variation in the data. One must realize, however, that a non-uniform grid only offers significant savings if you have large areas in your DEM of low topographic relief and few buildings. In areas where most of the hydrologic surface has a lot of detail, as it does in most cities, the potential savings of a non-uniform grid is mostly lost and you are back to having to increase the average node spacing to a distance that is computationally feasible but lacks accuracy (Shephard *et al.*, 1983). Also, the very same irregular node spacing used to balance between information loss and the computer storage can cause high computational complexity in the actual hydrologic models in that every pixel must be indexed with the particular locations of its irregularly connected neighbors. This also presents a difficulty in fusing data of different resolutions (Wilson, 2004). Considering these issues, we use a regular grid in implementing our hydraulic model. That is not to say that the

methods used here could not be adapted for use on an irregular grid, but rather the implementation on a regular grid makes the impact of our decomposition method easier to understand.

To minimize the number of pixels included in the computations, we exclude the data that fall inside footprints of buildings in running the hydraulic model. Schubert *et al.*, (2008) refer to this approach as the Building-Hole (BH) method and compared it to the Building-Block (BB) method, in which the terrain height is raised where buildings coincide with the mesh. Their study concluded that the accuracy of BH and BB are similar; however, the computational time for the BH approach is shorter

In some cases, *ad hoc* methods of manually specifying sub-pixel boundary conditions have been used. However, these are highly specific to the particular flood model used (e.g. SLOSH, ADCIRC), as well as highly inefficient and subjective (Bates *et al.*, 2000). What is needed is a principled and systematic method for preserving information in the high resolution DEMs that can be used at coarser resolution in the models. Ultimately, the scale must be decided by the modeler's tolerance for error, but we present some guidelines for choosing a proper scale by considering a balance between performance error and computational requirements. In DEMs of urban areas, the exterior walls of buildings and the ground (including paved area) form the surface over which flood waters flow. However, these two components of the hydrologic surface often exhibit very different spatial frequencies. Much of the information contained in the landscape topography, such as hills and valleys, is spatially correlated over hundreds of meters to kilometers (i.e. low frequency). This is particularly true for cities on coastal plains where the topographic relief is quite small. Examples of such cities in the United States include Houston, TX; New Orleans, LA; Miami, FL; and Jacksonville, FL. It is precisely such low-relief urban

areas that are at greatest risk for wide spread flooding and devastating storm surge. In contrast, the buildings in these urban areas represent high (typically on scales of meters to tens of meters) frequency information. As a result, it is sub-optimal to reduce the spatial resolutions of these two components of the hydrologic surface uniformly, as happens when a high-resolution LiDAR DEM is naively down-sampled equally over the entire study area.

We present a method for decomposing the hydrologic surface into these two distinct components and then reducing them independently. As further motivation for this approach, we present the evidence of the validity of decomposing a mixture distribution into its component distributions to preserve more information (Cover *et al.*, 1991). If viewed as a lossy data compression problem, the entropy of the mixture distribution is guaranteed to be greater than or equal to the mixture of the component entropies. This implies that reducing the resolution of the DEM components separately preserves more information.

While still a relatively new topic, some approaches to encoding the impact of buildings in flood or surge routing have been explored. For example, the concept of porosity (Chow *et al.*, 1988) can be used to handle the effects of buildings in coarse DEMs. Alemseged *et al.*, (2005) suggested that buildings could be defined as hollow, partially solid, or entirely solid objects depending on the percentage of building area and ground area at any given resolution. The resulting effect of a building is the same in every direction and for any water depth. This approach is incomplete if we consider an elongated building or narrow channels between buildings, wherein water flows predominantly in one direction. Neelz *et al.* (2007) presented preliminary results from the 2D flood model TUFLOW with high resolution data, coarse resolution data, and coarse resolution data with an increased roughness value (based on increasing the Manning coefficients) and mentioned that the overall effects of buildings in urban

areas should be considered. Unfortunately, that method cannot be used generally because the roughness value is actually affected by water depth.

In this dissertation we show that a new friction value can be efficiently computed by combining the drag force of buildings with shear stress of the ground, including its dependence on water depth.

4.2 Decomposition

Our study region comprises the urban area of Miami-Dade County, Florida. Our finest scale DEM of the study area was generated at 1m spatial resolution from LiDAR data. This data set was chosen because the density of LiDAR points is representative of typical LiDAR acquisitions over urban environments. In such data sets, it is not uncommon to have small data voids due to low-reflectance water surfaces and shadowing from buildings and trees. In this work, the LiDAR voids and areas of no LiDAR coverage were filled in by fusing the LiDAR data with a coarse resolution (30m) dataset from SRTM by using MKS (Slatton, Cheung *et al.*, 2005). A subset of the area is shown in Figure 4-1, where the size of a pixel is 1m x 1m. The data format of the LiDAR consisted of two surfaces, the LTS and LBS surfaces, as mentioned in section 3.3.1. The LiDAR DEM is a simple data structure, with every pixel having a single elevation value. Buildings are considered as the sole dominant hydrologic feature in dictating flow of water due to the sparsity of vegetation in the urban area (as well as the predominantly narrow trunks of vegetation in this region, which do not provide resistance to fluid motion) Hence, to better estimate the hydrologic response (e.g. water discharge rate), we only include the building and ground information to form a hydrologic surface.

The region property filter (`regionprops()`) built in Matlab was used to help estimate the hydrological surface for flood or surge simulation. Initially a scalar elevation threshold was applied to the LiDAR elevations to generate a binary image composed of ground and non-ground

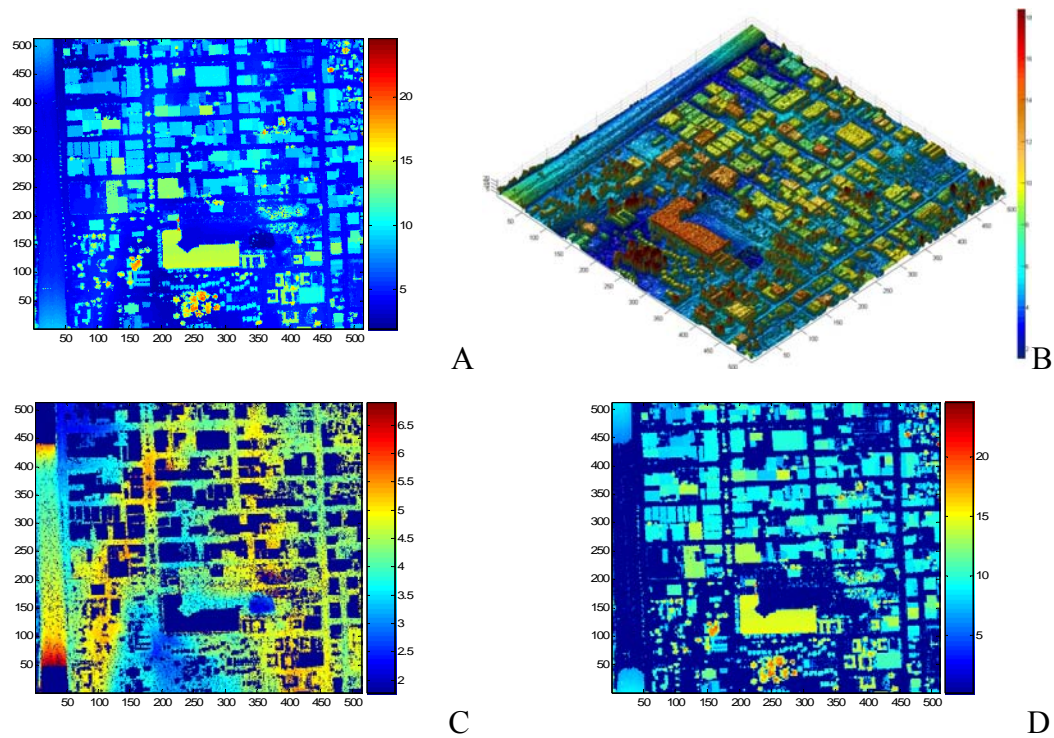


Figure 4-1. Ground and non ground DEM of LiDAR A) Fused DEM by MKS in the finest scale,, Top view , B) Shade relief model of the finest scale data, C) ground LiDAR, D) non ground LiDAR. Elevations are in meters

features as we did in section 3.3.1.). Testing this approach showed it to be flawed; if the threshold height was too high, building features were mislabeled while if the threshold was set too low, trees (particularly those adjacent to buildings) were misclassified. In section 3.3.1, this error could be forgiven because exclusion of some building data did not greatly influence the error statistics of SRTM. However, the calculation of hydrologic features is much more sensitive to the accuracy of the exclusion process.

In order to remove vegetation but preserve buildings accurately we applied multiple height thresholds to the LTS. For each discrete threshold (increments of 2 m height), a morphological ‘size of obstruction’ operator was applied to determine if an obstruction was a tree or not. If the size of the object is less than 6 pixels it is considered a tree. The values of the threshold height and the size of obstruction were achieved experimentally to get the best visual agreement with

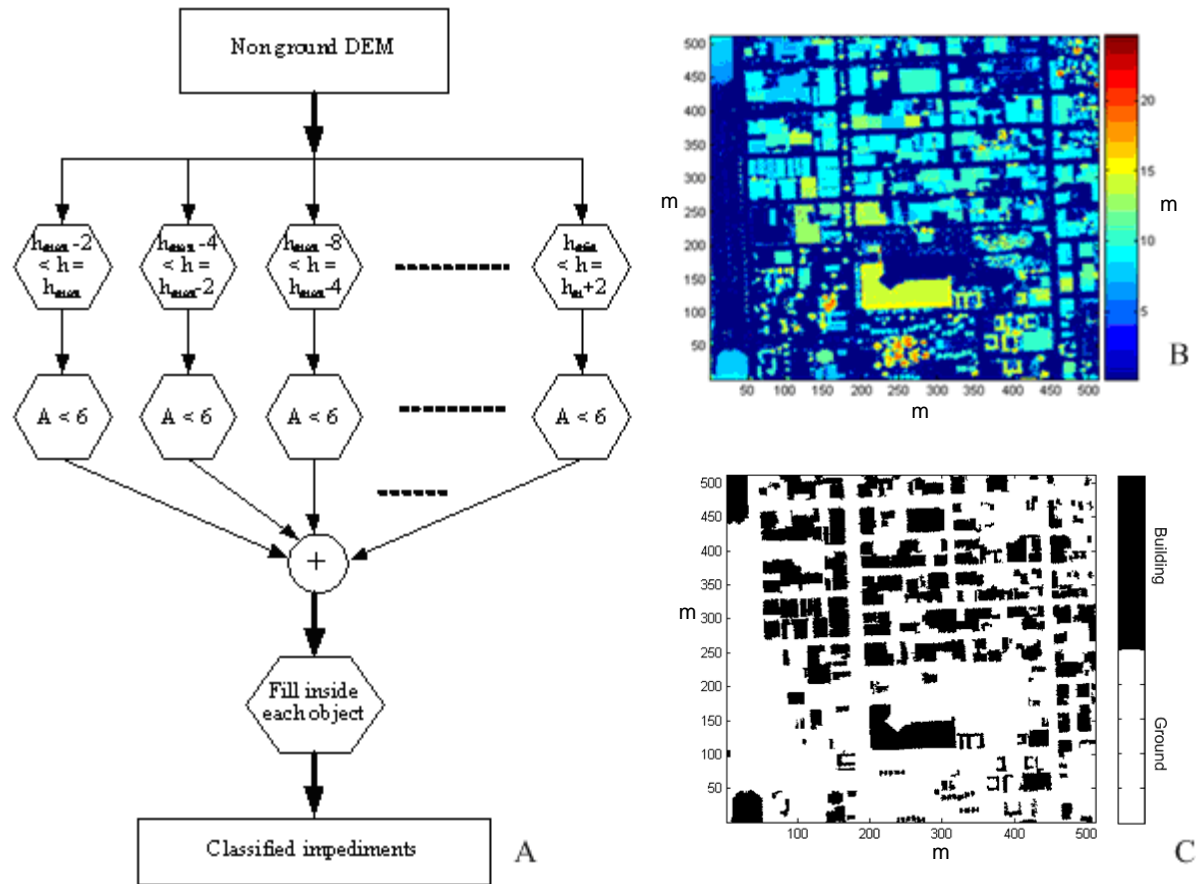


Figure 4-2. Procedure for making hydrologic surface. A) The procedure of morphological filter by multiple threshold heights. B) Non-ground DEM C) Classified impediments where the white pixels represent the area of bare ground or vegetation where water can easily flow. Small impediments such as curbs are still present. Tall impediments to flow, such as buildings, are in black.

aerial images. After filtering the DEM at multiple threshold values through application of the region property filter, the filtered images were then combined by bitwise OR operation. Small holes inside buildings are then filled for each footprint. The procedure and result are depicted in Figure 4-2. It should be noted that more complex methods could have been applied in the segmentation of vegetation and buildings, but since the focus here is on the subsequent scaling of the hydrologic surface, the simple approach used here for producing hydrologic surfaces was deemed sufficient for that purpose.

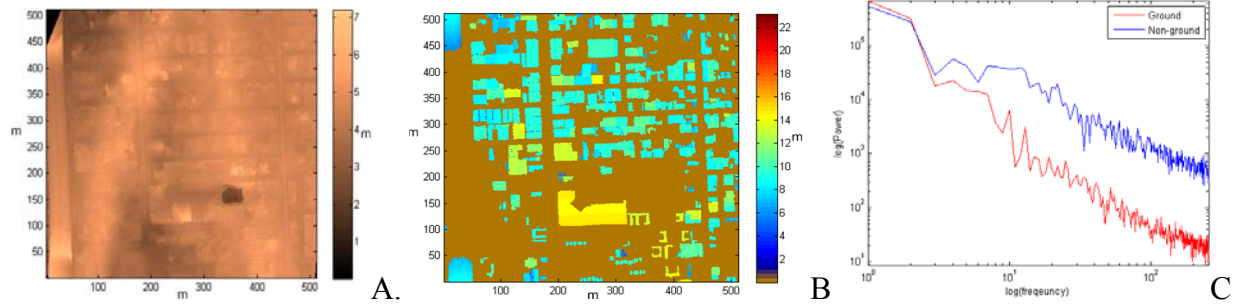


Figure 4-3. Spectral characteristic of ground and buildings, A) Bare ground DEM (interpolated) B) Non ground DEM, C) Power spectral densities of the A) and B).

After creating the hydrologic surface from the LiDAR DEM data, we can decompose the resulting model further, classifying the pixels into ground and building. These two components exhibit very different spatial frequencies as can be observed in the power spectral density in Figure 4-3. C. An approach like downsampling, which would reduce the spatial resolution of both components equally, is therefore not appropriate for preserving information. The implemented method must reduce the components separately.

To illustrate the advantages of separate reduction, we investigate the entropy of a general (hypothetical) mixture distribution relative to the entropy of each component distribution.

Theorem 1. Let z be a random variable (RV) that is distributed as $z = p$ and governed by a mixture model of the three component RVs \mathbf{a} , \mathbf{b} , and \mathbf{c} , such that each component RV is distributed according to a given pdf $\mathbf{a} = p_1$, $\mathbf{b} = p_2$, and $\mathbf{c} = p_3$. We can express the distribution z as

$$p = \lambda_1 p_1 + \lambda_2 p_2 + \lambda_3 p_3 \quad (4-1)$$

where $\lambda_1 + \lambda_2 + \lambda_3 = 1$. We can then write the entropy $H(p)$ as

$$H(p) = H(\lambda_1 p_1 + \lambda_2 p_2 + \lambda_3 p_3) \quad (4-2)$$

By the convexity property of entropy function,

$$H(\lambda_1 p_1 + \lambda_2 p_2 + \lambda_3 p_3) \geq \lambda_1 H(p_1) + \lambda_2 H(p_2) + \lambda_3 H(p_3) \quad (4-3)$$

The lower entropy for the mixed entropies is indicative of the advantage available by separating and processing the components separately.

4.3 Reduction and Scale Selection

In principle, the high spatial resolution of airborne LiDAR observations enables the use of relatively simple hydraulic models to accurately model the flow of water across open terrain in rural areas and in highly developed urban areas. Modelers can also take advantage of the high spatial resolution LiDAR data to compare more complex hydraulic models having higher order terms. However, natural disasters tend to impact relatively large areas. For example, the effective range of Hurricane Katrina was about 200~300 km (Resio *et al.*, 2008). Running meter scale simulations over areas of hundreds of kilometers results in unacceptable computational times, even with the simplest hydraulic models, making it necessary to reduce the spatial resolution of the observational data (Jain *et al.*, 2006)

Historically data reduction in imagery has been achieved by (1) transforming the information into a different domain (e.g. JPEG: spatial to frequency, MPEG: spatial to wavelet) and (2) encoding (e.g. Huffman, run-length coding) to reduce redundancy. Both processes (domain transformation or encoding) transmute important statistical properties of the original data. As a result, the reduced data must be decoded and transformed back to the original domain in order to extract these desired structural features in the image (Gonzalez *et al.*, 2002). The primary advantage of the method proposed in this text is that the reduced data does not require any reconversion to extract the original geometric properties. The ground data are reduced by down-sampling with an approach that preserves the primary characteristic (elevation). Likewise, the desired features of the building data (building width and areas) can be calculated directly

from the two corner point values in the reduced data. This is important because the hydrologic models need to run on the DEM directly. If the DEM had to be fully “uncompressed” prior to running the models, no performance advantage would have been gained.

In addition, basic guidelines will be established for selection of a scale that balances algorithm memory requirements with accuracy of hydraulic feature (water discharge rate) estimation. Though the best scale of reduction will ultimately be decided by the user’s tolerance for error, these guidelines serve as a framework for further investigation.

4.3.1 Ground

In modern storm surge models, such as ADCIRC, irregular mesh grids are generated to represent the terrain heights since their use can reduce data storage by adjusting the node density (mesh resolution) depending on the amount of height variation in the data. However, the non-uniform node spacing leads to high memory usage and computational complexity in the subsequent implementation of the surge model. As a result, minimum node spacings are generally limited to 30 m, and are often much larger (Vemulakonda *et al.*, 1999). Moreover, with this irregular dataset, it is difficult to fuse different resolution data sources (Wilson *et al.*, 2004). If there is significant elevation variation (as in urban or high-relief areas), then this method requires a large number of nodes, and the solution approaches the same number of nodes that a regular grid would require. To more clearly examine the dependence on scale, we use a regular grid DEM, but it should be noted that this work could potentially be extended to non-uniform DEM grids.

For the investigated areas, the quantity of information lost by down-sampling the bare ground elevations usually increases slowly relative to the down-sampling factor because most of the topography in coastal plain cities, like Miami, is smooth (Figure 4-4, B). However, we still require a criterion for deciding the down-sampling factor applied to the ground data for

hydrologic modeling. Generally, the optimal scale selection depends on the requirements of the surge modeler. The cost function we choose to use for selecting optimal scale is

$$TC(s) = (1 - \lambda)G_W + \lambda G_M, 0 < \lambda < 1 \quad (4-4)$$

where

$$G_W(s) = \frac{WDR(N) - WDR(s)}{WDR(N)}, G_M(s) = \frac{MU(N) - MU(s)}{MU(N)} \quad (4-5)$$

and s is the scale (analogous to resolution) and N is the finest scale. $WDR(s)$ and $MU(s)$ are water

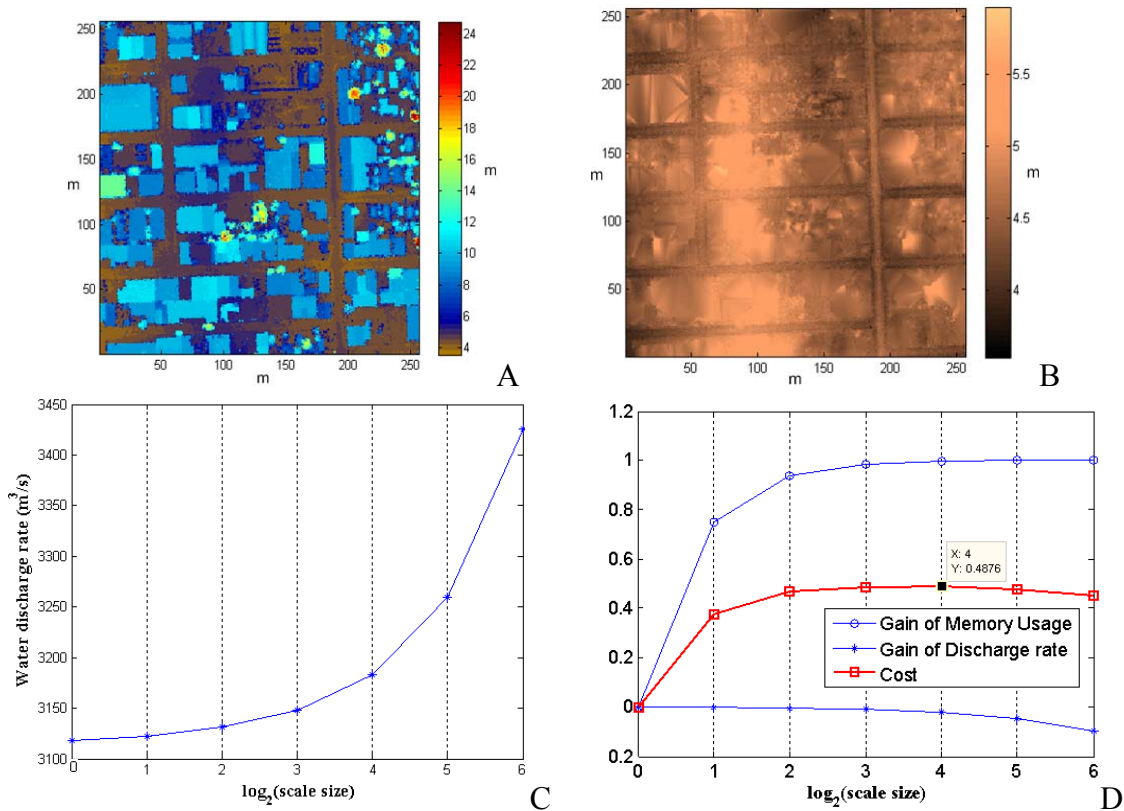


Figure 4-4. Optimal scale selection for ground. A) The finest scale DEM estimated by MKS, B) The filtered and interpolated ground data. The color bar shows the ground heights in meters, and the x- and y-axes units are also in meters. C) Water discharge rate for a wave moving from left to right estimated at multiple scales. The x-axis is in units of the base-2 log of the pixel length in meters. For example, a value of 4 on the x-axis indicates a pixel scale of ($2^4 = 16$ m). In this particular scenario, the discharge rate increases with scale because the ground becomes smoother as resolution is lost. D) Optimal scale selection in terms of the memory usage “gain” and water discharge rate “gain” defined in Eq. 4-5. The cost function curve is then computed using Eq. 4-4. The optimal scale is simply taken to be the scale at which the cost function is maximized. In this case, that occurs at $x=4$.

discharge rate and memory usage at scale s respectively. G_W is the normalized water discharge rate error incurred by decreasing resolution. We refer to this as the negative “gain” for the estimation of water discharge rate. G_M is a normalized difference between the change in memory usage incurred by decreasing resolution. We refer to this as the positive “gain” for memory reduction achieved by decreasing the scale. The choice of λ is left to the surge modeler. If the modelers want to only consider the error of water discharge rate they can set $\lambda=0$. If they wish to give equal importance to memory usage and discharge error, then can set $\lambda=0.5$.

If we consider a particular storm surge scenario of a water wave moving from left to right, not flowing out through bottom and top edges in the DEM shown in Figure 4-4 B, we can compute these gains and evaluate the cost function. For example from Figure 4-4 C, the water discharge rates at $x=6$ (64 m resolution) and $x=0$ (1 m resolution) are $3425 \text{ m}^3 / \text{s}$ and $3125 \text{ m}^3 / \text{s}$ respectively. That yields 9.6 % error in the estimate of water discharge rate if we reduce the resolution to 64 m. With regard to the error in the discharge rate and memory usage, the optimal scale occurs where the TC curve is maximized. For the example in Figure 4-4 D, this occurs at $x=4$, or a scale of 16 m using Eq.4-4 with $\lambda = 0.5$. It is worth noting that the memory usage is closely related to computational time since the local discharge rate should be calculated in every pixel and for all desired directions

4.3.2 Building

Now consider a scenario in which two buildings are spaced closely together, one directly east of the other. Flood waters are flowing from north to south. The water reaches the south side of the buildings by flowing between them. If an overly smoothed or coarse resolution DEM is used, those two buildings may both appear to be shorter and wider (larger footprints) due to local

averaging effects. This implies that the DEM elevations in the channel between the buildings will be erroneously high and skew the modeling result.

The key concept behind the reduction procedure for the building data is that building elevations above the maximum expected inundation level are not important to modeling the flow of water on the hydrologic surface. Additionally, most flood modeling algorithms consider obstructions to water flow as data voids since the flood waters do not enter them in sufficient quantities to affect overall flooding dynamics. Thus, the height characteristics of an obstruction are not used once it is classified as an obstruction. Therefore we only need to preserve information about the footprint of the obstructions.

Building obstructions contain high (spatial) frequency information like edges and corners. One might consider initially using a frequency-domain or wavelet filtering approach to isolate the high frequency spectral components for the purpose of data compression. This would unfortunately tend to emphasize only the edges and corners and not treat the obstructions as solid or “convex” areas through which water cannot flow. A different approach is therefore necessary. Our goal is to maintain the shape of the building obstructions while reducing the amount of memory required for accurate representation of these structures. By considering a building footprint to be a union of rectangles, we can preserve most of the high-frequency information using a simple parameterization. We analyze the elevation data in the spatial domain and locate the two corner points (e.g. the northeast and southwest corners) of the smallest rectangle that circumscribes the building. We therefore maintain sharp edge information with very small memory requirements per building.

The extent to which the building footprints are quantized in this method depends on the scale of the smallest rectangle allowed. Clearly, if one uses large rectangles that enclose several

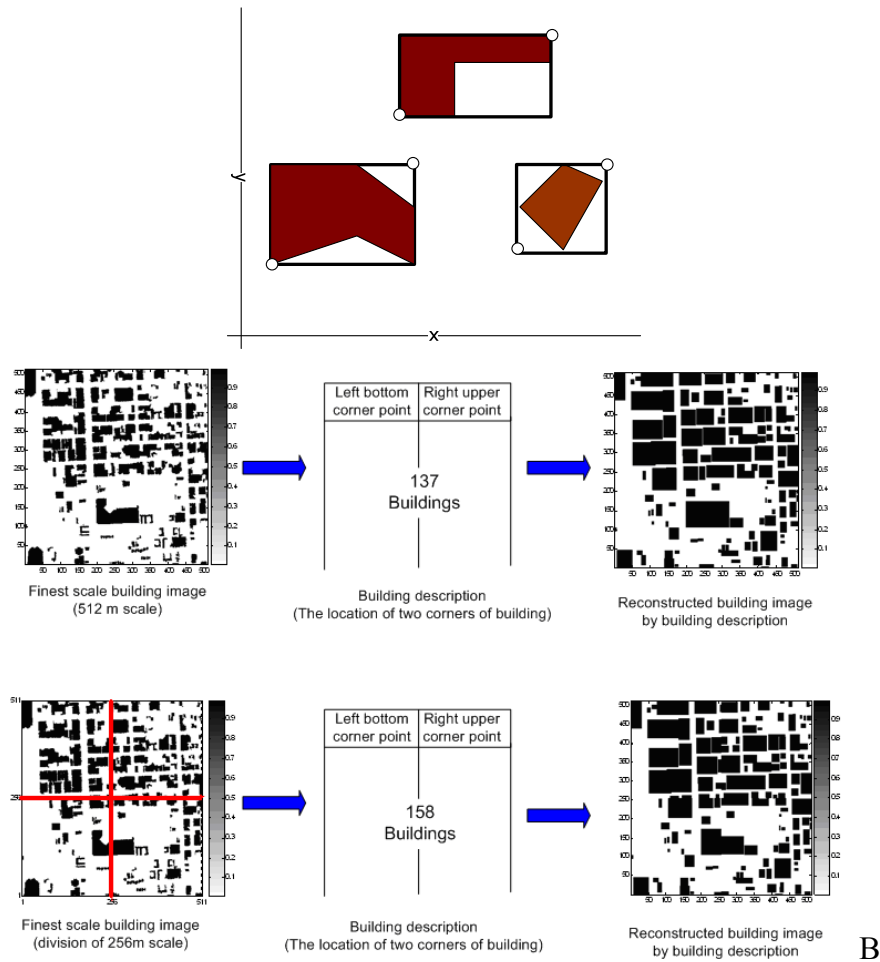


Figure 4-5. Encoding building and scale-division procedure. A) Two corner points of and resulting circumscribing rectangles for three hypothetical buildings. B) The procedure of scale-division method. Initially the entire DEM (512 x 512 in this case) is considered (top row). Subsequently, the scale is reduced by cutting the DEM into quadrants (bottom row). This has the effect of cutting some rectangularized buildings into two or more parts, and the number of buildings increases. . The results show that downsampling for ground-only data and saving two corner points for buildings are very effective for preserving information as a function of scale.

adjacent buildings or very complicated large buildings, a dramatic savings in memory can be achieved; the downside is a large resulting error in the final DEM due to loss of fine detail. To account for the information loss we use a scale-division method. The procedure for the scale-division method is as follows. First each building in the filtered binary image is bounded by a rectangular box. And then the locations of the two corner points (bottom left corner and upper

Table 4-1 Memory requirements for buildings as a function of scale. By comparison, if buildings were not parameterized, the raster representation of a 512x512 image would result in (512×512) pixels \times (2 location indices \times 9 bits per number) = 4,718,592.

| The scale distance (m) | # of buildings or other obstructions | Total number of bits [# of obstructions \times number of points per obstruction (2) \times bits per corner point (2 \times 9 bits)] |
|------------------------|--------------------------------------|---|
| 512 | 137 | 4,932 |
| 256 | 158 | 5,064 |
| 128 | 209 | 5,916 |
| 64 | 294 | 7,428 |
| 32 | 504 | 11,816 |
| 16 | 1033 | 23,628 |
| 8 | 2417 | 29,004 |
| 4 | 6696 | 78,624 |
| 2 | 21226 | 424,520 |

right corner) are saved for each generated rectangle. A new image is then generated by replacing the circumscribed buildings with their rectangular representations. This is initially performed on the entire DEM area. Figure 4-5 shows an example of a 512 x 512 pixel image. Because of the LiDAR DEM resolution (pixels are 1 m x 1 m), this image corresponds to a 512 m x 512 m area. In the demonstrated case, the first reconstruction results in a building map that preserves the streets (channels) that will allow water to flow between buildings. For the subsequent reconstruction (Figure 4-5), the DEM area is quartered in a standard quadtree fashion.

Buildings that fall along the quadrant boundaries are cleaved and treated as two separate buildings. Each portion of the cleaved buildings is parameterized by its own rectangle. The process continues such that with subsequent reconstruction, more rectangles are used and a higher amount of detail information from the original buildings is preserved. As a result, more memory is required to store the corner locations. Table 4-1 shows the memory requirements for the 2-point building descriptions by scale. In order to choose an optimal scale at which to represent the building data, we need to balance the memory requirements with an error metric associated with the quantization of the building footprints. Figure 4-6 demonstrates the effect of

changing the scale of encoded building footprint data on the calculated water discharge rate with same scenario of water movement we used in section 4.3.1. The result agrees with the expected behavior in that we can expect some flow blockages to occur by coarsening the data and joining closely spaced or irregular shapes of buildings. For this case, we can achieve a 99% reduction (107888 bits at 2 m scale division, 912 bits at 256 m scale division) in memory usage at the cost of 27% error ($950 \text{ m}^3 / \text{s}$ at 2 m scale division, $690 \text{ m}^3 / \text{s}$ at 256 m scale division) of water

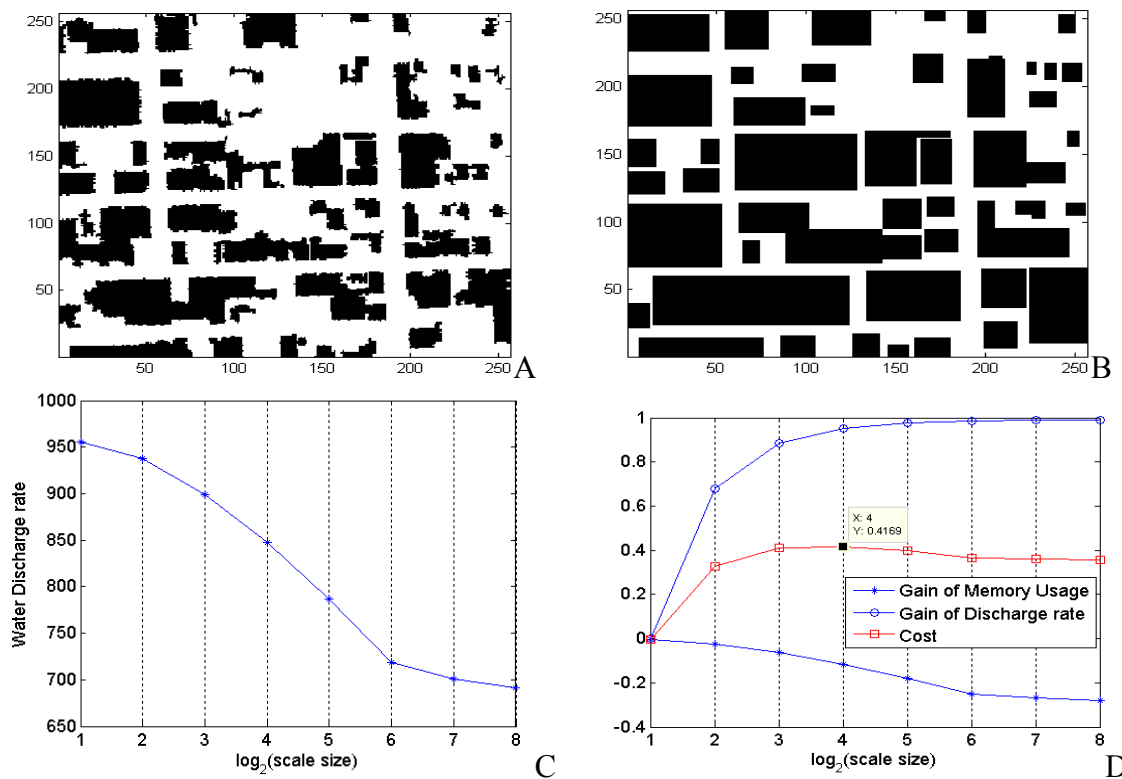


Figure 4-6. Optimal scale selection for buildings. A) the finest scale building footprint, B) the coarsest scale building footprint, C) the change of discharge rate by the quantization of building footprint with a wave moving from left to right, The x-axis is in units of the base-2 log of the pixel length in meters. In this particular scenario, the discharge rate decreases with scale because the widths of buildings are increased due to the quantization of building footprint. D) Optimal scale selection in terms of the gain of memory usage and discharge rate defined in Eq. 4-5. The cost function curve is then computed using Eq. 4-4. In this case, that occurs at $x=4$.

discharge rate. We chose our optimal scale to be 4 (16m) by choosing the appropriate balance between the error of discharge rate ($G_W(s)$) and memory usage ($G_M(s)$) using Eq.4-4 with $\lambda = 0.5$.

4.4 Evaluation

Once the ground data and building data have been individually reduced, we can recombine these two components to synthesize an approximation of the true hydrologic surface. The resulting elevation image is memory efficient while preserving most of the information that affects water flow over that terrain. The two types of synthesized DEMs are shown in Figure 4-7. The DN n images show the standard quadtree downsampling approach of MKS at different scales. The subscript n denotes the downsampling factor. The G x B y images are created using our reduction method. The subscripts x and y denote the downsampling factor on the ground data and

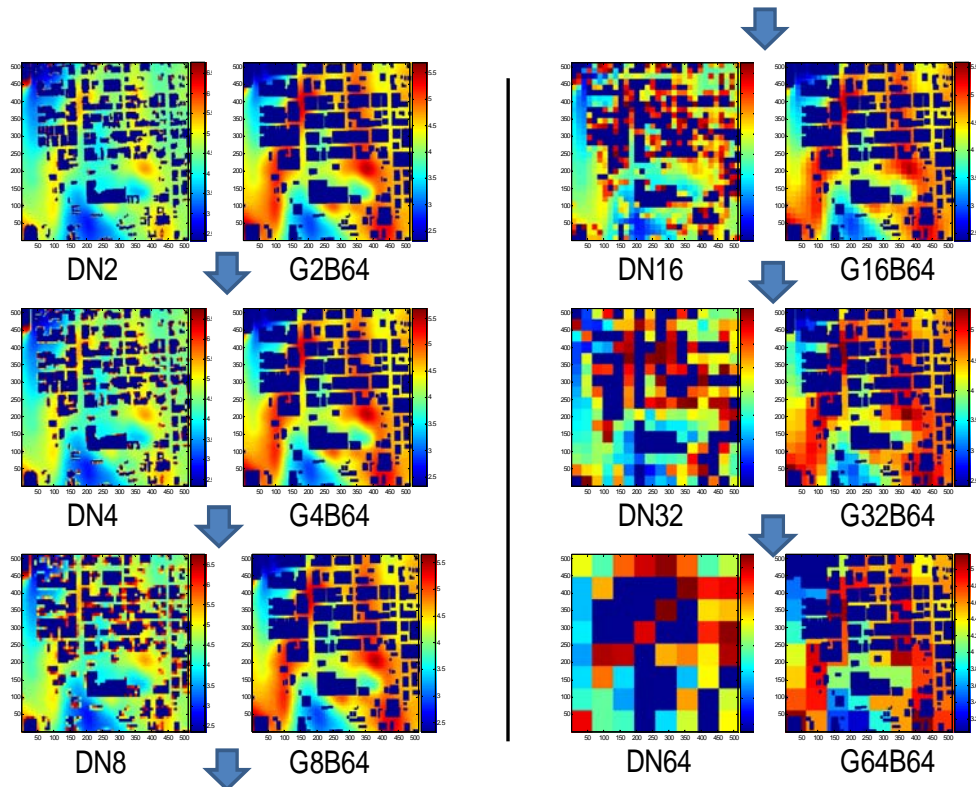


Figure 4-7. Two kinds of DEMs in different scales. DN n stands for downsampling by a factor of n , G x B y stands for x -scale for the ground and y -scale for the buildings. The arrow represents the change of scale going from fine to coarse.

the scale-division factor on the buildings, respectively. To quantify the performance of our method relative to the original quadtree-based downsampling of MKS (Slatton, Cheung *et al.*, 2005), we selected MSE (Mean Square Error) and the Correlation Coefficient (CC) as metrics to evaluate the hydrologic DEM as an elevation image. As hydrologic features, we chose flow accumulation number (FAN) generated by a hydrologic (flow routing) model and water discharge rate (WDR) generated by hydraulic (fluid dynamic) model.

4.4.1 Mean Square Error and Correlation Coefficient

The MSE and CC are general metrics commonly used to evaluate image quality. Mean square error is the simplest approach to measure error by the Euclidean distance between images and is defined (Bovik, 2005) as

$$MSE = E((I_T - I_D)^2) \quad (4-6)$$

where I_T is the true image and I_D is the test image (distorted by a reduction of information). A higher value of MSE obviously corresponds to greater distortion in the resultant image.

The correlation coefficient is a measure of the linear dependence of two random variables. For image data, this metric is used to depict the strength and direction (sign) of the relationship between the image pixels (Bovik, 2005). It is given by:

$$CC = E\left(\left(\frac{I_T - \mu_T}{\sigma_T}\right)\left(\frac{I_D - \mu_D}{\sigma_D}\right)\right) \quad (4-7)$$

where μ is the mean value and σ is the standard deviation. The subscripts T and D denote true image and distorted image respectively. The CC value can vary between -1 (perfect negative correlation) and 1 (perfect positive correlation). In our case, the images before and after reduction will have the same general relationships for positive and negative values. We therefore,

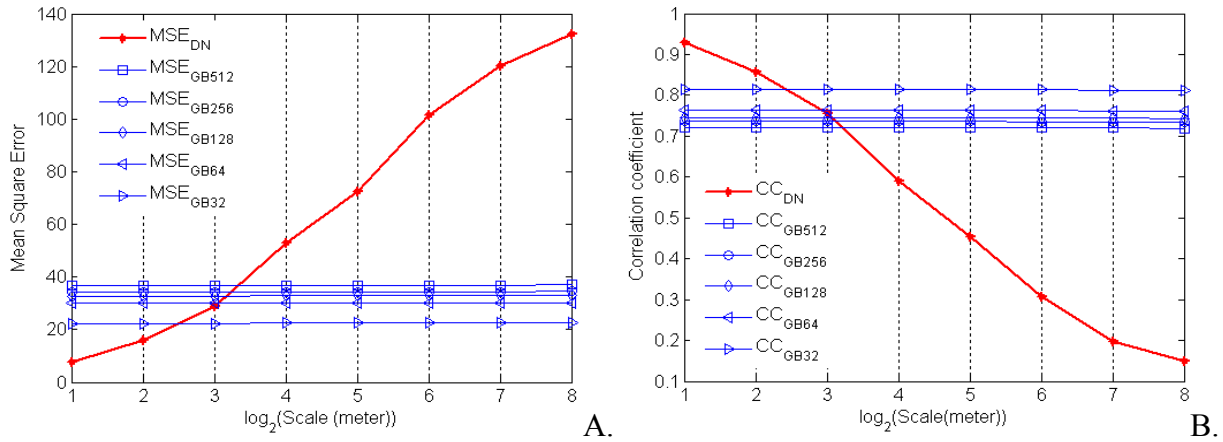


Figure 4-8. Evaluation of the hydrologic DEMs in Figure 4-7 as the scale is increased from 1m to 256m. The red curve is for naïve downsampling. The blue curves are for various GxBy configurations. A) Evaluation with MSE, B) Evaluation with CC. The results shows that downsampling reduction for ground data and saving two corner points for building data is very effective for preserving information without regard to scale.

need not worry about differentiating negative from positive correlation, and we can simply use the strength of correlation (the absolute value of the CC) as our accuracy metric.

Evaluation of the two reduction methods (downsampling and our proposed reduction method) based on MSE and CC values is presented in Figure 4-8. While the performance of downsampling continues to deteriorate as the size of the scale (pixel size) increases, our new approach is much less affected by scale changes because the vital information (e.g. building footprints) are preserved separately. The blue lines in Figure 4-8 represent the change of performance based on the scale of building reduction. Even though the performance decreases as a coarser scale is used to represent the building footprints, the error gap of our approach is small relative to that of the downsampling MKS method.

4.4.2 Flow Accumulation Number

Unlike the global MSE and CC metrics discussed above, FAN is evaluated at every pixel. It represents the total number of cells (pixels) that would contribute runoff water to the current considered cell from a gradient-based routing of flow from each cell to its steepest-decent

neighbor cell (ArcGIS, 2008). The flow routing algorithm allows us to resolve the spatial flow patterns of water (or sediment, nutrients etc) in a DEM. Thus we can determine the down slope areas (cells) in a landscape to which the outflow from a cell will be distributed (Desment *et al.*, 1996). To calculate FAN we used and modified the flow routing algorithm presented by Wolfgang, (2008). His code was implemented in MATLAB to enable users and developers to easily customize the algorithm and combine it with alternate applications, such as ecological cellular automata (Wolfgang, 2008). Since slope is a measure for the potential energy in a specific location, it is one of the most important influences on surface process. Wolfgang, (2008) defines the runoff slope from the considered pixel to each neighbor pixel as the downward angle between the pixels. It should be noted that other definitions for local DEM slope exist, such as area-based methods, and could be used. Another important question in both geomorphology and

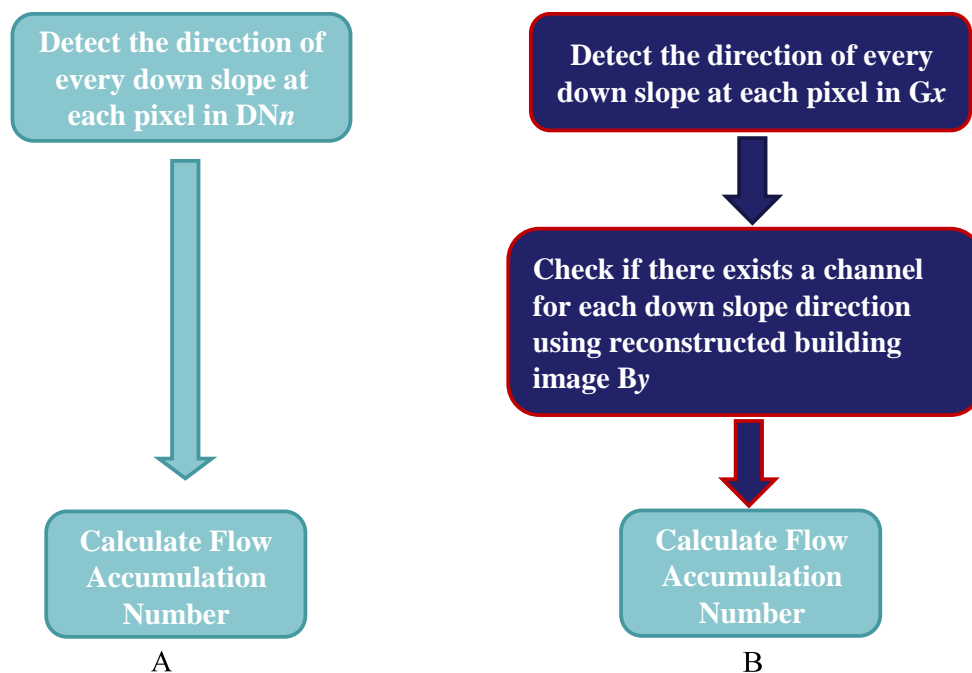


Figure 4-9. Procedure of calculating FAN. A) The standard procedure (D8 based multiple flow routing). B) the modified procedure for new data reduction.

hydrology is, “Where does the water flow when it rains?”. Wolfgang, (2008) chose the multiple flow direction algorithm, which partitions and transfers the discharge in each cell to all of its lower elevation neighbor cells (in the local 8-neighbor group) to overcome the weakness of the single flow direction algorithm. In general, single flow algorithms permit only parallel or convergent flows; however, multiple flow algorithms can accommodate divergent flow as well (Desmet *et al.*, 1996). The relative amount of discharge transferred from one cell to a maximum possible number of eight downward neighbors is proportional to the slope to each respective neighbor.

For the DN n images, the FAN was calculated by the standard procedure (Figure 4-9). However for the GxBy images generated using our reduction method, the standard procedure does not accurately reflect the preserved detail information of obstructions (e.g. buildings). We therefore modified the standard procedure for application to our reduction method as indicated in Figure 4-9. In order to evaluate the performance through the scales, we need to approximate the “ground truth” FAN data in each scale. The multiscale true FAN values were calculated by downsampling the FAN calculated from the finest scale DEM (Figure 4-10). Detection of high risk areas (DHRA) was then carried out by setting the average FAN as a binary threshold; areas

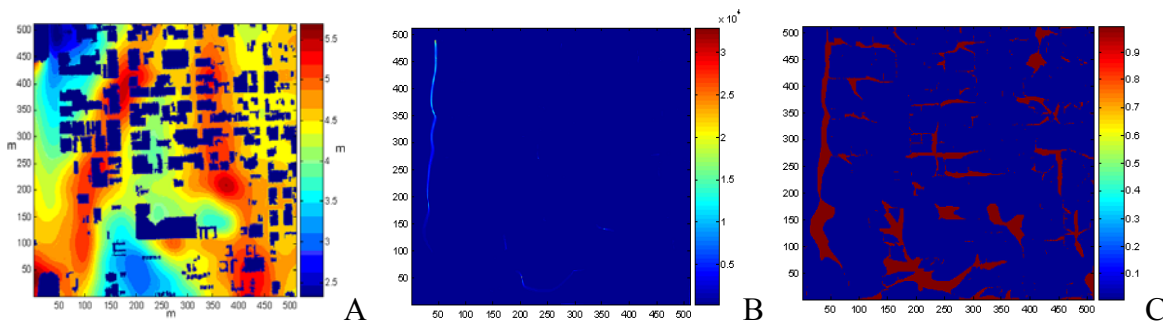


Figure 4-10. Input and resultant images for the FAN metric. A) A 1 m scale hydrologic DEM. Elevations are meters B) the corresponding FAN image. The colorbar units refer to the count of pixels that contribute runoff water to the each pixel in the DEM. C) Detected high risk areas by locating pixels with FAN values greater than the average value of FAN.

where the FAN was higher than the average were labeled as “high risk for flooding” with a value of 1 while the rest were set to a value of zero (Figure 4-10. C.).

We calculated the FAN values and DHRA in different scales using both the downsampling method and our method (Figure 4-11). Performance was then evaluated for coarse scale DHRA made from our proposed reduction method and from downsampling by calculating the strength of the CC with “ground truth” DHRA in different scale. The performance evaluation was plotted in Figure 4-12 in terms of different memory sizes and different building reduction scales. We see that, as expected, the correlation decreases as the memory size used in the downsampling MKS process is reduced. Applying our new data reduction method, we preserve a higher degree (more than 0.7) of correlation as the memory usage is decreased.

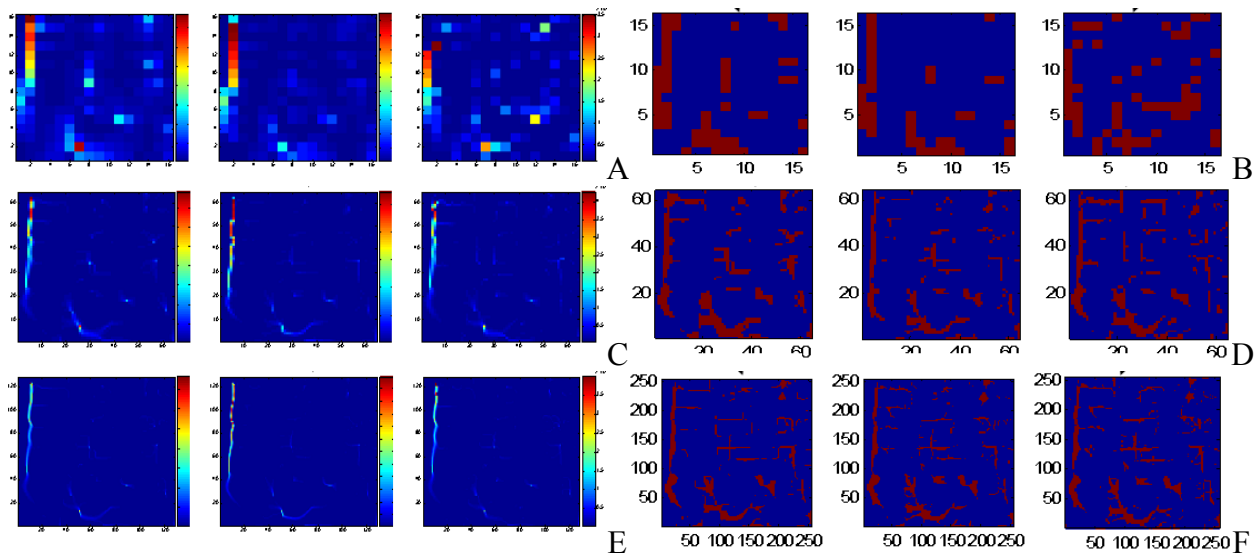


Figure 4-11. FAN and DHRA at different scales. For a given 1x3 row triplet, results from three methods are shown. In the left-most plot of each triplet, the result using our proposed method on the DEM to compute FAN or DHRA with the modified procedure is shown. In the right-most plot of each triplet, the result using naïve downsampling of the DEM and then computing FAN or DHRA with the standard procedure is shown. In the middle plot of each triplet, the approximation to “ground truth” is shown where the finest-scale FAN or DHRA result is itself downsampled to the corresponding scale. (A-triplet) FAN computed for scale = 32 m. (C-triplet) FAN computed for scale = 8 m. (E-triplet) FAN computed for scale = 2 m. (B-triplet) DHRA computed

for scale = 32 m. (D-triplet) DHRA computed for scale = 8 m. (F-triplet) DHRA computed for scale = 2 m.

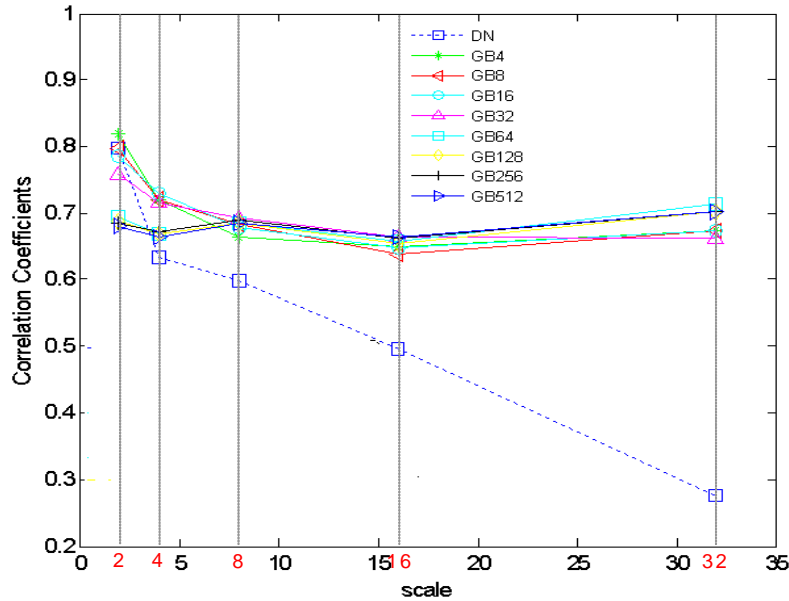


Figure 4-12. Comparison to high risk area detection (DHRA) by FAN. The dotted line with square mark shows the performance of downsampling. The other lines show the performance of our new reduction method at different scales of building descriptions. As scales approach those that are feasible for surge modelers (e.g. 16 m and larger), the proposed method preserves significantly more of the spatial structure of the DHRA, as evidenced by the CC values.

An interesting observation is that, in some cases, traditional downsampling actually performs better for a very limited range of scales close to the finest scale (e.g. resolution scales from 1m to 6 m). This is perhaps not surprising since the rectangularization of buildings can reduce more information than simple downsampling as one moves from meter-scale to the few-meter scales. For larger scales (more than 16 m), which are necessary for storm surge modeling, the proposed method maintains a much higher correlation with the original data. It should be noted that the building details seem to have an effect on the performance only in small scales. In large scales, the very fine details of buildings, (e.g. short channels between small buildings that are close together) do not have a significant effect.

The results from proposed reduction method appear to be very promising. By preserving the pertinent information like obstruction shape and location, we lost only 30% to 40% accuracy even after significant reduction in data volume. Interestingly, the advantage seen with regards to processing time was even larger than the reduced memory footprint. The memory reduction from 512x512 to 256x256 is 75 % while the corresponding decrease in processing time (34 seconds for 512 x 512 DEM, 3 seconds for 256x256 DEM) was 90% on a Dell 3Ghz, Intel Core2 Duo.

4.4.3 Water Discharge Rate

4.4.3.1 Simple 2D Hydraulic Model

In addition to the static hydrologic concept of FAN and the resulting metrics we explored above, we now wish to examine a dynamic hydraulic model and the resulting performance of our method. The full differential equation of a two-dimensional hydrodynamic modeling platform for shallow waters is known as the Shallow Water St. Venant complete equation (SWE) and can be found in (Covelli *et al.*, 2002). We ignored the convective acceleration and wind induced acceleration terms to arrive at a simple model. These modifications are appropriate since the former is a second order term that requires nonlinear solutions and the latter is an external forcing factor that is outside our scope.

The continuity equation is then given by:

$$\frac{\partial z}{\partial t} = -\frac{\partial q_x}{\partial x} - \frac{\partial q_y}{\partial y} \quad (4-8)$$

where t is time and (x, y, z) are the three Cartesian dimensions, with z referring to the vertical.

q_x and q_y denote the flux of water in the x and y directions along the local surface patch.

Likewise, the momentum equation can be expressed as:

$$\frac{\partial q_x}{\partial t} = -gh \frac{\partial z}{\partial x} - \frac{1}{\rho} \tau_{bx}, \quad (4-9)$$

$$\frac{\partial q_y}{\partial t} = -gh \frac{\partial z}{\partial y} - \frac{1}{\rho} \tau_{by}$$

where g is the local gravitational acceleration, h is the water depth., τ_{bx} and τ_{by} are the shear stress components in x and y direction, and ρ is the water density.

It is common to solve these equations with computer aided numerical methods after approximating them into finite difference equations (FDE) since they do not typically have analytical solutions for general geometries. The appropriate FDEs, of first order accuracy, are given as follows:

FDE continuity equation:

$$z_{(i,j)}^{t+\Delta t} = z_{(i,j)}^t + \frac{\Delta t}{\Delta x} (q_{x(i+\Delta x,j)}^t - q_{x(i,j)}^t) + \frac{\Delta t}{\Delta y} (q_{y(i,j+\Delta y)}^t - q_{y(i,j)}^t) \quad (4-10)$$

FDE momentum equations:

$$q_{x(i,j)}^{t+\Delta t} = \frac{q_{x(i,j)}^t - g\bar{h}_{x(i,j)} \frac{\Delta t}{\Delta x} (z_{(i+\Delta x,j)}^t - z_{(i,j)}^t)}{\left(1 + \frac{f_{x(i,j)} |\bar{q}_{(i,j)}^t| \Delta t}{8\bar{h}_{x(i,j)}^2}\right)} \quad (4-11)$$

$$q_{y(i,j)}^{t+\Delta t} = \frac{q_{y(i,j)}^t - g\bar{h}_{y(i,j)} \frac{\Delta t}{\Delta y} (z_{(i,j+\Delta y)}^t - z_{(i,j)}^t)}{\left(1 + \frac{f_{y(i,j)} |\bar{q}_{(i,j)}^t| \Delta t}{8\bar{h}_{y(i,j)}^2}\right)} \quad (4-12)$$

where Δx (Δy) is the distance (in meters) between two pixels (i.e. the horizontal/vertical resolution of the image); $q_{x(i,j)}$ ($q_{y(i,j)}$) is water discharge rate (m^3/s) into location (i,j) in the x (y) direction; $\bar{h}_{x(i,j)}$ ($\bar{h}_{y(i,j)}$) is the averaged water depth (m) between (i,j) and $(i-\Delta x,j)$ in the x (y) direction, such that $\bar{h}_{x(i,j)} = (h_{(i-\Delta x,j)} + h_{(i,j)})/2$ ($\bar{h}_{y(i,j)} = (h_{(i,j-\Delta y)} + h_{(i,j)})/2$); and $f_{x(i,j)}$ ($f_{y(i,j)}$) is the friction coefficient (dimensionless) of the channel between the (i,j) and $(i-\Delta x,j)$ in the x (y) direction.

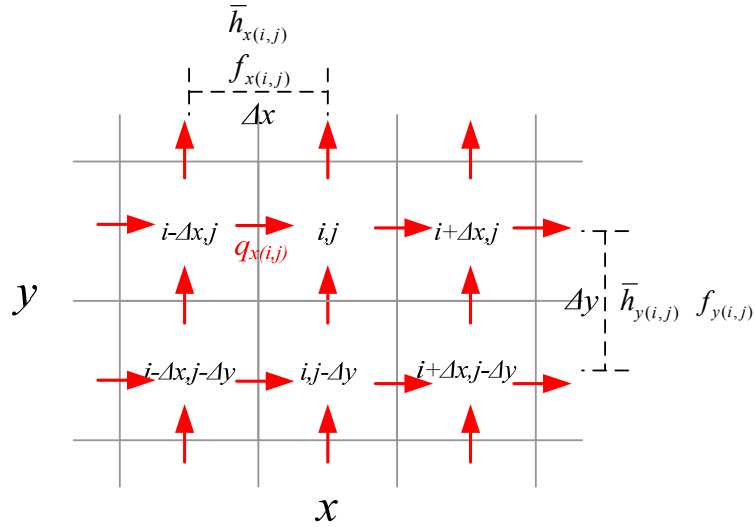


Figure 4-13. Spatial domain discretization scheme

Figure 4-13 shows the numerical approximation at spatial domain having first order accuracy for least computational complexity.

For the finite difference to have a unique solution we must define boundary conditions and initial values. For boundary conditions, arbitrary different water heights were set to ensure some flow from the left to right edges in the DEM. We prescribed no flow boundary conditions at the upper and lower boundaries in the DEM to prevent more complex water flows in and out of the DEM. The initial value of the water surface height ($z_{(i,j)}$) was defined by the boundary conditions. While initial values of discharge rates ($q_{x(i,j)}$, $q_{y(i,j)}$) are generally set to zero, we used an approximate solution of the Darcy Weisbach equation (Chow *et al.*, 1988) as the initial values to achieve faster convergence. We then used the Courant-Friedrichs and Lewy condition (Covelli *et al.*, 2002)

$$\Delta t < \frac{\min\{\Delta x, \Delta y\}}{\sqrt{2gh_{\min}}} \quad (4-13)$$

imposed on the time step to maintain numerical stability and help to ensure convergence.

In order to verify our new model under the conditions mentioned above we have to check if the final solution can reach a steady state. Since a steady state implies no change in water surface height regardless of the lapse of time, we can set the continuity equation to zero as shown below.

$$\frac{dq_{x(i,j)}}{dx} + \frac{dq_{y(i,j)}}{dy} = -\frac{dz_{(i,j)}}{dt} = 0 \quad (4-14)$$

We define the criteria to stop the iterative calculation procedure

$$\sum_{j=1}^J \left(\frac{dq_{x(i,j)}}{dx} + \frac{dq_{y(i,j)}}{dy} \right) \Delta y = 0 \quad (4-15)$$

$$\frac{d}{dx} \sum_{j=1}^J (dq_{x(i,j)} \Delta y) + \frac{d}{dy} \sum_{j=1}^J (dq_{y(i,j)} \Delta y) = 0 \quad (4-16)$$

$$\frac{d}{dx} Q_{x(i)} + Q_{y(i,J)} - Q_{y(i,1)} = 0 \quad (4-17)$$

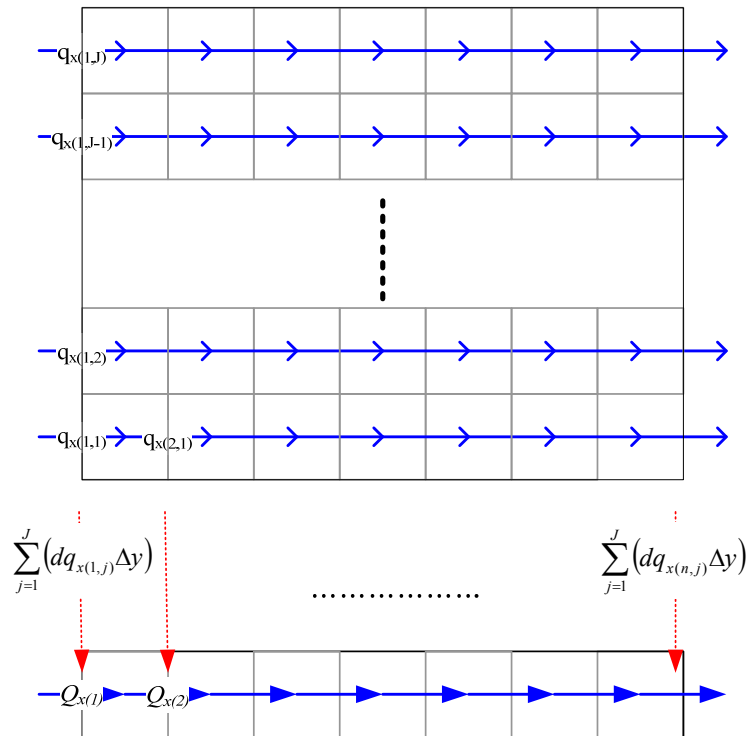


Figure 4-14. Pictorial illustration of the criterion ($Q_{x(1)} = Q_{x(1)} = \dots = Q_{x(n)}$)

and we provide the pictorial illustration in Figure 4-14.

The criterion to stop the procedure is globally

$$Q_{x(i)} = Q_{x(i+\Delta x)} \text{ for all } i \quad (4-18)$$

In practice excessive processing time is required to strictly satisfy the steady-state criterion. We therefore apply a less strict stopping criterion as follows

$$\max_i(Q_{x(i)}) - \min_i(Q_{x(i)}) < 10^{-5} \quad (4-19)$$

Even with the above criterion, we checked the results for several simulations. In some cases, the solutions did not reach steady-state. Since our simple model does not consider every physical force related to topographical features and is only a first order approximation, we could observe the occasional divergence of the solution in cases where some excessive in-flow or out-flow existed initially. This creates an unstable localized state that eventually spreads through all other locations. This was the cause of the observed divergence of the total solution. To prevent the divergence we initially set the friction coefficients, $f(0)$, as an arbitrarily high value f_0 and decreased it exponentially. The minimum value should not be lower than the real value we want to use, so we expressed the friction coefficient as follows.

$$f(n) = f_t + f_0 e^{-an} \quad (4-20)$$

where n is the iteration number, f_0 is the initial value much bigger than f_t , a is the rate of decreasing f_0 . a was chosen experimentally since the iteration can potentially be stopped by the steady-state criterion before $f(n)$ can reach f_t for very small values of a . On the other hand, the divergence can occur if a is chosen too large. To choose a proper value for a , we decreased a gradually whenever we observed divergence. Figure 4-15 shows that our method to prevent the numerical solution diverging on the surface having obstructions is effective.

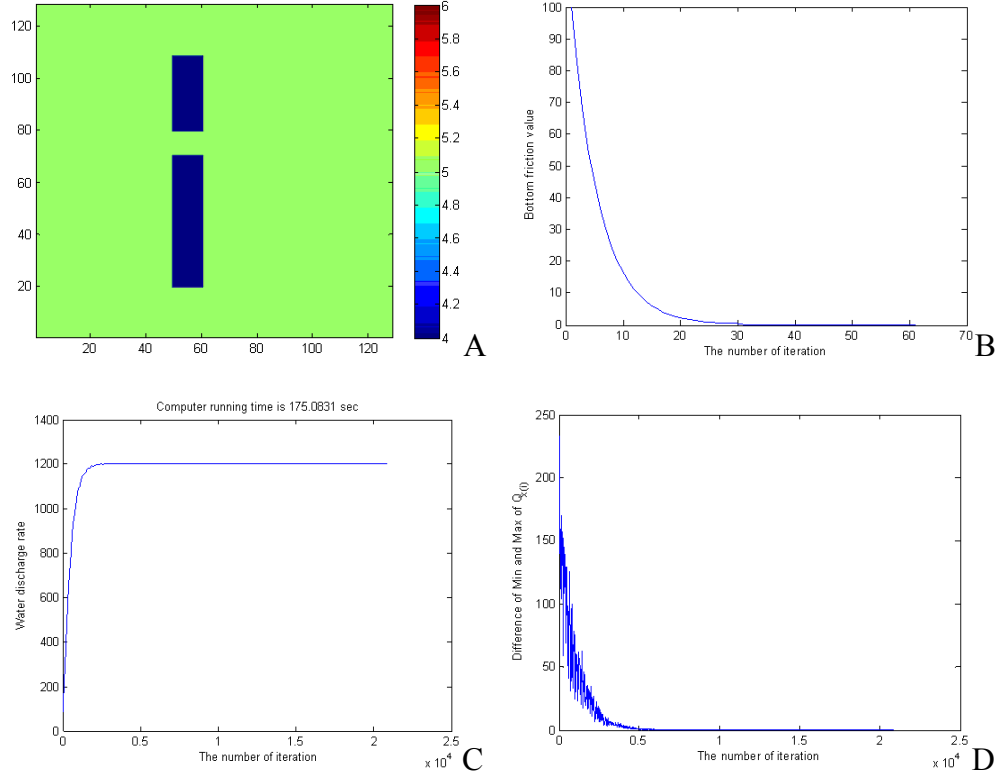


Figure 4-15. Convergence of our simple model with changing bottom friction value. A) DEM, B), friction value $f(n)$, C) averaged water discharge rate, D) difference between min and max of $Q_{x(i)}$

After we had established that our solution reached steady-state, we want to test the accuracy of said solution. First, the simple model was evaluated by comparing the numerical solution to an analytical solution for a hypothetical flat bottom since the analytical solution is only applicable to the flat bottom case. Analytical solutions can be calculated from the equation of water head loss (Chow *et al.*, 1988) rewritten in terms of the discharge rate per unit width as follows

$$\frac{dh}{dx} = -\frac{f}{4} \frac{q^2}{2gh^3} \rightarrow q = \sqrt{\frac{2g(h_1^4 - h_2^4)}{f\Delta x}} \quad (4-21)$$

where h_2 , $h_1(x_2, x_1)$ are the boundary conditions at the left edge and right edge respectively

Since the analytical solution can be derived from numerical equations with the condition of

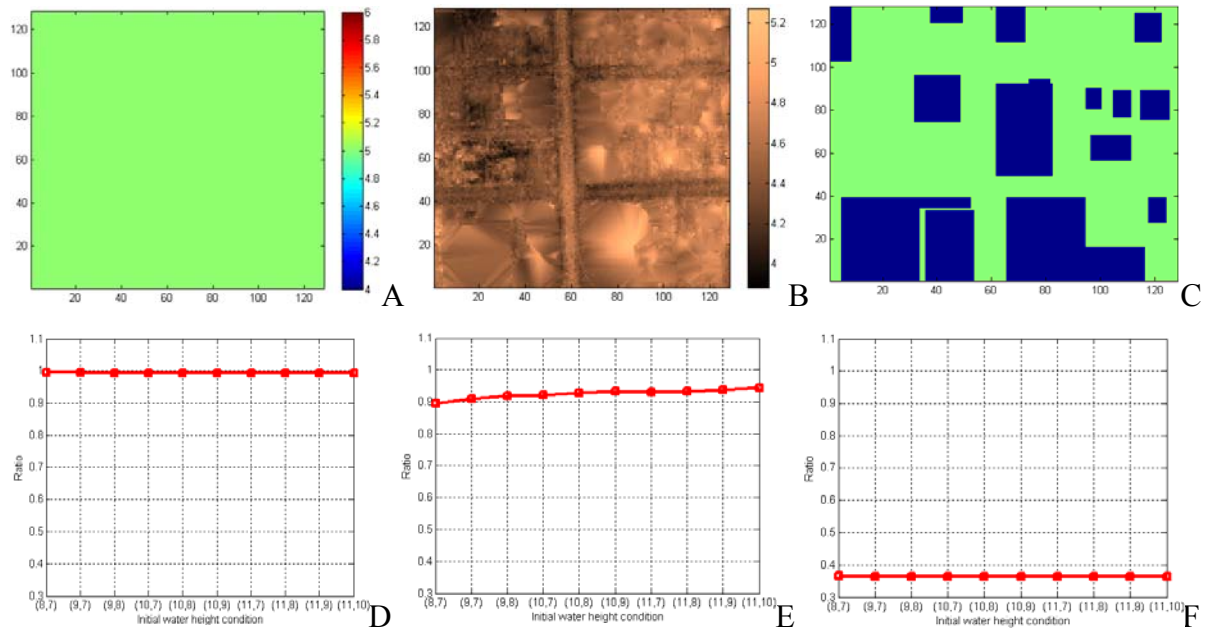


Figure 4-16. Testing of the ratio of the numerical solution to an analytical solution. A,D) the ratio for a hypothetical flat bottom DEM. , B,E) the ratio for real bare ground data. C,F) the ratio for flat surface with buildings data. The abscissas (h_1 , h_2) of D, E, F) represent of initial water depth at left and right boundary, respectively. .The ratio of C is low because the impact of buildings is significant

flat surface the numerical solution should be same to the analytical solution without regard to water depth. With the assumption that the multiple water depths (h_1 and h_2) are given at the left edge and right edge, the width (Δx) of the DEM is 256 meters, and the bottom friction factor is 0.05, the ratio (q_n) of the numerical solution to the analytical solution is shown in Figure 4-16 . The results in Figure 4-16 A and D show that our simple model is valid since the numerical solution exactly agrees with the analytical solution for the case of a perfectly flat bottom with no obstructions.

Figure 4-16 B and E depict results from this simple model applied to real ground data in the Miami area. Results show a very small (9%) difference between the numerical solution for real ground data and the analytical solution for the assumed flat surface since the real DEM data is nearly flat. In other words, in this case the effect of the actual ground data is very small, such that one can use the analytical solution for the ground instead of numerical solution.

The comparison of the numerical solution being applied to a flat surface with buildings and the analytical solution is low, with an accuracy of less than 40% (Figure 4-16, C, F) because the impact of buildings is not reflected in the analytical solution. Therefore we must somehow compensate for the impact of buildings when we make urban areas coarse. This is perhaps not surprising since buildings will tend to lose their perceived surface area as we decrease the resolution of the DEMs. The following section shows how we compensate for this phenomenon.

4.4.3.2 Sub-grid Parameterization

Since there is no physical model of fluid flow which considers buildings, we must create a method to compensate for the effect of these structures. Based on the underlying physical behavior, we derived new friction values in consultation with Prof. Bob Dean of the University of Florida that are equivalent to the shear stress on the ground. To derive the equivalent friction factor, first we define the drag force due to the building as follows

$$F_D = \frac{C_D \rho W V^2 h}{2} \quad (4-22)$$

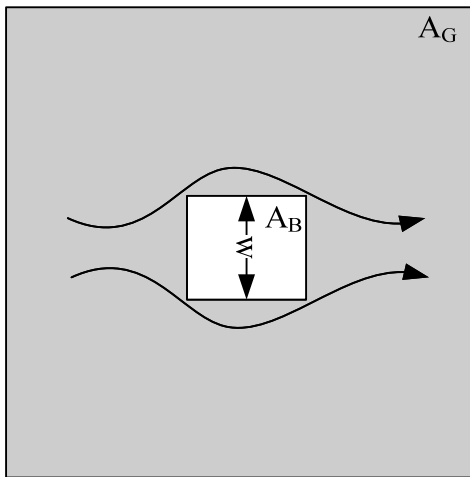


Figure 4-17. Example of the physical behavior of water by building. w is the width of building that is perpendicular to water direction. A_G is the area of ground, A_B is the area of building. A_T is the total area ($A_B + A_G$)

where W is the projected width of the buildings relative to the flow vector (m) (i.e. this quantity will change with flow direction), C_D is the drag coefficient (dimensionless, around 1.0), V is the water speed in the direction of flow (in m/s), h is the water depth and ρ is the water density.

Since the shear stress is force per unit area, the equivalent shear stress considering a building is the sum of the drag force induced by the building and the shear stress induced by the ground (Figure 4-17).

$$\begin{aligned}
 \tau_{eq} &= \frac{F_T}{A_T} = \frac{F_D + \frac{\rho f V^2}{8} A_G}{A_B + A_G} \\
 &= \frac{\frac{C_D \rho W V^2 h}{2} + \frac{\rho f V^2}{8} A_G}{A_B + A_G} \\
 &= \rho \left[\frac{4C_D \rho W V^2 h + f A_G}{A_B + A_G} \right] \frac{V^2}{8}
 \end{aligned} \tag{4-23}$$

where A_G is the area of ground, A_B is the area of building, A_T is the total area of building and ground, f is the friction factor by ground, F_D is the drag force by building, and F_T is the total drag force by ground and building,

The bottom stress used in general fluid models is $\tau = \rho f V^2 / 8$ so that the friction factor when considering multiple buildings is

$$f_M = \frac{4C_d h \sum_n W_n + f \left(A_T - \sum_n A_{Bn} \right)}{A_T} \tag{4-24}$$

where n is the number of buildings. Note that it is dependent on flow depth h as well as width and area of buildings

From the equivalent friction equation we see that the vital features are the widths and sizes of buildings. The features can be directly extracted from the encoded building data depending on

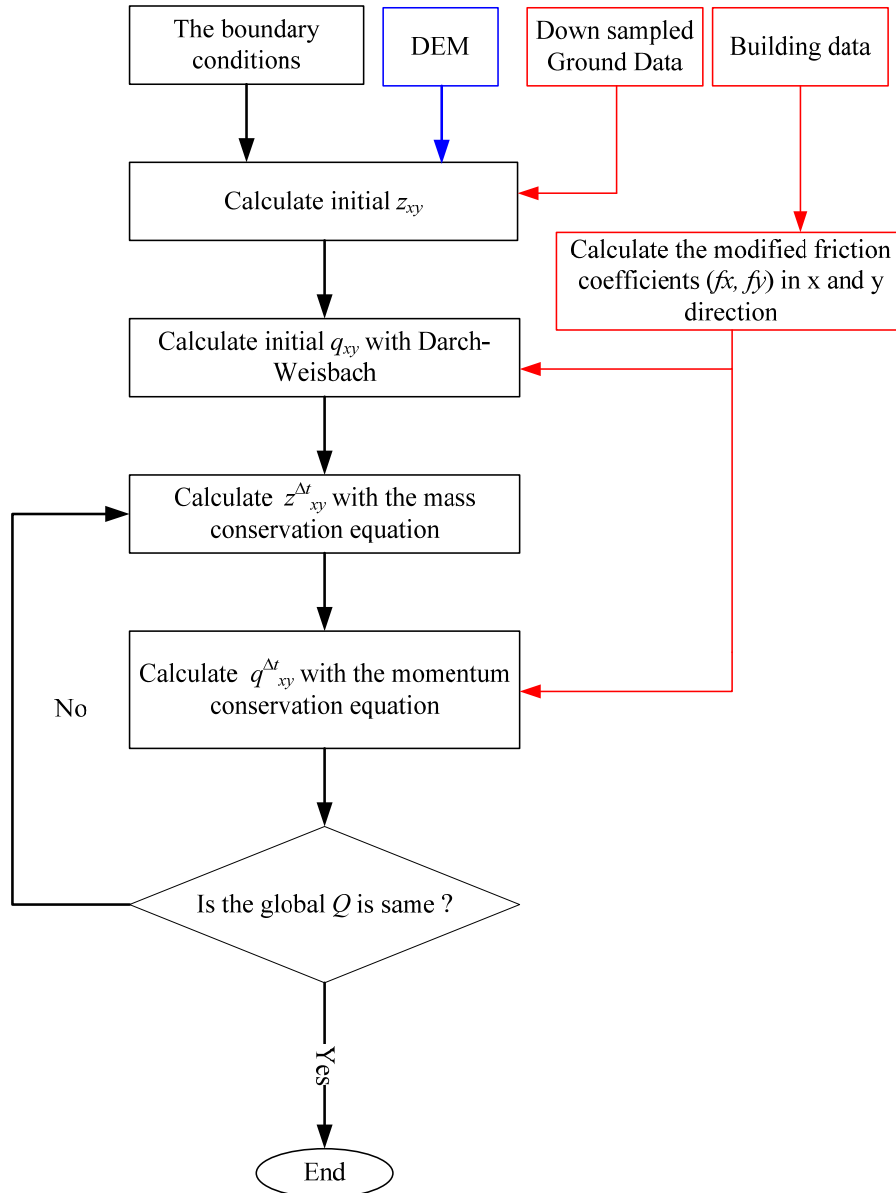


Figure 4-18. Procedure for calculating WDR. The additional red procedure is for the new reduction approach.

the scale of the data. The procedure to calculate fluid discharge rate is shown in Figure 4-18. The steps outlined in the red box are done to use the decomposed data separately and parameterize buildings in a sub-grid size.

4.4.3.3 Evaluation

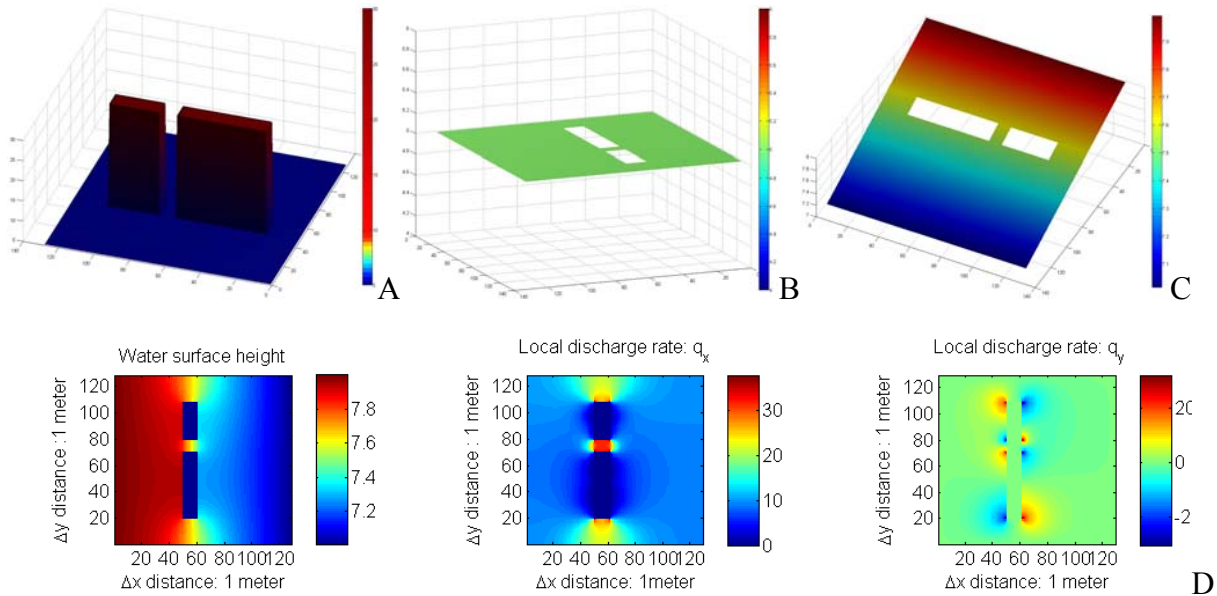


Figure 4-19. Simple simulated DEM and its estimated WDR. A) Simulated DEM in the finest (1 meter) scale, B) input DEM after voiding buildings , C) initial input water surface by boundary condition (First of D) water surface height, $z_{(i,j)}$, (Second of D) local charge rate in x direction, $q_{x(i,j)}$, (Third of D) local discharge rate in y direction, $q_{y(i,j)}$.

In order to evaluate the performance of our approach we compare results with those from naive downsampling. First we calculated the change of local discharge rates, $q_{x(i,j)}$, $q_{y(i,j)}$ and global discharge rate, $Q_{x(i)}$ using a simple but plausible DEM simulation (Figure 4-19). The simulation DEM clearly shows the effect of downsampling locally and globally as we increase the scale size. The water surface height and local discharge rates in x and y directions are provided in Figure 4-19.

The same results for the downsampled DEM and the decomposed and parameterized DEM (our method) are shown in Figures 4-20 and 4-21, respectively. While two buildings become merged in the downsampling method at the 8 meter resolution, our approach preserved the impact of separate buildings in the discharge . As a result, the discharge between the two

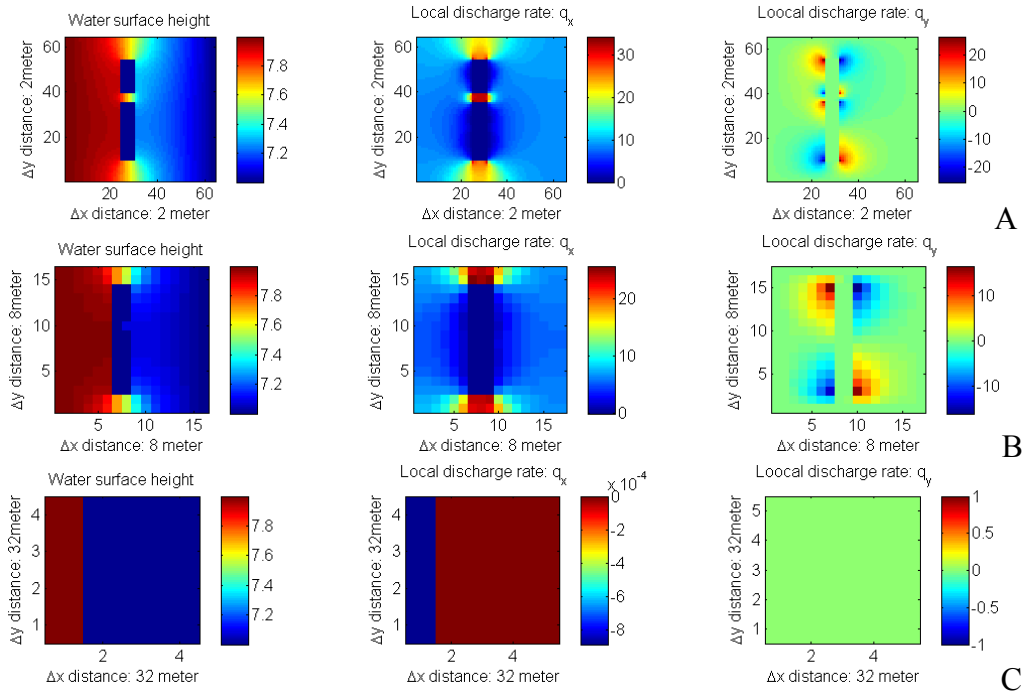


Figure 4-20. Estimated WDR of hydrologic DEM made by downsampling. (left) water surface height, (center) local charge rate ($q_{x(i,j)}$) in x direction, (right) local discharge rate ($q_{y(i,j)}$) in y direction of DEM made by naive down sampling. A) 2 meter resolution DEM, B) 8meter resolution DEM C) 32 meter resolution DEM

buildings disappears in the downsampling method while it remains in our approach (compare second rows in Figures 4-20 and 4-21). The performance difference between downsampling and our reduction at 32 m resolution is very significant ($0 \text{ m}^3/\text{s}$ for downsampling, $1150 \text{ m}^3/\text{s}$ for our reduction, whereas the true rate is $1200 \text{ m}^3/\text{s}$). While the discharge rate is calculated as zero due to total blockage in the downsampling case, our approach makes a good estimation of the discharge rate (compare third rows in Figures 4-20 and 4-21). The result shows that, at the same scale, the local detail information is preserved in our reduced image and discarded in the naively downsampled image.

Figure 4-22 demonstrates that the decomposed/parameterized approach also makes an accurate estimate with regards to global information. Figure 4-22 also shows the difference in running time between our method and the downsampling approach. You can find small

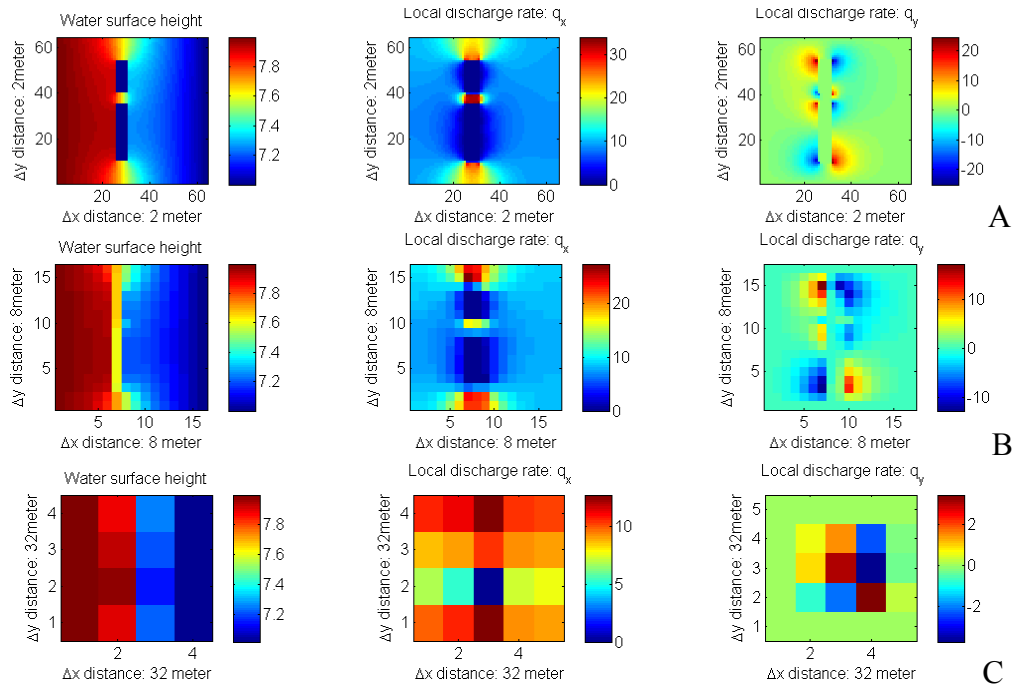


Figure 4-21. Estimated WDR of hydrologic DEM and sub-grid parameterization made by our reduction method. (left) water surface height, (center) local charge rate ($q_{x(i,j)}$) in x direction, (right) local discharge rate ($q_{y(i,j)}$) in y direction of DEM made by our approach. A) 2 meter resolution DEM, B) 8meter resolution DEM C) 32 meter resolution DEM. At 8 m resolution the local discharges between buildings can be seen while the local discharges in Figure 4-20 disappear by merging two buildings due to downsampling reduction. At 32 m resolution we can see the existence of the discharge while the discharge rate is $0 \text{ m}^3 / \text{s}$ in Figure 4-20 by a complete blockage due to downsampling.

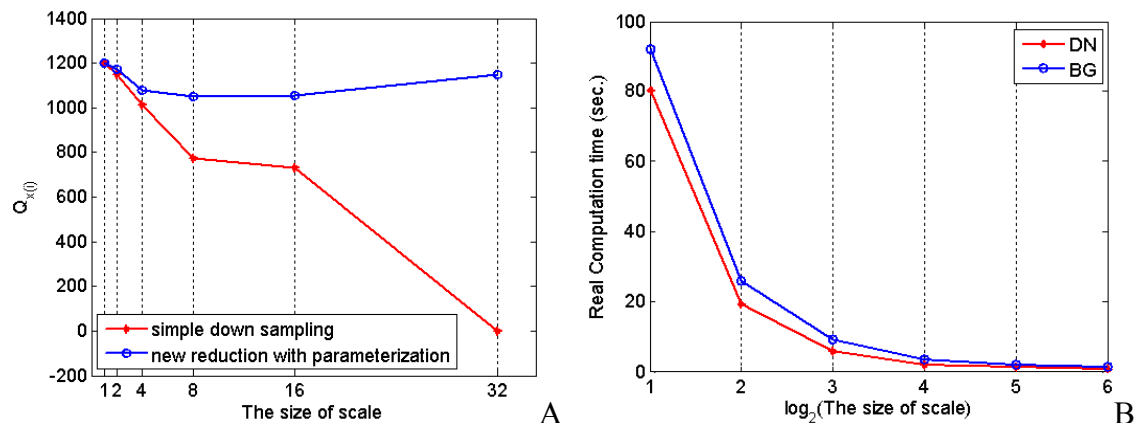


Figure 4-22. Comparison of total discharge rate and running-time between downsampling method and our reduction method at different scale. A) The $Q_{x(i)}$ comparison between naive downsampling and new method. The vertical axis is discharge in the x direction $Q_{x(i)}$ B) The real computation time to calculate water discharge rate in different scale and different method (red is for downsampling, blue is our new method)

differences between the two methods in each scale because our method has an additional procedure to encode the impact of buildings. However, the additional time required is small.

We then repeated this process, comparing results for the real Miami DEM (Figure 4-23). Figure 4-23 shows the performance comparison in terms of coarsening the building parameterization and the scale of ground for real data (Miami, FL). The notation ‘B*G’ is used to represent the scale of building footprints, where ‘*’ is the corresponding scale/resolution in meters. Using fine scale ground data, the results deteriorate depending on the degree of coarsening of the building details. With the coarse scale ground data, the difference in performance is much less. In other words, similar performance can be obtained while saving memory usage for building information when the surge modeler wants to use a very coarse resolution hydrologic DEM to save computation time.

Comparing the results from our algorithm with those of downsampling over the real Miami data, the error trend is almost equivalent to the error trend observed for the simulation. As the scale of downsampling is increased, the water discharge rate decreases due to merging of closely

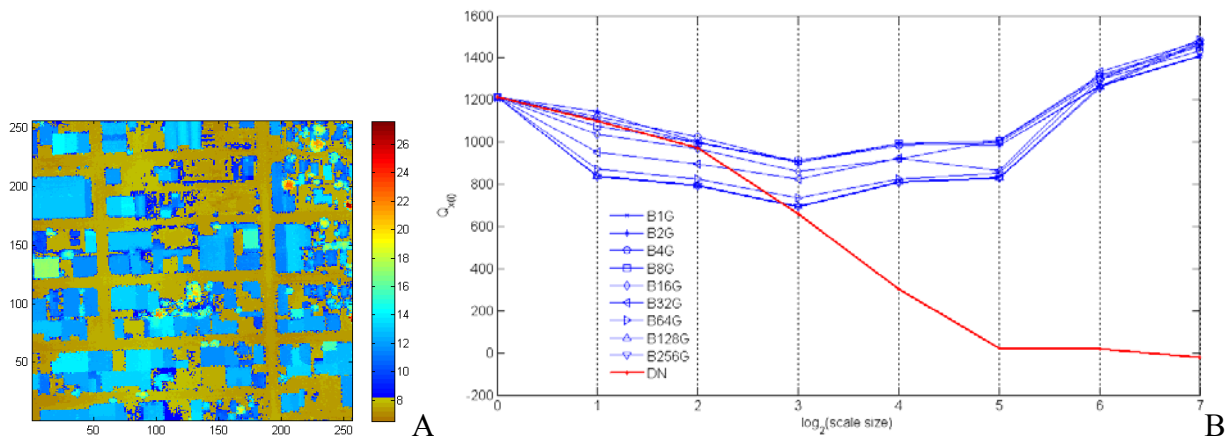


Figure 4-23. Comparison of total discharge rate over real DEM data at different scales with different levels of building rectangularization. A) Real Miami DEM, B) The comparison between naive downsampling and new method with the real data. We desire for the discharge to change as little as possible as scale is increased. We see that the proposed method allows us to maintain reasonable estimates of discharge across a large range of scales, whereas the downsampling does not.

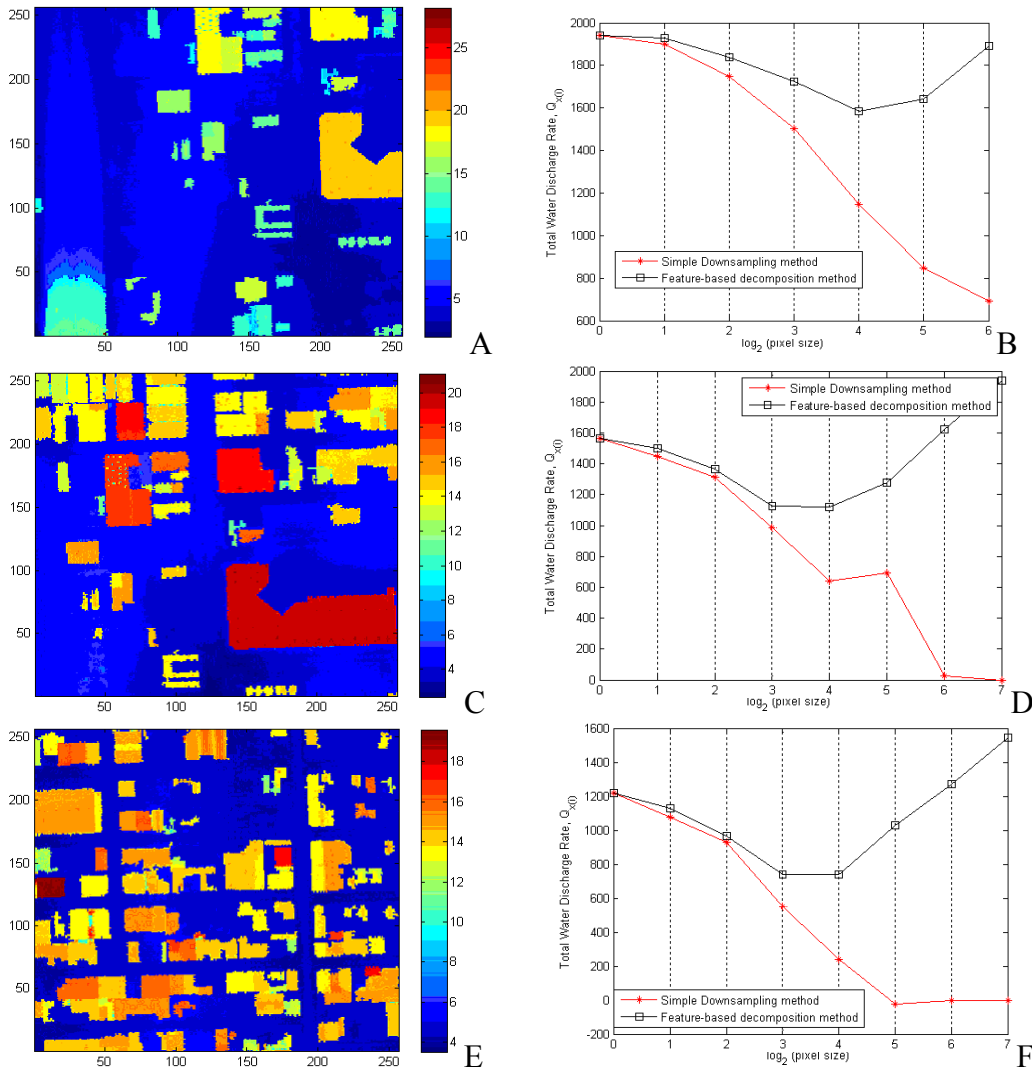


Figure 4-24. Estimate of total discharge rate on different sites in Dade County, Miami, FL. A, C, E) Different sites B, D, F) Corresponding estimate of total discharge rate. Those show the aberrant behavior common to the estimate of $Q_{x(i)}$.

spaced adjacent buildings. For small downsampling factors, the effect of the reduction is not noticeable and the performance of downsampling is generally acceptable. However, as the scale of downsampling is increased, the effects get worse and the advantages of our method become obvious.

When we applied our reduction method on different sites we observed a strange behavior common to the estimate of $Q_{x(i)}$. The estimate was observed to rise suddenly after a steady decrease as a function of pixel size.

In order to find the cause, we applied our reduction method on simulated DEMs with different building distributions (Figure 4-25). As a result, we determined that the reason for the aberrant behavior in the performance curve was the new friction value (Eq. 4-24) that accounts for the impact of buildings. The new friction value is decided by the sum of forces of buildings

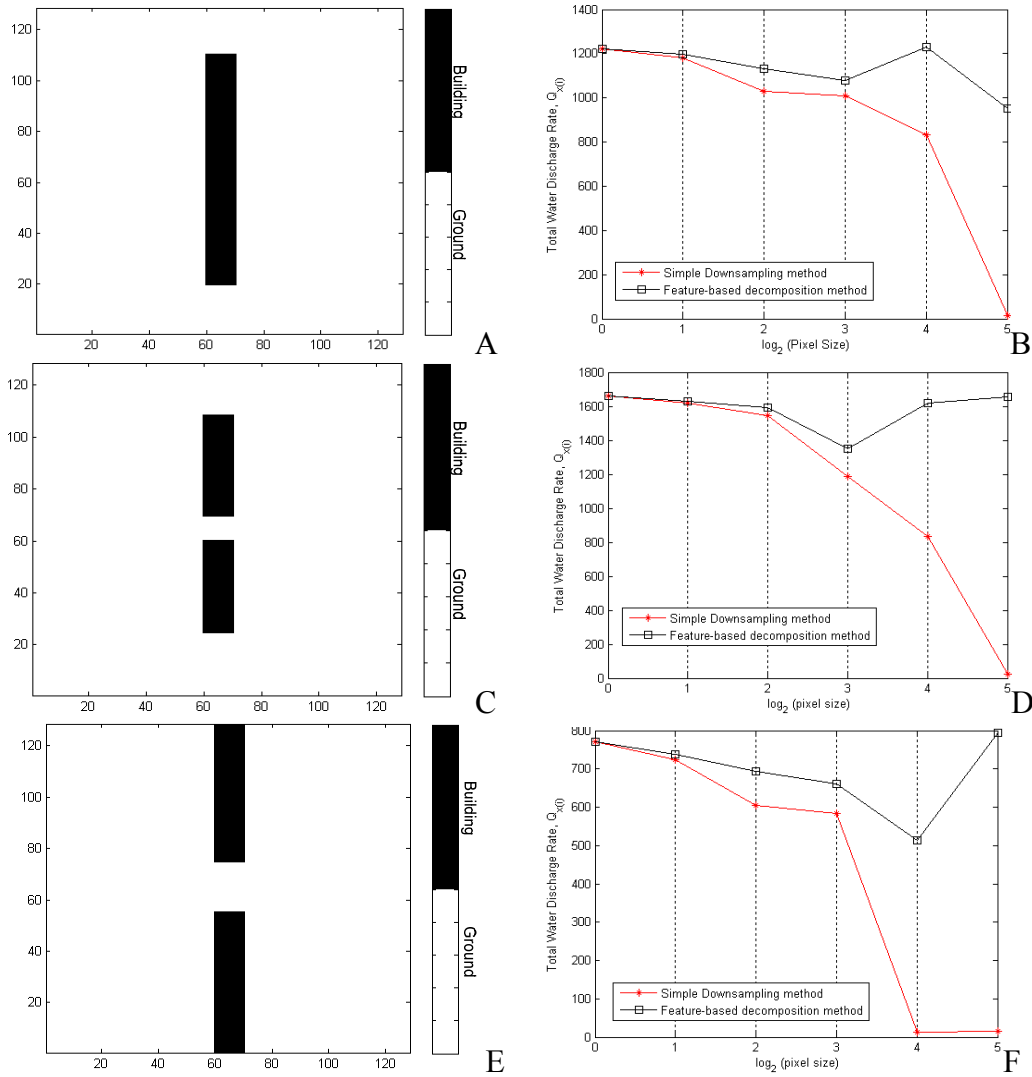


Figure 4-25. Estimate of total discharge rate on simulated DEMs having different building distribution, A, C, E) Simulated DEMs having different building distribution, B, D, F) Corresponding estimate of total discharge rate. After two buildings being merged by downsampling it cannot generate the total discharge rate. Our reduction method can still make the total discharge rate. As the scale of the ground pixels increases, any given ground pixel will likely be a composite of multiple buildings, so that our friction value systematically under-estimates the actual combined impact.

and the shear stress of ground. In this process, we did not consider the effect of the distribution of buildings because the impact was generally thought to not be significant. In other words, the new friction value cannot perfectly account for the impact of multiple buildings. At small scales, individual buildings reside inside a single ground pixel, and the friction value properly predicts the impact of the building structure. As the scale of the ground pixels increases, any given ground pixel will likely be a composite of multiple buildings, so that our friction value systematically under-estimates the actual combined impact. As future work, we plan to research a method that accurately parameterizes the impact of multiple buildings independent of scale.

CHAPTER 5 CONCLUSIONS AND FUTURE WORK

The fusion of diverse multi-sensor observations allows us to identify appropriate surface models and scaling relationships for topographic and bathymetric surface features in the coastal zone. However, in order to run hydrologic process models capable of predicting such things as hurricane storm surge, evacuation routes, flood risk, coastal wave spectra, and littoral-zone erosion, improved seamless elevation maps must be obtained that cover the land surface and the underwater surface. In our work we used four types of elevation data sets: 90 m resolution NGDC data, 30 m resolution SRTM, 10 m resolution bathymetric LiDAR, and 1-5 m resolution topographic LiDAR. The topography and bathymetry in the NGDC were derived from stereo aerial photography and sonar sensors, respectively. The SRTM was acquired from the space shuttle with dual-antenna C-band SAR. The high resolution topography and bathymetry data derived from the LiDAR were acquired by airborne lasers using different wavelengths (532 nm for bathymetry, 1064 nm for topography) and flight altitudes (300~400 m for bathymetry, 900~1200m for topography).

In section 3.2, we investigated a computationally-demanding application of MKS data fusion. When the data sets to be fused differ in resolution by an order of magnitude or more and the fine-scale observations are sparse and aggregated, the standard MKS algorithm proves inefficient. We reduced the floating point operations per node by two by deriving a new equation for calculating the covariance of the process noise (the detail process). The equation has a general form so that we can reduce the operations per node without regard to the distribution of the data in the quadtree. We also then reduced the number of nodes in the quadtree that must be processed depending on the distribution of the finest-scale data, which led to a dramatic

reduction (more than 80% for our data sets) in floating point operations required for estimating a fused DEM from the component data.

In section 3.3, the accuracy of the SRTM DTED-2 data was evaluated by analyzing the statistical characteristics of the Kalman innovations (the difference between measurements and projected prior estimates) in the MKS estimator to estimate a terrain-dependent measurement uncertainty for the SRTM data. Fused DEMs can be produced at every scale, such that the benefits of global coverage and finer details are present. Fused DEMs can provide improved boundary conditions for predicting areas affected by floodwaters as compared to a DEM at any single scale (See Figure 3-11). The uncertainty associated with each elevation estimate (the Kalman estimate error variance) was also obtained at every pixel, thus the fused DEMs at each scale are accompanied by a confidence map at each scale. The SRTM data were found to provide important intermediate-scale information for bridging the gap between large national elevation data sets like the NGDC and small high-resolution elevation data sets like the LiDAR. In future work, refined methods for estimating terrain-dependent SRTM uncertainty for more specific land-use classes will be investigated.

In principle, the high spatial resolution of airborne LiDAR observations makes it possible to use relatively simple hydraulic models to accurately model the flow of water across open terrain in rural areas and in highly developed urban areas. Modelers can also take advantage of high spatial resolution LiDAR data to compare the relative advantage of incorporating more complex hydraulic models with higher order terms. However, because natural disasters tend to impact relatively large areas, we are also interested in analysis of areas of much larger scale. For example, the effective range of Hurricane Katrina was about 200~300 km (Resio *et al.*, 2008). Running meter scale simulations over areas of hundreds of square kilometers results in

unacceptable computation times, even with the simplest hydraulic models, making it necessary to reduce the spatial resolution of the observational data.

Historically, reduction of image data, such as in JPEG and MPEG encoding, was done by transforming the data into a different domain (from spatial to frequency or from spatial to wavelet) and bit encoding (run-length coding) to reduce redundancy. However, this process of transforming and encoding data can transmute inherent properties of the data in the original domain (e.g., elevation, area and width of buildings). As a result, the reduced data must be decoded and transformed back to the original domain to retrieve the desired features.

The main advantage of the method proposed herein is that the reduced data does not require any procedure to transform back to the original domain. The ground data are reduced by downsampling such that the topographic information is reduced gradually with scale. In reducing the building data, the desired features (building width and areas) can be calculated directly from two corner points. This parameterization leads to a much milder loss of information about hydraulic boundary conditions as scale increases.

Our scale reduction method was evaluated using various measures: MSE, CC, FAN, and WDR. MSE and CC were used to evaluate the synthesized hydrologic DEM and to compare this to a naive downsampling image. The results show that our reduction method can preserve important information over a large range of scales. For example, the CC between the true and reduced “high risk area detection (DHRA)” is able to remain near 0.7 as the scale increases from 4 m to 32 m (see Figure 4-12). Over that same range of scales, the downsampling method shows a much more rapid deterioration of image quality (CC = 0.63 to 0.3) as the scale is increased. Since image quality is often determined subjectively, we used FAN and WDR to provide objective hydrologically meaningful metrics of performance. When looking at total discharge

rate in Figure 4-22, it was seen that our method approximates that true discharge much more faithfully as scale is increased than does downsampling.

Another important concept introduced in this work is the methodology to encode the impact of buildings for hydraulic modelers working at coarse scales over urban areas. We derived an equivalent friction factor based on the physical behavior of water flowing over complex structure elements (buildings), which can be used generally. The friction factor is a function of the size and width of a particular building along with water surface height. This work represents the first systematic framework for the efficient multiscale fusion of multiple-source DEMs and decomposition of urban DEMs for the preservation of hydraulic boundary information as a function of increasing scale.

As an exploratory method, we attempted to find an alternative measure of water discharge rate that could be used to choose an optimal scale for the building reduction. Since topographic

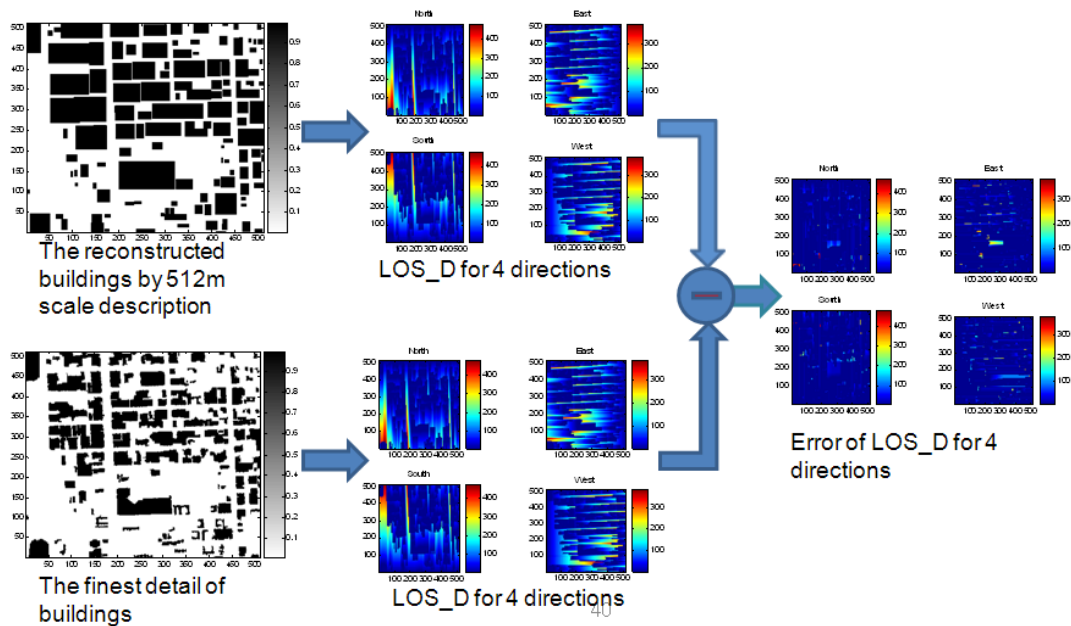


Figure 5-1. LOSD and its error for the quantization of buildings. LOSD for principal directions (North, East, South, and West) is computed.

relief in urban areas on coastal plains (e.g., Houston, TX; New Orleans, LA; Miami, FL; and Jacksonville, FL.) is quite small, buildings are the main features that impact the estimation of water discharge rate. We devised a line-of-sight distance (LOSD) metric, which measures the linear distance one can travel from a given pixel without being impeded by a building. We measured LOSD in the four principal directions (North, East, South, and West, Figure 5-1)

By determining that one or more of the MSE, CC and LOSD metrics tracks the error of discharge rate as scale is increased, we contend that they can be used as computationally efficient and alternative error measures to a highly complicated hydrodynamic model that keeps all higher order terms. From the results in Figure 5-2 and Table 5-1, we found that north and south direction LOSDs are most similar to $Q_{x(i)}$ generated in a case where the direction of water flow is set from west to east with no flow from north and south. In other words, the discharge rate is more affected by the channel widths than the channel length between buildings as long as the lots of channels are not completely blocked. The quantized buildings by our method preserve most of

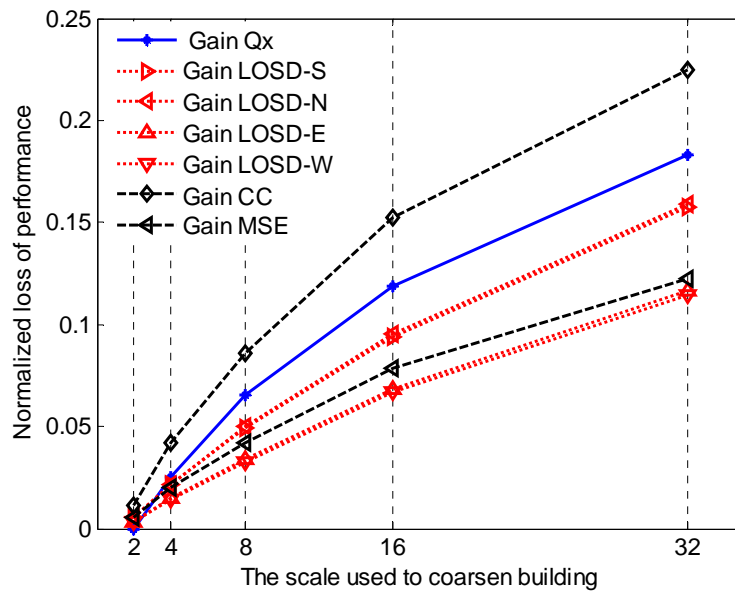


Figure 5-2. Comparison measurements (MSE, CC, LOSD) with Water discharge rate, (Q_x) for building reduction.

the channels between buildings. Therefore we can conclude that the loss of channel width between buildings in where the width is perpendicular to the direction of water flow, can be a major feature in deciding the performance of water discharge rate.

Table 5-1. The similarity between Gain Q_x and MSE, CC, LOSD

| | MSE | Difference of slope in loglog scale |
|---------------------------|---------|-------------------------------------|
| Gain Q_x vs Gain LOSD | 0.0005 | 0.0322 |
| Gain Q_x vs Gain LOSD-S | 0.00032 | 0.0261 |
| Gain Q_x vs Gain LOSD-N | 0.00029 | 0.0178 |
| Gain Q_x vs Gain LOSD-E | 0.0016 | 0.0691 |
| Gain Q_x vs Gain LOSD-W | 0.0017 | 0.0789 |
| Gain Q_x vs Gain CC | 0.00072 | 0.3006 |
| Gain Q_x vs Gain MSE | 0.0012 | 0.1556 |

APPENDIX
DETAILED DERIVATION OF PROCESS NOISE VARIANCE

Let the spatial interval be $0 \leq s \leq M$ and the spatial coarse-to-fine state model is

$$x(s) = \Phi(s)x(Bs) + \Gamma(s)w(s) \quad (\text{A-1})$$

where $w(s)$ is white process and uncorrelated $x(0)$

$$E[w(s)] = 0, \quad E[w(s)w^T(t)] = I\delta(s-t)$$

$$E[x(0)] = 0, \quad E[x(0)x^T(0)] = P_x(0)$$

The forward orthogonal condition is satisfied, i.e. $E[x(0)w^T(s)] = 0$ for $s \geq 0$

The backward model can be derived from (A.1) by reversing the direction of spatially dependent state variable.

$$x(Bs) = \Phi^{-1}(s)x(s) - \Phi^{-1}(s)\Gamma(s)w(s) \quad (\text{A-2})$$

The backward state process is still Markov but it does not satisfy the backward orthogonal condition between $x(M)$ and $w(s)$ for $s \leq M$.

We can define $w(s)$ by Markovity of minimum mean square error (MMSE) as follows

$$\begin{aligned} w(s) &= E[w(s) | x(s), x(s+1), \dots, x(M)] + \tilde{w}(s) \\ &= E[w(s) | x(s)] + \tilde{w}(s) \end{aligned} \quad (\text{A-3})$$

where $E[w(s) | x(s)]$ is MMSE estimate and due to the property of MMSE, $\tilde{w}(s) \perp x(s)$

We assume that $w(s)$ and $x(s)$ are zero-mean Gaussian so that the following equation applies: (Kay, 1993).

$$E[w(s) | x(s)] = E[w(s)x^T(s)]E[x(s)x^T(s)]^{-1}x(s) \quad (\text{A-4})$$

Since $x(s) = \Phi(s)x(Bs) + \Gamma(s)w(s)$ and we can substitute $x(s)$ into (A-3) so that

$$E[w(s) | x(s)] = \Gamma^T(s)P_x^{-1}(s)x(s) \quad (\text{A-5})$$

The backward Markov model can be rewritten (G.Verghese, 1979).

$$\begin{aligned}
x(Bs) &= \Phi^{-1}(s)x(s) - \Phi^{-1}(s)\Gamma(s)(E[w(s) | x(s)] + \tilde{w}(s)) \\
&= \Phi^{-1}(s)x(s) - \Phi^{-1}(s)\Gamma(s)\Gamma^T(s)P_x^{-1}(s)x(s) - \Phi^{-1}(s)\Gamma(s)\tilde{w}(s) \\
&= \Phi^{-1}(s)(I - \Gamma(s)\Gamma^T(s)P_x^{-1}(s))x(s) - \Phi^{-1}(s)\Gamma(s)\tilde{w}(s)
\end{aligned} \tag{A-6}$$

Let

$$F(s) = \Phi^{-1}(s)(I - \Gamma(s)\Gamma^T(s)P_x^{-1}(s)) \tag{A-7}$$

$$\bar{w}(s) = -\Phi^{-1}(s)\Gamma(s)\tilde{w}(s) \tag{A-8}$$

As a result, the backward Markov model is

$$x(Bs) = F(s)x(s) + \bar{w}(s) \tag{A-9}$$

Since

$$\begin{aligned}
P_x(s) &= \Phi(s)P_x(Bs)\Phi^T(s) + \Gamma(s)\Gamma^T(s) \\
\Phi^{-1}(s)P_x(s) &= \Phi^{-1}(s)\Phi(s)P_x(Bs)\Phi^T(s) + \Phi^{-1}(s)\Gamma(s)\Gamma^T(s) \\
\Phi^{-1}(s) &= \Phi^{-1}(s)\Phi(s)P_x(Bs)\Phi^T(s)P_x^{-1}(s) + \Phi^{-1}(s)\Gamma(s)\Gamma^T(s)P_x^{-1}(s) \\
\Phi^{-1}(s) - \Phi^{-1}(s)\Gamma(s)\Gamma^T(s)P_x^{-1}(s) &= P_x(Bs)\Phi^T(s)P_x^{-1}(s)
\end{aligned} \tag{A-10}$$

$F(s)$ is defined as

$$F(s) = P_x(Bs)\Phi^T(s)P_x^{-1}(s) \tag{A-11}$$

Let $Q(s) = E[\bar{w}(s)\bar{w}^T(s)]$ and

$$\begin{aligned}
E[\tilde{w}(s)\tilde{w}^T(s)] &= E[(w(s) - E[w(s) | x(s)])(w(s) - E[w(s) | x(s)])^T] \\
&= E[(w(s) - \Gamma^T(s)P_x^{-1}(s)x(s))(w(s) - \Gamma^T(s)P_x^{-1}(s)x(s))^T] \\
&= I - \Gamma^T(s)P_x^{-1}(s)E[x(s)x(s)^T]P_x^{-T}(s)\Gamma(s) \\
&= I - \Gamma^T(s)P_x^{-1}(s)P_x(s)P_x^{-T}(s)\Gamma(s) \\
&= I - \Gamma^T(s)P_x^{-1}(s)\Gamma(s)
\end{aligned} \tag{A-12}$$

It then follows that

$$\begin{aligned}
Q(s) &= E[\bar{w}(s)\bar{w}^T(s)] \\
&= \Phi^{-1}(s)\Gamma(s)E[\tilde{w}(s)\tilde{w}^T(s)]\Gamma^T(s)\Phi^{-T}(s) \\
&= \Phi^{-1}(s)\Gamma(s)\left[I - \Gamma^T(s)P_x^{-1}(s)\Gamma(s)\right]\Gamma^T(s)\Phi^{-T}(s) \\
&= \Phi^{-1}(s)\Gamma(s)\Gamma^T(s)\Phi^{-T}(s) - \Phi^{-1}(s)\Gamma(s)\Gamma^T(s)P_x^{-1}(s)\Gamma(s)\Gamma^T(s)\Phi^{-T}(s)
\end{aligned} \tag{A-13}$$

Since

$$\begin{aligned}
P_x(s) &= \Phi(s)P_x(Bs)\Phi^T(s) + \Gamma(s)\Gamma^T(s) \\
\Phi^{-1}(s)P_x(t) &= \Phi^{-1}(t)\Phi(s)P_x(Bs)\Phi^T(s) + \Phi^{-1}(s)\Gamma(s)\Gamma^T(s) \\
\Phi^{-1}(s) &= \Phi^{-1}(s)\Phi(s)P_x(Bs)\Phi^T(s)P_x^{-1}(s) + \Phi^{-1}(s)\Gamma(s)\Gamma^T(s)P_x^{-1}(s) \\
\Phi^{-1}(s)\Gamma(s)\Gamma^T(s)\Phi^{-T}(s) &= \Phi^{-1}(s)\Phi(s)P_x(Bs)\Phi^T(s)P_x^{-1}(s)\Gamma(s)\Gamma^T(s)\Phi^{-T}(s) \\
&\quad + \Phi^{-1}(s)\Gamma(s)\Gamma^T(s)P_x^{-1}(s)\Gamma(s)\Gamma^T(s)\Phi^{-T}(s) \\
\Phi^{-1}(s)\Gamma(s)\Gamma^T(s)P_x^{-1}(s)\Gamma(s)\Gamma^T(s)\Phi^{-T}(s) &= \Phi^{-1}(s)\Gamma(s)\Gamma^T(s)\Phi^{-T}(s) + P_x(Bs)\Phi^T(s)P_x^{-1}(s)\Gamma(s)\Gamma^T(s)\Phi^{-T}(s)
\end{aligned} \tag{A-14}$$

$Q(s)$ can be rewritten

$$Q(s) = P_x(Bs)\Phi^T(s)P_x^{-1}(s)\Gamma(s)\Gamma^T(s)\Phi^{-T}(s) \tag{A-15}$$

Since $F(s) = P_x(Bs)\Phi^T(s)P_x^{-1}(s)$ and

$$\begin{aligned}
P_x(s) &= \Phi(s)P_x(Bs)\Phi^T(s) + \Gamma(s)\Gamma^T(s) \\
P_x(s)\Phi^{-T}(s) &= \Phi(s)P_x(Bs)\Phi^T(s)\Phi^{-T}(s) + \Gamma(s)\Gamma^T(s)\Phi^{-T}(s) \\
\Gamma(s)\Gamma^T(s)\Phi^{-T}(s) &= P_x(t)\Phi^{-T}(s) - \Phi(s)P_x(Bs)
\end{aligned} \tag{A-16}$$

It then follows that

$$\begin{aligned}
Q(s) &= F(s)\left(P_x(s)\Phi^{-T}(s) - \Phi(s)P_x(Bs)\right) \\
&= F(s)P_x(s)\Phi^{-T}(s) - F(s)\Phi(s)P_x(Bs)
\end{aligned} \tag{A-17}$$

Since $F(s) = P_x(Bs)\Phi^T(s)P_x^{-1}(s) \rightarrow F(s)P_x(s)\Phi^{-T}(s) = P_x(Bs)$ the expression for

$Q(s)$ becomes

$$\begin{aligned}
Q(s) &= P_x(Bs) - F(s)\Phi(s)P_x(Bs) \\
&= (I - F(s)\Phi(s))P_x(Bs)
\end{aligned} \tag{A-18}$$

The equation of $Q(s)$ which was written in (Fieguth *et al.*, 1995) can be derived from

$$\begin{aligned}
Q(s) &= P_x(Bs)\Phi^T(s)P_x^{-1}(s)\Gamma(s)\Gamma^T(s)\Phi^{-T}(s) \\
&= P_x(Bs)\Phi^T(s)P_x^{-1}(s)\left[P_x(s)\Phi^{-T}(s) - \Phi(s)P_x(Bs)\right] \\
&= \left[P_x(Bs)\Phi^T(s)P_x^{-1}(s)P_x(s)\Phi^{-T}(s) - P_x(Bs)\Phi^T(s)P_x^{-1}(s)\Phi(s)P_x(Bs)\right] \\
&= \left[P_x(Bs) - P_x(Bs)\Phi^T(s)P_x^{-1}(s)\Phi(s)P_x(Bs)\right] \\
&= P_x(Bs)\left[I - \Phi^T(s)P_x^{-1}(s)\Phi(s)P_x(Bs)\right]
\end{aligned} \tag{A-19}$$

As a result, we can get two equations for $Q(s)$

$$\begin{aligned}
Q(s) &= P_x(Bs)\left[I - \Phi^T(s)P_x^{-1}(s)\Phi(s)P_x(Bs)\right] \\
&= (I - F(s)\Phi(s))P_x(Bs)
\end{aligned} \tag{A-20}$$

Since the calculation of $F(s)$ is necessary in the middle of changing the posterior estimate at previous scale into the prior estimate at present scale, we achieved a two multiplication reduction in scalar type MKS. This new equation is general form so that we can achieve more operations for vector type MKS.

LIST OF REFERENCES

- Acheson, D. J., 1990, *Elementary Fluid Dynamics*, Oxford Applied Mathematics and Computing Science Series, (Oxford University Press).
- Alemseged, T. H. and Rientjesb, T.H.M., 2005, Effects of LiDAR DEM Resolution in Flood Modelling : A model sensitivity study for the city of Tegucigalpa, Honduras, Proceedings of the ISPRS Workshop Laser Scanning, Netherlands, pp. 12-14
- Anderson, B. D. O., 1999, From Wiener to Hidden Markov models In *IEEE IDC99*, page 239, Adelaide, South Australia.
- ArcGIS, 2008, Desktop Help, Available online at: <http://webhelp.esri.com/arcgisdesktop/9.2>, Copyright © Environmental Systems Research Institute, Inc
- Bates, P., 2004, Remote sensing and flood inundation modeling, *Hydrological Processes*. **18**, pp.2593-2597
- Bates,P.D., and Roo, A.P.J., 2000, A simple raster-based model for flood inundation simulation, Elsevier *Journal of Hydrology*, **236**, pp. 54–77
- Bovik, A. 2005, *Handbook of image and video processing*, 2nd edition, (Elsevier)
- Brown, R.G. and Hwang, P., 1996, *Introduction to Random Signals and Applied Kalman Filtering*. 3rd ed. (John Wiley and Sons)
- Bruneau P., Gascuel-Oudoux C., Robin P., Merot, P. and Beven, K., 1995, The sensitivity to space and time resolution of a hydrological model using digital elevation data, *Hydrological Processes*, **9**, pp. 69–81
- Carter, W., Shrestha, R., Tuell G., Bloomquist D., and Sartori, M., 2001, Airborne laser swath mapping shines new light on earth's topography. *Eos, Transactions, American Geophysical Union*, **82**, pp. 549, 550, 555.
- Cheung, S., Jhee, H., and Slatton, K.C., unpublished, Fusing airborne and SRTM data for improved multiscale DEMs over coastal zone and landscape-dependent evaluation of SRTM accuracy. *Photogrammetric Engineering and Remote Sensing*, (conditional accepted)
- Chou, K., Willsky A., and Albert, B., 1994, Multiscale recursive estimation data fusion and regularization, *IEEE Transaction on Automatic Control*, **39**, pp. 464 – 478.
- Chow, V., Maidment, D., and Mays, L.W., 1988, *Applied Hydrology*. (McGraw-Hill)
- Covelli, P., Marsili-Libelli, S., and Pacini, G., 2002, SWAMP: A two-dimensional hydrodynamic and quality modeling platform for shallow waters, *Numerical Methods for Partial Differential Equations: Wiley Periodicals*, **18**, pp. 663-687.

- Cover, T.M. and Thomas, J.A., 1991, *Elements of Information Theory*. (John Wiley & Sons)
- Curkendall, D., Fielding, E., Cheng, T., and Pohl, J., 2003, A computational-grid based system for continental drainage network extraction using SRTM digital elevation models. In *Proceedings of the International Conference on Parallel Processing Workshops, ICPPW03*, 6-9 October, pp. 181-190.
- Daniel, M. and Willisky, A., 1997, A multiresolution methodology for signal-level fusion and data assimilation with applications to remote sensing. In *Proceedings of the IEEE*, **5**, January, pp. 164-180
- Dean, R., and Dalrymple, R., 2002, *Coastal Processes with Engineering Applications*. (Cambridge University Press)
- Desmet, P.J.J. and Govers, G., 1996, Comparison of routing algorithms for digital elevation models and their implications for predicting ephemeral gullies, *International Geographical Information Systems*, **10**, pp. 311-331
- Dobson, M., Ulaby, F., Pierce, L., Sharik, T., Bergen, K., Kellndorfer, J., Kendra, J., Li, E., Lin, Y., Nashashibi, A., Sarabandi, K., and Siqueira, P., 1995, Estimation of forest biophysical characteristics in northern michigan with SIR-C/X-SAR. *IEEE Transactions on Geoscience and Remote Sensing*, **33**, July, pp. 877 – 895.
- Fairfield, J., and Leymarie, P., 1991, Drainage networks from grid digital elevation models. *Water Resource Research*, **27**, pp.709-717
- Farr, T. G., Rosen, P.A., Caro, E., Crippen, R., Duren, R., Hensley, S., Kobrick, M., Paller, M., Rodriguez, E., Roth, L., Seal, D., Shaffer, S., Shimada, J., and Umland, J., 2007, The Shuttle Radar Topography Mission, *Rev. Geophys.*, **45**,
- Fieguth, P., Karl, W., Willisky, A., and Wunsch, C., 1995, Multiresolution optimal interpolation and statistical analysis of TOPEX/POSEIDON satellite altimetry. *IEEE Transactions on Geoscience and Remote Sensing*, **33**, March, pp. 280–292.
- Gan, Q., and Harris, C.J., 2001, Comparison of two measurement fusion methods for Kalman-filter-based multisensor data fusion, *IEEE Transactions on Aerospace and Electronic System*, **37**, issue 1, pp. 273-279
- Gader, P., Lee, W., and Wilson, J., 2004, Detecting landmines with ground-penetrating radar using feature-based rules, order statistics, and adaptive whitening. *IEEE Transactions on Geoscience and Remote Sensing*, **42**, November, pp. 2522-2534.
- Gao, Y., Maggs, M., 2005, Feature-level fusion in personal identification, *Proceedings of the 2005 IEEE Computer Society Conference on Computer Vision and Pattern Recognition*, **1**, pp. 468-473

- Gesch, D., William, J., and Miller, W., 2001, A comparison of U.S. geological survey seamless elevation models with shuttle radar topography mission data. In *Geoscience and Remote Sensing Symposium, (IGARSS '01). IEEE 2001 International*, **2**, 9-13 July, pp. 754-756
- Gonzalez, R., and Wood, R., 2002, *Digital Image Processing*, 2nd ed (Prentice Hall)
- Gunatilaka, A.H., and Baertlein, B.A., 2001, Feature-level and decision-level fusion of noncoincidentally sampled sensors for land mine detection, *IEEE Transactions on Pattern Analysis and Machine Intelligence*, **23**, issue: 6, pp. 577-589
- Haykin, S., 2002, *Adaptive Filter Theory*, Fourth Ed. (Prentice Hall)
- Hall, D., and Llinas, J., 1997, An introduction to multisensor data fusion, In *Proceedings of the IEEE*, **85**, January, pp. 6-23
- Harris, D., 1963, Characteristics of the hurricane storm surge, Technical Paper No. 48, Weather Bureau, U.S. Dept of Commerce, Washington, D.C., pp. 139.
- Hensley, S., 2005, From raw data to digital elevation map. In *Workshop of the Shuttle Radar Topography Mission – Data Validation and Applications*, 14-16 June, Virginia.
- Hicks, S., Sillcox, R., Nichols, C., Via, B., and McCay E., 2000, *Tide and Current Glossary*. U.S. Department of Commerce, National Oceanic and Atmospheric Administration, January
- Horritt, M.S., and Bates, P.D., 2001, Effects of spatial resolution on a raster based model of flood flow, *Journal of Hydrology*, **253**, pp.239-249.
- Hunter, N. M., Bates, P. D., Horritt, M. S., Wilson, M. D., 2007, Simple spatially-distributed models for predicting flood inundation: A review, Elsevier *Geomorphology* , pp. 208–225
- IHRC, 2004, WSMP (Windstorm Simulation & Modeling Project): Airborne LiDAR data and digital elevation models in Miami-Dade, Florida, final report. International Hurricane Research Center (IHRC).
- Iwasa, Y., Inoue, K., and Mizutori, M., 1980, Hydrologic analysis of overland flood flows by means of numerical method. *Annual Report*, Disaster Prevention Research Institute in Kyoto University
- Jain, I., Chittibabu, P., Agnihotri, N., Dube, S.K., Sinha, P.C., and Rao, A.D., 2006, Numerical storm surge model for India and Pakistan, *Natural Hazard*, Springer, 42, No. 1, pp. 67-73
- Kamen, E.W. and Su, J. K. Su, 1999, *Introduction to Optimal Estimation*. London, UK:(Springer-Verlag)
- Kay, S.M., 1993, *Fundamentals of Statistical Signal Processing: Estimation Theory*. (Upper Saddle River, NJ: Prentice Hall)

- Komar, P. D., 1998, *Beach Processes and Sedimentation*, 2nd ed. (Upper Saddle River, NJ: Prentice Hall)
- Kuperman, W., and Lynch, J., 2004, Shallow-water acoustics. *Physics Today*, **55**, October, pp. 55-57.
- LADS, 2003, Dade County LADS Survey Report. Coastal Planning and Engineering in Florida Department of Environmental Protection, Tallahassee, FL.
- Luetlich, R., and Westerink, J., 2006, A (Parallel) Advanced Circulation Model for Oceanic, Coastal and Estuarine Waters”, Technical Report, Available online at :<http://www.adcirc.org/>.
- McMillan, H., and Brasington, J., 2007, Reduced complexity strategies for modeling urban floodplain inundation, Elsevier *Geomorphology*, pp.226-243
- NEELZ, S and Pender, G., 2007, Sub-grid scale parameterisation of 2D hydrodynamic models of inundation in the urban area, *Acta Geophysica*, **55**, no. 1, pp. 65-72
- NGA, 2005, Geosciences: Coordinate Systems Analysis. National Geospatial-imagery Agency, Bethesda, MD.
- NGDC, 2005, Available online at: www.ngdc.noaa.gov, National Geophysical Data Center (NGDC), National Oceanic & Atmospheric Administration, Washington, DC.
- NOAA CSC, “Part II of a roadmap to a seamless topobathy surface”. Technical Report, National Oceanic and Atmospheric Administration Coastal Service Center, Washington, DC. 2007
- O’Callaghan, J.F. and Mark, D.M., 1984, The extraction of drainage networks from digital elevation data. , *Computer Vision Graphics and Image Proceedings*, **28**, pp. 323-344
- Resio, D. T., and Westerink, J. J., 2008, Modeling the physics of storm Surges, Feature Article. *Physics Today*.
- Robertson, W., Whitman, D., Zhang, K., and Leatherman, S.P., 2004, Mapping shoreline position using airborne laser. *Journal of Coastal Research*, **20**, pp.884-892.
- Roweis, S. and Ghahramani, Z., 1999, A unifying review of linear gaussian models. *Neural Computation* , **11**, pp. 305-345.
- Schubert, J. E., Sanders, B. F., Smith, M. J., Wright, N. G., 2008, Unstructured mesh generation and landcover-based resistance for hydrodynamic modeling of urban flooding, Elsevier, *Advances in Water Resources*. **31**, Issue 12, December, pp.1603-1621
- SFWMD, 1999, 1999 Land Cover Land Use Section 3, (Miami-Dade Co), Available online at: www.sfwmd.gov/org/gisit/index.html, South Florida Water Management District (SFWMD), West Palm Beach, FL.

- Shepard, M.S., Yerry, M.A., 1983, Approaching the automatic generation of finite elements meshes, *Computers in Mechanical Engineering*, **1**, pp. 49-56
- Shrestha, R.L., Carter W.E., Sartori, M., Luzum, B.J. and Slatton, K.C., 2005, Airborne laser Swath Mapping: quantify changes in sandy beaches over time scales of weeks to years. *ISPRS Journal of Photogrammetry and Remote Sensing*, **59**, pp. 222-232
- Slater, J., 2005, personal communication. National Geospatial Agency (NGA).
- Slatton, K.C., Cheung S., and Jhee, H., 2005, Reduced-complexity fusion of multiscale topography and bathymetry data over the Florida coast. *IEEE Geoscience and Remote Sensing Letters*, **2**, pp. 389-393.
- Slatton, K.C., Crawford, M.M., and Evans, B.L., 2001, Fusing interferometric radar and laser altimeter data to estimate surface topography and vegetation heights. *IEEE Transactions on Geoscience and Remote Sensing*, **39**, pp. 2470-2482.
- Sorenson, H.W., 1970, Least-square estimation: From Gauss to Kalman, *IEEE Spectrum*, pp. 63-68
- Starek, M., Slatton, K.C., and Adams, P., 2005, High-resolution measurement of beach morphological response to hurricane-induced wave dynamics, *Eos, Transactions, American Geophysical Union, Fall Meet. Suppl.*, Abstract G34A-06.
- Stumpf, R. P., Holderied K., and Sinclair, M., 2003, Determination of water depth with high-resolution satellite imagery over variable bottom types. *Limnology and Oceanography*, **48**, pp. 547-556.
- Treuhaft, R. N. and Siqueira, P., 2000, Vertical structure of vegetated land surfaces from interferometric and polarimetric radar, *Radio Science*, **35**, pp. 141-177.
- Turcotte, D. L., 1997, *Fractals and Chaos in Geology and Geophysics*, 2nd ed, (Cambridge University Press).
- USACE, 2004, CORPSCON Coordinate Conversion Software, Available online at: crunch.tec.army.mil/software/corpscon/corpscon.html, US Army Corps Engineers, Alexandria, VA
- USGS, 2000, Fact Sheet 040-00, US GeoData Digital Elevation Models, Available online at: erg.usgs.gov/isb/pubs/factsheets/fs04000.html, U.S. Geological Survey, Reston, VA.
- USGS, 2004, Seamless Data Distribution system, Available online at: seamless.usgs.gov/, U.S. Geological Survey, Reston, VA.
- Verghese, G. and Kailath, T., 1979, A further note on backward markovian models. *IEEE Transactions on Information Theory*, **IT-25**, pp. 121-124

- Vemulakonda, S.R., Scheffner, N.W., Mark, D.J., and Brown, M.E., 1999, Water-surface elevation frequency estimates for the Louisiana Coast, Coastal Engineering Research Center, **CERC-99-1**,
- Wang, M., and Hjelmfelt, A., 1998, DEM based overland flow routing model. *Journal of Hydrologic Engineering*, **3**, January, pp. 1-8.
- Wegmuller, U. and Werner, C., 1997, Retrieval of vegetation parameters with SAR interferometry, *IEEE Transactions on Geoscience and Remote Sensing*, **35**, pp. 18-24.
- Wilson, M. D., 2004, Evaluating the effect of data and data uncertainty on predictions of flood inundation, PhD dissertation.
- Willsky, A.S., 2002, Multiresolution markov models for signal and image processing, *Proceedings of the IEEE*, **90**, No. 8, pp. 1396-1458, August
- Wolfgang S., 2008, personal communication, Institute of Geographic Sciences, Freie Universit at Berlin, Germany
- Woods, J., 1984, Two-Dimensional Digital Signal Processing I:Chapter 5, (Springer)
- Zhang, K., Chen, S.C., Whitman, D., Shyu, M., Yan, J. and Zhang, C., 2003, A progressive morphological filter for removing non-ground measurements from airborne LiDAR data, *IEEE Transactions on Geoscience and Remote Sensing*, **41**, pp. 872-882.
- Zhang, X., Long, W., Xie, H., Zhu J. and Wang J., 2007, Numerical simulation of flood inundation processes by 2D shallow water equation. Research Article, *Frontiers and Architecture and Civil Engineering in China*, **1**, pp. 107-113

BIOGRAPHICAL SKETCH

Sweungwon Cheung was born in Seoul, South Korea. He received both his B.S. degree and M.S. degree in Information Engineering from Korea University, South Korea in 1994 and 1996, respectively.

After obtaining a second M.S degree in Electric and Computer Engineering from the University of Colorado in 2000, he began to pursue a Ph. D degree in Electrical and Computer Engineering at the University of Florida. Since 2003 he has worked under the supervision of Dr. Kenneth C. Slatton. His research interests include remote sensing, image fusion and reduction, and stochastic estimation.